

A Refined Methodology for Calibrating Premium Threaded Connection Make-ups

Erik B. Ostergaard

Thesis submitted to the faculty of the Virginia Polytechnic Institute and State University  
in partial fulfillment of the requirements for the degree of

Master of Science  
In  
Mechanical Engineering

Robert L. West, Chair  
David H. Coe  
Romesh C. Batra

February 22, 2013  
Blacksburg, Virginia

Keywords: (Oil Country Tubular Goods, Connection Make-up, Finite Element Analysis,  
Digital Image Correlation)

Copyright 2013, Erik B. Ostergaard

# A Refined Methodology for Calibrating Premium Threaded Connection Make-ups

Erik B. Ostergaard

## ABSTRACT

Digital Image Correlation is used to generate high-spatial-density full-field displacement and strain data of a connection box outer diameter for use in the calibration of finite element make-up models. Image acquisition and data processing techniques are discussed and best practice recommendations are made. 3D-wedge models consisting of a twenty-degree sweep of the connection geometry are generated from manufacturer supplied profiles. Deformation plasticity material models are developed from identified minimum strength material coupons. Axisymmetric and 3D meshing schemes are used to capture the geometric complexity, supply enough resolution to represent seal performance, and provide a solution in an acceptable timeframe. Several techniques for achieving good contact resolution are presented. The mechanics of the full 3D connection makeup are decomposed into simple idealized representations. Finite element boundary conditions are developed to adequately represent the 360-degree make-up mechanics in a wedge section. The wedge model is loaded to achieve a torque-rotation coupling which satisfies the experimental make-up conditions. This model displays a much improved ability to capture box outer diameter strain and displacement fields, and thus better represents the mechanics of a connection make-up. A 3D inspired axisymmetric pretension loading scheme is developed which enables the 3D-wedge seal conditions to be replicated in a computationally efficient axisymmetric form for connection performance evaluation. Seal metrics are developed and converged to evaluate connection sealing capabilities in the power-tight configuration. Modeling error metrics are developed, and the final 3D-wedge model is evaluated relative to the experimental DIC data.

# Acknowledgements

I would like to thank my advisor, Dr. Robert L. West for his guidance of this research and his passion for education. I'm very grateful to Dr. David H. Coe for his expertise and for bringing this work to Virginia Tech. Thanks also to Prof Romesh C. Batra for his support throughout this effort.

Many thanks to Nick Angelini for his help with the formulation and implementation of the correlation code and to Jeremy Mateyk for his contribution to the meshing schemes and modeling efforts. I would also like to thank the Hess Corporation for their financial sponsorship.

Thanks to my wife Lindsey and my parents Dale and Lea Ann for your support and encouragement. Many thanks to the Graduate Christian Fellowship at Virginia Tech and to the congregation of Cambria Baptist Church. Thank you Jesus for the strength to complete this work and for life itself.

ERIK B. OSTERGAARD

*Virginia Polytechnic Institute and State University  
February 2013*

# Table of Contents

Acknowledgements.....	iii
Table of Contents.....	iv
List of Figures.....	vii
List of Tables.....	x
Nomenclature.....	xi
Chapter 1 Introduction and Motivation.....	1
1.1 Research Objective.....	1
1.2 Solution Hypothesis.....	1
1.3 Problem Statement.....	2
1.4 Scope of Study.....	2
1.5 Discussion and Organization.....	3
Chapter 2 Literature Review.....	4
2.1 Connection Make-up Modeling.....	4
2.2 Evaluation of Performance Limits.....	5
2.3 Sealing Criteria.....	5
2.4 Strain gauging OCTG's and Digital Image Correlation.....	5
Chapter 3 Digital Image Correlation.....	7
3.1 Motivation and Description.....	7
3.2 DIC Calibration.....	7
3.2.1 Fiduciary Marks.....	8
3.3 Data Acquisition.....	8
3.4 Error and Precision in the DIC.....	10
3.5 Data Processing, Reduction, and Alignment.....	12
3.5.1 DIC Coordinate System Definition.....	12
3.5.2 Removing Rigid Body Motion.....	13
3.5.3 Data Extraction.....	14
3.5.4 DIC Filtering.....	14
Chapter 4 The Finite Element Make-up Model.....	16
4.1 Overview of a Premium Connection Make-up.....	16
4.2 Reducing Run Time.....	17
4.2.1 The Full 3D Model.....	17
4.2.2 The Axisymmetric Form.....	17

4.2.3	The 3D-Wedge Assumption .....	20
4.3	Geometry .....	20
4.3.1	Axisymmetric Geometries .....	20
4.3.2	3D Geometry from Axisymmetric Geometries.....	20
4.4	Material Models .....	22
4.4.1	Optimizing the Ramberg-Osgood Deformation Plasticity Model .....	22
4.5	Meshing Schemes.....	24
4.5.1	Axisymmetric Meshing.....	24
4.5.2	3D Meshing.....	26
4.6	Resolving the Contact Problem.....	29
4.6.1	Standard Interference Fit.....	30
4.6.2	Method of Thermal Expansion .....	32
4.6.3	Explicit Finite Element Contact Formulation .....	34
4.7	Loading Schemes and Boundary Conditions .....	36
4.7.1	3D Loading Methods .....	36
4.7.2	3D Inspired Axisymmetric Pretension Loading .....	47
4.8	Seal Metrics.....	49
4.8.1	Contact Pressure and the Pressure Penetration Routine .....	49
4.8.2	Contact Normal Strain .....	50
4.8.3	Contact Length and Contact Area.....	50
4.8.4	Strain Energy Density and the Seal Number .....	50
4.8.5	Convergence of Seal Metrics .....	53
4.8.6	Seal Metric Results and Discussion.....	54
Chapter 5	Calibration of the Finite Element Model .....	58
5.1	Model Error Metrics.....	58
5.1.1	The Correlation Coefficient .....	58
5.1.2	Data Set Alignment.....	58
5.1.3	Sum Squared Error.....	59
5.1.4	Fast Fourier Transform .....	60
5.1.5	Analysis of the Residuals.....	61
5.2	Identifying the Minimum Error Make-up Model.....	63
Chapter 6	Summary, Conclusions, and Recommendations.....	65
6.1	Summary and Conclusions.....	65
6.2	Recommendations .....	67

6.2.1	The In-Plane Minimum Seal Performance Envelope .....	67
6.2.2	The Out-of-Plane Minimum Seal Performance Envelope .....	67
6.2.3	Response Surface Modeling .....	68
	Bibliography .....	71
	Appendix A Data Flow Diagram for Minimum Seal Performance Envelope Generation .....	74
	Appendix B Photographs of Experimental Setup.....	79
	Appendix C Mapping for Material Coupons.....	80
	Appendix D MATLAB Code for Deformation Plasticity Material Model Optimization .....	81
	Appendix E Finite-Element Based Response Surface Formulation .....	82
	E.1 Response Surface Example in a Single Dimension .....	82
	E.2 Extending the Response Surface to Problems of Higher Dimension.....	87
	Appendix F Copyright Permission Letters .....	88

# List of Figures

Figure 1.1: High level data flow diagram for the generation of a premium connection minimum seal performance envelope. ....	2
Figure 3.1: Axial strain vs. axial length of a commonly used OCTG premium connection after make-up. Used with permission of Hess Corporation [18]. ....	7
Figure 3.2: Diagram illustrating the ARAMIS experimental setup. Used with permission of Hess Corporation [18]. ....	9
Figure 3.3: Demonstration of pattern tracking during deformation. Undeformed left and right camera images (top) and deformed left and right camera images (bottom). Used with permission of Trilion Quality Systems [19]. ....	9
Figure 3.4: The random paint pattern applied to the box with axial strain output overlaid (left). A GOM ARAMIS DIC camera system (right). Used with permission of Trilion Quality Systems [19]. ....	10
Figure 3.5: Two issues with the DIC data are highlighted. Inadequate lighting and/or a poor paint pattern in some areas produces a void in the computed data fields. The small offset between the image computation grid (blue) and the assumed system coordinates (black) produces a coordinate mismatch which prevents equal spacing between extracted section points (gold). ....	11
Figure 3.6: The fitted cylinder used to orient the DIC data. The coordinate system was defined by points projected from the image surface to the axis of the cylinder primitive. ....	12
Figure 3.7: The region of least deformation used to identify the rigid body mode is shown in dark grey to the far right of the image. The extraction set locations are shown plotted over the result, and are designated by circumferential coordinate. ....	13
Figure 3.8: The extracted results from Figure 3.7. The displacement results are forced to zero at the far right of the extraction sets. The extracted axial displacement data is shown plotted as a function of the axial coordinate. ....	14
Figure 3.9: The relationship between the time and frequency domains. a) Three-dimensional coordinates showing time, frequency, and amplitude b) Time domain view c) Frequency domain view. © Agilent Technologies, Inc. 2000. Reproduced with Permission, Courtesy of Agilent Technologies, Inc. [20]. ....	15
Figure 3.10: FFT Filtering demonstrated on a sample DIC extracted set. To the left, the original extracted signal in blue, and the reconstructed inverse FFT signal using only low frequency content in red. To the right, the spatial frequency content of the filtered signal after the high frequencies have been thrown out. ....	15
Figure 4.1: A generic axisymmetric connection geometry shown in the shoulder-tight configuration. ....	16
Figure 4.2: An axisymmetric pretension section using four dilated pretension sections. The deformations have been exaggerated for visualization purposes. ....	18
Figure 4.3: The axial displacement field of an axisymmetric pretension model. ....	18
Figure 4.4: The extracted axial displacement field. ....	19
Figure 4.5: The resulting axial displacement field overlaid on the DIC displacement data. ....	19
Figure 4.6: Simplified axisymmetric profile illustrating the cut-planes and transition regions used to generate the 3D swept sections. The Nose, Shoulder, and	

Base sections are revolved without a helix angle. The threaded regions include a helix angle in the revolution.....	21
Figure 4.7: The five 3D swept regions with transition regions before (left) and after (right) the merge operation. All interior surfaces are discarded and the single solid part remains.....	22
Figure 4.8: A fitted Ramberg-Osgood deformation plasticity material model.....	23
Figure 4.9: Partitioning scheme used for assignment of mesh parameters. High mesh density regions shown in red, medium density thread regions in orange, medium-sparse density shown in yellow, sparse density in green, and transition regions in pink. ....	24
Figure 4.10: Thread partitioning (left) and meshing scheme (right). ....	25
Figure 4.11: The circumferential double biasing scheme provides low aspect ratio at the wedge centerline and the edges. The aspect ratio of the elements on the wedge centerline at the seals is fixed at 1. Seal results are extracted from the area shown in red.....	27
Figure 4.12: Meshing techniques used to achieve efficient mesh transitions.....	28
Figure 4.13: Sample torque-turn plot from experimental connection make-up illustrating the shoulder point and final torque dump. Used with permission of Hess Corporation [18].....	30
Figure 4.14: Master box contact surface shown in red. Slave pin contact surface shown in pink. ....	31
Figure 4.15: The smooth step amplitude curve used to apply the maximum allowable interference constraint in the contact formulation. First and second time derivatives also shown. ....	32
Figure 4.16: The coordinate system defined for the orthotropic expansion coefficients with desired thread translation vector $V$ and angle $\beta$ corresponding to a positive temperature change. The box is displayed in green, and the pin in grey. ....	33
Figure 4.17: The composite cylinder example problem. ....	38
Figure 4.18: An overlay of three solutions for the composite cylinders problem. ....	40
Figure 4.19: The 20-degree wedge model illustrating the displacement controlled loading method.....	42
Figure 4.20: An overlay of three solutions for the Torsion bar problem.....	43
Figure 4.21: Depiction of composite cylinder wedge model behavior with antisymmetric boundary conditions on the cut-planes. The box is shown in red, the pin in blue, and the pipe axis is out of the page. ....	44
Figure 4.22: Boundary conditions and loading scheme for 3D-wedge model. ....	45
Figure 4.23: Naming conventions shown for Pin and Box surfaces. Displacement results were extracted on both the Box ID and the Pin OD for the 3D-axisymmetric seal calibration. ....	47
Figure 4.24: Displacement field of the Box ID for the both the 3D and axisymmetric models. The pretension sections are shown as well as the shoulder, inner seal, and outer seal locations.....	48
Figure 4.25: Displacement field of the Pin OD for the both the 3D and axisymmetric models. The pretension sections are shown as well as the shoulder, inner seal, and outer seal locations.....	48

Figure 4.26: Axisymmetric pretension loading scheme shown. Pretensions which dilate shown in red. Pretensions which contract shown in blue. Fixed axial boundary conditions shown in orange. ....	49
Figure 4.27: Components used in the calculation of the Seal Number; the element height $h$ , change in element height due to load $\delta$ , the component of the stress tensor normal to the seal surface projected to the node $\sigma_{ni}$ , the seal surface unit normal vectors $n_i$ , the element seal face lengths $L_i$ , and the seal coordinate $l_s$ . The normal strain can be visualized as $\epsilon_n = \delta/h$ .....	53
Figure 4.28: Convergence plots for each seal metric.....	54
Figure 4.29: Diagram of connection naming conventions illustrating the “High Low – Pin Slow Box Fast” configuration.....	55
Figure 5.1: Alignment of data sets. $\phi_{optim}$ is the phase offset that produces the largest correlation coefficient. The trimmed data sets (illustrated in red) are passed forward for error metric evaluation.....	59
Figure 5.2: FFT overlays of the FE and DIC data. Note: The vertical scales are not constant in this image.....	61
Figure 5.3: Example plots of the residual analysis. ....	62
Figure 5.4: FFT of the residuals for the final correlated model. The FFT SSE from Equation (5.3) is a squared summation of the above data. ....	63
Figure 5.5: Final overlay of 3D-wedge finite element data and extracted DIC data. Displacements (top) and Strains (bottom) show strong resemblance. ....	64
Figure 6.1: The In-Plane Minimum Seal Performance Envelope can be discretized into several segments which allow the envelope to be operated upon.....	67
Figure 6.2: Trajectory functions can be used to generate Out-of-Plane Minimum Seal Performance envelopes and to interpolate minimum seal performance limits between known test configurations. Here the trajectories operate as a function of the outer diameter design variable.....	68
Figure 6.3: The response surface can operate upon a parametric finite element make-up model to identify the modeling configuration that produces the minimum error with respect to the experimental data.....	69
Figure 6.4: The response surface can operate upon a parametric finite element service load model to investigate seal performance across the load space. ....	70
Figure B.1: A good DIC experimental setup. Cameras pushed far apart to maximize the dynamic range of the out-of-plane ray tracing measurement. Cameras are also oriented parallel to the pipe axis to give better resolution for in-plane measurements. Used with permission of Hess Corporation [18].....	79
Figure B.2: A poor DIC experimental setup. Cameras are not separated by a sufficient angle. Cameras also oriented perpendicular to the pipe axis. Used with permission of Hess Corporation [18].....	79
Figure E.3: The 1D linear response surface element with normalized local coordinate $\xi$ .....	83
Figure E.4: The 1D response surface mesh in the global coordinate system consisting of two linear 1D elements. ....	83
Figure E.5: The linear response surface solution to $F(x) = x^2$ using two elements. ....	85
Figure E.6: The 1D quadratic response surface element. ....	86
Figure E.7: The single quadratic element response surface solution to $F(x) = x^2$ . ....	86

## List of Tables

Table 3.1: Statistics for DIC data.....	11
Table 4.1: Seeding guidelines and element distributions for axisymmetric meshes at different levels of refinement.....	26
Table 4.2: Seeding guidelines and element distributions for 3D meshes at different levels of refinement.....	29
Table 4.3: Features for the composite cylinders finite element models .....	40
Table 4.4: Features for the torsion bar finite element models .....	41
Table 4.5: Tangential boundary conditions at the top surface for the torsion bar wedge problem. ....	42
Table 4.6: Maximum torque achieved by model as a function of friction coefficient.....	46
Table 4.7: Typical seal metric convergence levels. ....	54
Table 4.8: Contact Pressure results from the comparative seal analysis. Results extracted from equivalent axisymmetric model configurations developed from 3-D wedge models and correlated with DIC data. ....	55
Table 4.9: Normal Strain results from the comparative seal analysis. Results extracted from equivalent axisymmetric model configurations developed from 3-D wedge models and correlated with DIC data. ....	56
Table 4.10: Seal Length results from the comparative seal analysis. Results extracted from equivalent axisymmetric model configurations developed from 3-D wedge models and correlated with DIC data. ....	56
Table 4.11: Seal Number results from the comparative seal analysis. Results extracted from equivalent axisymmetric model configurations developed from 3-D wedge models and correlated with DIC data. ....	57
Table 5.1: Correlation coefficients for the final 3D-wedge model.....	58
Table 5.2: Sum Squared error values for the final 3D-wedge model .....	60
Table 5.3: Fast Fourier Transform sum squared error values for the final 3D-wedge model.....	61
Table 6.1: Table of design variables for make-up studies .....	69
Table 6.2: Table of load variables for service load studies.....	70
Table E.1: Sampling locations for the 1D example problem.....	83
Table E.2: Shape function contributions for the 1D example problem. ....	84

# Nomenclature

## English Symbols

$A(t)$	Amplitude of the maximum allowable slave node penetration
$A_i$	Initial amplitude
$A_{i+1}$	Final amplitude
$A_c$	Contact area
$a$	Inner radius
B	Box
$b$	Outer radius
$C$	The radius measured from the middle of the cylinder
$c$	Interface radius
$c_i$	Outer radius of the pin / inner member
$c_o$	Inner radius of the box / outer member
DC	Direct Current, used here as reference to a vertical offset
DIC	Digital Image Correlation
$DIC_i$	The $i^{th}$ point of the digital image correlation data set
$dA/dT$	First time derivative of the Amplitude
$d^2A/dT^2$	Second time derivative of the Amplitude
$dW$	The variation of work
$dU$	The variation in internal energy
$E$	Young's modulus
$E_0$	Initial estimate for the Young's Modulus
FEA	Finite Element Analysis
$FE_i$	The $i^{th}$ point of the finite element data set
FFT	The Fast Fourier Transform
FFT SSE	The Sum Squared Error of the Fast Fourier Transform
$F(x)$	The function of interest in the response surface problem
$\{F\}$	The vector of loads
$G$	The shear modulus
H	High
HH-PFBS	Geometry with high thread interference, high seal interference, fast pin taper, and slow box taper
HL-PNBN	Geometry with high thread interference, low seal interference, nominal pin taper, and nominal box taper
HL-PSBF	Geometry with high thread interference, low seal interference, slow pin taper, and fast box taper
$h$	The undeformed height of a seal surface element
$i$	Increment tracking variable
$J$	The polar moment of inertia
$j$	Increment tracking variable
$[K]$	The global assembled stiffness matrix
L	Low

$L$	The measured length of the seal contact region
$L_{DIC}$	The spatial length of the extracted Digital Image Correlation data set
$L_i$	The element seal face length
$L_{FE}$	The spatial length of the extracted finite element data set
LL-PSBF	Geometry with low thread interference, low seal interference, slow pin taper, and fast box taper
$l$	The length of the cylinder
$l_i$	The first direction cosine of the element face unit normal vector
$l_s$	The length coordinate along the seal contact region
$m_i$	The second direction cosine of the element face unit normal vector
N	Nominal
$N_{ij}$	The $j$ shape functions for element $i$
NN-PNBN	An ideal geometry with nominal thread interference, nominal seal interference, nominal pin taper, and nominal box taper
$n$	The maximum value of the tracking variable $i$
$n_i$	The third direction cosine of the element face unit normal vector
$\hat{n}_i$	The element face unit normal vector
$\hat{n}_{t,i}$	The unit vector tangent to the element face
OD	Outer Diameter
P	Pin
$p$	Threadform pitch
$p_i$	Inner pressure
$p_o$	Outer pressure
$p_s$	Composite cylinders interfacial pressure at point $c$
$R$	The radial direction
$r$	The radial direction
$S$	Standard deviation
SN	Seal Number
$SNR$	Signal to Noise Ratio
SSE	Sum squared error
T	Torque
$T_i$	The transformation vector
$t$	Step time
$t_i$	Initial step time
$t_{i+1}$	Final step time
$U$	Internal Energy
$U_0$	Internal energy density / strain energy density
$U_{0,n}$	Normal strain energy density
$u$	Displacement in the radial direction
$u_{box}$	Displacement in the radial direction of the box
$u_{pin}$	Displacement in the radial direction of the pin
$U_1$	The radial degree of freedom in an Abaqus cylindrical coordinate system
$U_2$	The tangential degree of freedom in an Abaqus cylindrical coordinate system
$U_3$	The axial degree of freedom in an Abaqus cylindrical coordinate system
$\{u\}$	The vector of nodal displacements

$\{\ddot{u}\}$	The vector of nodal accelerations
$V$	Volume
$\vec{V}$	Thread translation vector
$v$	Displacement in the circumferential direction
$w$	Displacement in the axial direction
$X$	An arbitrary constant used to conceal proprietary data
$x$	The axial nodal coordinate
$x_i$	A result extracted from model $i$
$x_{i-1}$	A result extracted from model $i$ with less degrees of freedom than $x_i$
$\bar{x}_{ij}$	Sample location
$x_0$	Initial estimate vector
$\{x\}$	Vector of design parameters
$y$	The radial nodal coordinate
$y_{ij}$	Nodal function values
$Z$	The axial direction
$z$	The axial direction

## Greek Symbols

$\alpha$	The yield offset
$\alpha_{11}$	Thermal expansion coefficient in the radial direction
$\alpha_{22}$	Thermal expansion coefficient in the circumferential direction
$\alpha_{33}$	Thermal expansion coefficient in the axial direction
$\alpha_0$	Initial estimate for the yield offset
$\beta$	Thread translation angle
$\gamma_{r\theta}$	Shear strain in the $r - \theta$ plane
$\gamma_{rz}$	Shear strain in the $r - z$ plane
$\gamma_{\theta z}$	Shear strain in the $\theta - z$ plane
$\Delta T$	Change in temperature
$\delta$	The displacement of the seal surface parallel to the element face unit normal vector
$\epsilon$	Total strain
$\epsilon_0$	The measured strain corresponding to $\sigma_0^o$
$\epsilon^o$	Offset yield strain
$\epsilon_{11}$	Strain in the radial direction
$\epsilon_{22}$	Strain in the circumferential direction
$\epsilon_{33}$	Strain in the axial direction
$\epsilon_n$	Strain in the direction normal to the element seal surface
$\epsilon_{rr}$	Strain in the radial direction
$\epsilon_{\theta\theta}$	Strain in the circumferential direction
$\epsilon_{zz}$	Strain in the axial direction
$n$	The hardening exponent for the plastic strain term
$n_0$	Initial estimate for the hardening exponent for the plastic strain term
$\theta$	The circumferential direction
$\mu$	Friction coefficient

$\nu$	Poisons ratio
$\sigma$	Stress
$\sigma^o$	Yield offset stress calculated from uniaxial tensile test data
$\sigma_0^o$	Initial estimate for the yield stress
$\sigma_n$	Normal component of the stress tensor
$\sigma_{rr}$	Normal stress in the radial direction
$\sigma_{\theta\theta}$	Normal stress in the circumferential direction
$\sigma_{zz}$	Normal stress in the axial direction
$\tau_{r\theta}$	Shear stress in the $r - \theta$ plane
$\tau_{rz}$	Shear stress in the $r - z$ plane
$\tau_{\theta z}$	Shear stress in the $\theta - z$ plane
$\phi$	The phase offset used in data set alignment
$\phi_{max}$	The maximum allowed phase offset
$\phi_{optim}$	The optimum phase offset

## Other Symbols

3D	Three Dimensions or Three Dimensional
% <i>Conv</i>	The percent convergence

# Chapter 1 Introduction and Motivation

## 1.1 Research Objective

Oil Country Tubular Goods (OCTG) are the collection of pipes used for the drilling and extraction of oil and gas. An oil well is comprised of several OCTG's joined by threaded connections. Modern oil wells primarily rely on a subset of these tubulars appropriately named “premium connections”. These connections are complex proprietary designs, and have been tailored to provide structural integrity for the well and ensure an effective connection seal for drilling and production fluids under extreme conditions. A steel manufacturer often produces dozens of families of connections, and each connection is made available in hundreds of variations to suit the needs of the well designer. A single well often requires several variants of premium connections, and the performance limits of each connection variant must be well understood to ensure a safe and successful well design. The connections can vary substantially in size, weight, and grade, however a common design feature in all premium connections is a reliance on a small metal-to-metal contact region for sealability. The current best practice for understanding connection seal performance limits is extensive testing under various conditions at a connection test facility. At a cost of several months and hundreds of thousands of dollars [1] a connection test qualification program is a burden for operators who seek a reliable characterization of minimum seal performance. Furthermore, very little insight into the mechanics of the connection can be gathered from current test methods. As a result, little is understood of what governs the sealing mechanism itself and reliance upon expensive testing procedures has developed. The objective of this study is to develop a methodology that can help reduce the amount of testing required to qualify an OCTG premium connection for field service.

## 1.2 Solution Hypothesis

The amount of required physical testing needed to qualify a connection can be reduced by the use of Finite Element Analysis (FEA) provided an accurate representation of the make-up condition has been achieved. Achieving an appropriate finite element make-up model is the most difficult aspect of connection modeling. It is in this make-up event that the metal-to-metal seal is generated by the interference fit of the box and pin in the seal region(s).

A process for reducing connection testing is outlined in the data flow diagram [2] of Figure 1.1. The process begins with an accurate parametric geometry from the connection manufacturer that is representative of a prepared test specimen. A finite element make-up model is generated based on the provided geometry, torque/turn data from the make-up event, corresponding strain and displacement measurements, and material test data. Parameters in the finite element model are tuned to achieve a make-up configuration that produces a minimum error fit of the experimental strain and displacement measurements. This minimum error model is realized by minimizing error metrics that utilize experimental data as the reference. Service loads are then applied to the minimum error make-up model to predict field performance. Once the performance of several connection variants is captured, connection performance can be interpolated between well bounded configurations. A more detailed data flow diagram for this process is provided in Appendix A.

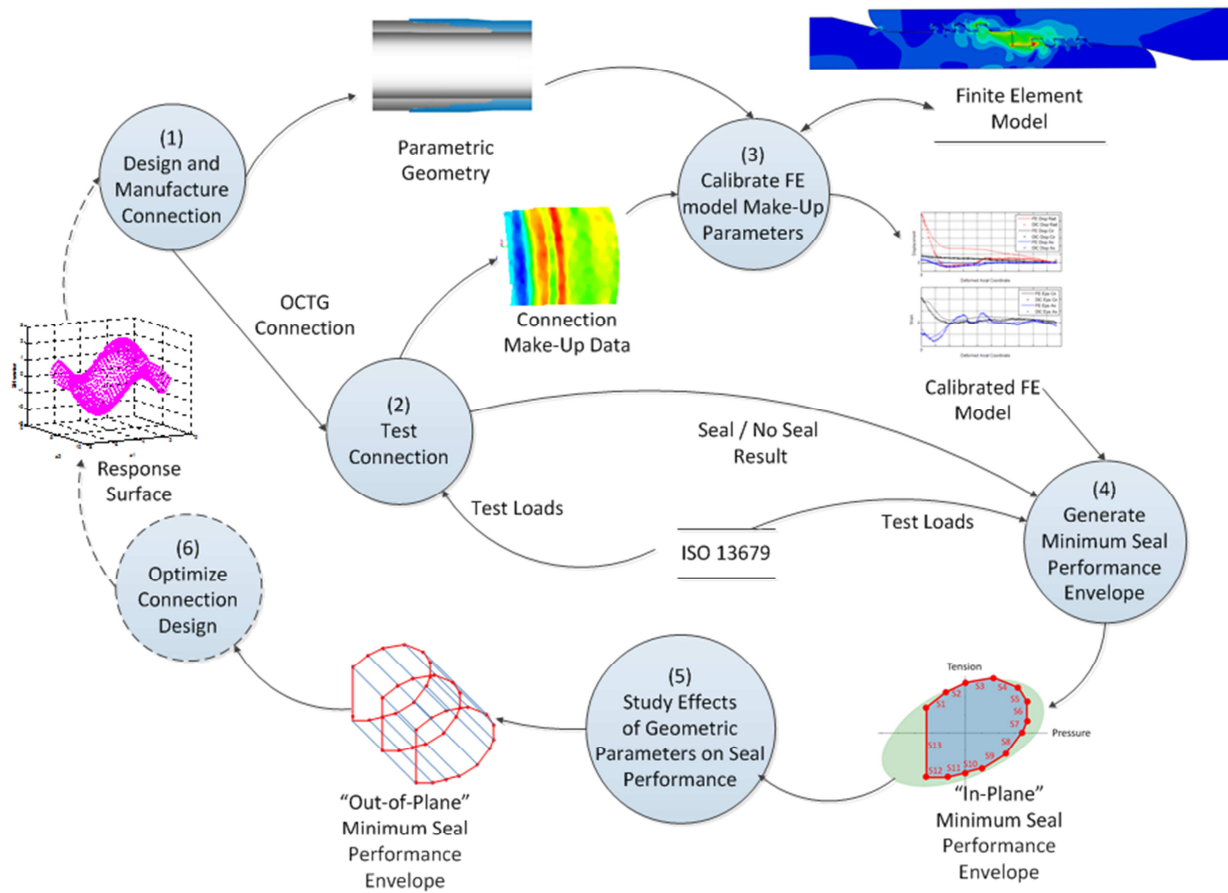


Figure 1.1: High level data flow diagram for the generation of a premium connection minimum seal performance envelope.

### 1.3 Problem Statement

The direct measurement of seal conditions at make-up is currently infeasible, and the best approximations are made from finite element models calibrated with strain gauge data. The make-up configuration has an immense impact on the ability of a connection model to accurately predict seal performance. Current axisymmetric modeling practice relies on axial offset assumptions at various locations to generate this make-up stress state. These axial offset assumptions are nonphysical and have little technical basis available in the public domain. For this reason, the goal of this modeling effort is to achieve a mechanics-based finite element make-up solution using only the manufacturer supplied geometry, connection test data, and commercially available finite element software.

### 1.4 Scope of Study

The focus of this work is the:

- Identification of best practices for premium connection DIC data acquisition and processing.
- Development of a tractable modeling technique that can produce a mechanics-based torque-rotation relationship for an OCTG connection.

- Replication of accurate connection make-up results in efficient axisymmetric pretension models.
- Development of quantitative metrics for connection seal evaluation.
- Development of quantitative metrics for the evaluation of model conformance to experimental data.

The simulation of connection performance under service loading is beyond the scope of this work. The interpolation of connection performance between well bounded configurations, as well as the response surface modeling and optimization of seal performance is also beyond the scope. A general outline for the response surface modeling approach is presented.

## **1.5 Discussion and Organization**

The thesis begins by establishing the need for greater spatial density in connection make-up experimental data so that connection models may be held to higher standards. Digital Image Correlation is introduced as a means to provide this higher standard. A technique for DIC imaging and data processing is presented, and the data quality is assessed.

With the experimental data in hand, the discussion turns to the finite element modeling technique. The great challenge of modeling premium connection make-ups is balancing the computational cost with the need for accurate results. The full 360-degree model is presented as the truest available representation, but found intractable because of its computational expense. Current axisymmetric modeling technique is evaluated and found sufficient for its computational efficiency, but lacking any documented technical basis for its assumed connection make-up boundary conditions.

A compromise is proposed which makes use of 3D-wedge modeling along with its own challenges. This modeling technique is revealed in full. 3D-wedge geometries are generated from manufacturer supplied axisymmetric profiles. Material models that permit a smooth transition from elastic to plastic behavior are constructed from minimum strength coupons. An efficient meshing method is presented to achieve 3D solutions in an acceptable timeframe. Several contact formulations are supplied to provide alternative paths for achieving good thread and seal contact resolution. The boundary conditions for the 3D-wedge make-up model are developed from a mechanics of materials basis and are applied to achieve experimental torque values.

With a 3D torque-rotation coupling achieved in the wedge model, a technical basis is available to guide the computationally efficient axisymmetric modeling effort. The 3D power-tight seal conditions are replicated in axisymmetric form using pretension sections, and the challenge of quantitatively evaluating the seal condition is presented. Several seal metrics are developed and evaluated in the power-tight configuration. An ability to converge the seal metrics is demonstrated and found crucial in characterizing seal behavior.

The 3D-wedge finite element model is then evaluated with respect to the uncompromising DIC data. Error metrics are used to quantify the fit of the box outer diameter displacement and strain signals through different but complimenting perspectives. Conclusions and recommendations for future efforts complete the write up.

## Chapter 2 Literature Review

This research is focused on achieving an accurate connection make-up model for the purpose of seal performance evaluation. It relies on the theoretical development of the connection stress state which has progressed from fundamental thick-walled cylinder theory to the use of finite elements. This work also relies on experimental techniques used in the oil and gas industry for connection qualification, and the use of optical metrology to measure displacement and strain fields.

### 2.1 Connection Make-up Modeling

Weiner [3] was the first to present the industry with a method of stress analysis for tapered threaded connections and lay the mathematical foundation for analysis of connection and seal performance. He makes simplifying assumptions to reduce the complex geometry of an API connection to a tractable axisymmetric linear elasticity problem.

Hilbert and Khalil [4] lay the groundwork for axisymmetric finite element modeling of premium connections while acknowledging that there is, “currently no verified, reliable, and general correlation between make-up torque and torque shoulder interference. Therefore a parametric study of the effect of increasing torque shoulder interference is usually conducted” of which they give no further detail. They maintain that the axisymmetric assumption produces accurate stress and strain calculations but do not distinguish this between calculations of an assembled connection under service conditions and the connection make-up event. They reinforce the importance of nonlinear material models for seal use and make use of multilinear material models in their work. They also implement contact algorithms based on master and slave surface penetration rather than relying on node-based ties. They begin the work of identifying worst case performance by testing and modeling the tolerance extremes of each connection, and begin the correlation of their finite element models to experimental strain gauge data.

The ExxonMobil Connection Evaluation Program documentation [5] requires prospective connection suppliers to submit geometries with a built-in torque shoulder interference of 0.001 inches. This torque shoulder interference is, “measured at the mid-point of the shoulder when the interference of the closest seal is just resolved (i.e., to measure the shoulder interference, translate the pin geometry radially until the seal surfaces are just in contact)”. This supplied geometry is then used to generate “forecasted performance envelopes” for each connection irrespective of the connection make-up torque. While Exxon acknowledges that make-up torque has an effect on sealability and claims the use of strain measurements to calibrate their connection make-up assumptions [1] there does not seem to be a well-defined process for this crucial modeling step in the public domain.

Dvorkin provides good insight into the element requirements for effective axisymmetric seal modeling, agrees that node-to-node contact algorithms are insufficient for modeling large sliding situations, and reinforces the need for nonlinear material models [6]. He shows the extreme extent of plasticity in the seal region during overtorque situations, and provides an example of a traditional finite element model validation based on standard strain gauge experimental data.

## 2.2 Evaluation of Performance Limits

The extensive testing process for OCTG connections is outlined in ISO 13679 [7]. The immense expense of connection testing has motivated the investigation of inferring untested connection performance based on previously completed tests. Heijnsbroek [8] acknowledges that by using extensive finite element modeling coupled with physical testing, “it might be possible to interpolate between test results of various diameters”. Powers [9] defines product families which “extend physical test results” based on “thread and seal interference magnitudes, thread pitch and taper, seal taper, torque shoulder taper, among other details”. Khemakhem [1] later extends Powers’ work to define finite-element-based, “characteristic performance factors, such as sealability factor, structural integrity factor, galling resistance factor, environmental resistance factor, [and] fatigue resistance factor” to infer the performance of a large group of connections based on the experimental performance of only a few.

## 2.3 Sealing Criteria

Concrete OCTG sealability requirements are difficult to find and often debated, however sources are available which allude to contributing factors. Hilbert and Khalil [4] evaluate seals based on the seal contact stress “length, height, enclosed area, and general shape”. They also note that, “since the mechanics of the seal can be affected by interaction with the torque shoulder, it is important to plot both seal and torque shoulder contact stresses”. Sugino [10] offers a “normalized seal contact energy” metric where the contact pressure is integrated over the seal length. Dvorkin [6] offers seal metrics using seal length, peak contact stresses, and extends Sugino’s method to incorporate internal pressure values by integrating the pointwise difference between seal contact stress and connection internal pressure. Heijnsbroek [8] performs fundamental background work on seal characterization. His experimental focus is conical metal-to-metal seals with the goal of identifying the main factors driving sealability. His work compares the advantages of high contact stresses over short seal lengths with lower contact stresses distributed over larger seal areas. He aides the effort of prioritizing the factors of sealability by using his experimental data to show that “sealing is mainly determined by axial displacement” (39).

Heijnsbroek concludes that plastic strain is a requirement for sealing, an assertion that many in the industry disagree with. Because of his academic affiliation, he is the only source with the freedom to reveal a quantitative requirement for OCTG sealability.

## 2.4 Strain gauging OCTG’s and Digital Image Correlation

The use of strain gauge measurements to verify OCTG makeup models can be traced back at least as far as Weiner [3]. The challenge with this measurement approach is the limited spatial resolution available. Hilbert and Khalil [4] reveal that preliminary finite element models are used to guide gauge placement prior to make-up. They acknowledge that this, “placement of gauges frequently misses locations of high strain or stress, due to the overall complex behavior of the connection”. Finite element models are then provided with the claim that, “the FEA detects peak strains that the gauges miss”. However, by examining the relatively sparse strain gauge data provided, it could easily be argued that the strain gauges are collecting accurate information and the model is missing the mark. To make such bold claims in regard to modeling capability requires greater spatial resolution in the experimental data.

Digital image correlation has the ability to provide this increase in spatial resolution as shown in Chapter 3. Sutton [11] has presented a detailed basis for Digital Image Correlation including the bundle adjustment technique used to generate a 3D representation from multiple 2D images of a calibration panel taken from different viewpoints. A useful procedure for determining the sensitivity and accuracy of an ARAMIS system configuration is provided by Schmidt [12,13]. A series of articles by Reu [14–17] also provides a helpful overview of Digital Image Correlation shape functions as well as recommendations for speckle patterns. Reu recommends averaging points at the same radius in an axisymmetric body to reduce measurement noise. He also maintains that the displacement measurement should be given priority over any subsequently calculated strain value because it is the primary measurement of a DIC system.

# Chapter 3 Digital Image Correlation

## 3.1 Motivation and Description

Replicating the make-up condition of a connection in a finite element model is a challenging task which typically relies on the use of strain gauges. However, strain-gauge data is typically only available at select points along the pipe axis and circumference. The typical application of strain gauges does not provide enough spatial resolution to properly capture the complex strain fields as demonstrated in Figure 3.1. In addition, current practice in industry relies on the finite element model to determine proper strain gauge placement [4]. This typically produces some issues in the test lab as even small variations in strain gauge placement can produce large variations in recorded strain values.

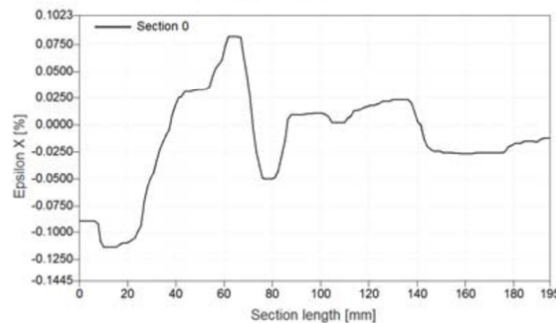


Figure 3.1: Axial strain vs. axial length of a commonly used OCTG premium connection after make-up. Used with permission of Hess Corporation [18].

Recent advances in the field of Digital Image Correlation (DIC) have produced a tool that can yield a more precise representation of a premium connection make-up. The ability of the DIC to capture high-spatial-resolution full-field displacement and strain data means that finite element connection models may now be held to higher standards. DIC systems have the ability to produce 3D displacement and strain fields rather than merely recording strain at discrete points. As a result, a more comprehensive picture of the connection state is available than traditional strain gauge arrays can offer. DIC systems can capture full-field strain features easily missed by sparse gauge placement. DIC systems also eliminate gauge location issues because they do not rely on a pre-existing model to determine where the strain is sampled. DIC measurements can provide high-spatial-density full-field validation data for finite element models of OCTG premium connection make-ups if an appropriate correlation technique is used to relate the displacements and strains on the outside of the pipe connection make-up zone. A validated FE model can then be used to better represent the connection performance under service loads.

## 3.2 DIC Calibration

A DIC data set is only as credible as its calibration. Calibrations are performed using certified calibration panels. Several images of the calibration panel are taken in precise orientations and a photogrammetry process known as bundle adjustment is used to determine the geometric orientation of the cameras with respect to the calibrated volume. Extreme care must be taken in this process to ensure a quality DIC data set for correlation to predictions from finite

element models. In addition, the cameras and test specimen should be well isolated from any source of vibration whenever possible.

### **3.2.1 Fiduciary Marks**

Several fiduciary marks must be introduced in the images to provide a basis for

- 1) Mapping the DIC data back to the geometry
- 2) Accounting for rigid body motion in the system.

The marks indicating the axis should be inscribed on the pipe itself at several circumferential locations within the field of view, and should be close to the edges of the calibrated volume to provide the greatest accuracy in the pipe axis designation. Great care should be taken to ensure that the fiduciary marks used for the purpose of rigid body motion subtraction remain completely stationary throughout the DIC data acquisition.

The rigid body reference fiduciary marks should be pushed to the edges of the calibrated volume to provide the greatest accuracy. In an ideal case, vibration isolated laser pinpoints would be projected onto the imaged surface in well documented locations. Doing so provides the analyst with a means to properly account for rigid body translations and rotations as the connection make-up progresses.

## **3.3 Data Acquisition**

Several tolerance variants of a common industry connection were selected for make-up studies. The ARAMIS system [19] was set up and calibrated as shown in Figure 3.2. Further guidelines on best practice experimental setup are provided in Appendix B. A random paint pattern was applied to the outer diameter of the box in the connection make-up zone. The outer diameter of the box was imaged before, during, and after the connection make-up. Several images were taken as the make-up progressed, and the ARAMIS system computed the relative displacement of the paint pattern in successive images as demonstrated in Figure 3.3. Strain and displacement data is made available through the software as shown in Figure 3.4. To compute the image deformations a facet size of 25x25 pixels was chosen with a 15-pixel overlap between facets. This image processing technique produced calibrated high-spatial-density full-field output images on the outer diameter of the box with data points arranged in a grid. Both strain and displacement data were extracted.

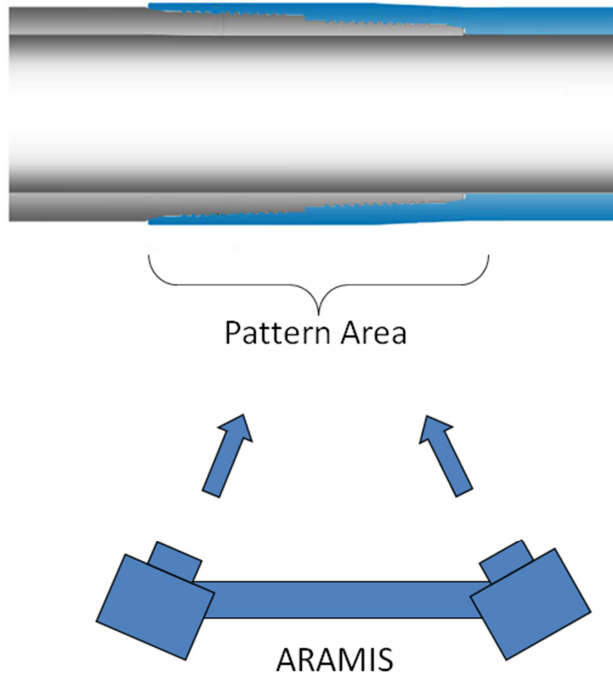


Figure 3.2: Diagram illustrating the ARAMIS experimental setup. Used with permission of Hess Corporation [18].

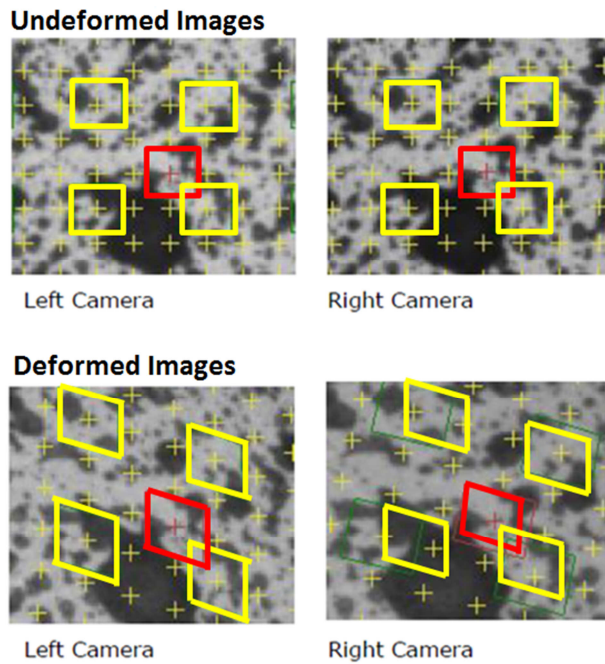


Figure 3.3: Demonstration of pattern tracking during deformation. Undeformed left and right camera images (top) and deformed left and right camera images (bottom). Used with permission of Trilion Quality Systems [19].



Figure 3.4: The random paint pattern applied to the box with axial strain output overlaid (left). A GOM ARAMIS DIC camera system (right). Used with permission of Trillion Quality Systems [19].

### 3.4 Error and Precision in the DIC

Because of the orientation of the DIC system to the connection during the test, there is a variation in precision depending on the component of displacement or strain. Statistical analysis of the DIC images reveals differing noise levels for the desired output quantities. The radial results measured out of the plane of view contain more noise than the axial and circumferential results measured in the plane of view.

This can be seen in the standard deviation and the signal-to-noise ratio of the DIC data at the final make-up frame. The standard deviation provides an indication of the amount of noise in the signal. The signal-to-noise ratio is the ratio of the dynamic range of the signal to the standard deviation as shown in Equation (3.1).

$$SNR = \frac{Max - Min}{S} \quad (3.1)$$

Where  $SNR$  is the signal-to-noise ratio,  $Max$  and  $Min$  are the maximum and minimum values of the signal, and  $S$  is the standard deviation of the signal.

From Table 3.1, it can be seen that there is consistently more noise in the radial displacement signal than that in the axial and circumferential displacement signals even though the radial  $SNR$  is greater. The standard deviation for the radial displacement signals was on average six times greater than those of the in-plane axial and circumferential displacement measurements.

Table 3.1: Statistics for DIC data.

	Radial Disp (mm)	Tangential Disp (mm)	Axial Disp (mm)	Tangential Strain (-)	Axial Strain (-)
<b>HL-PSBF</b>					
Standard Dev	2.11E-02	1.08E-02	9.52E-03	5.07E-04	8.51E-03
SNR	4.15	3.05	3.85	4.56	0.34
<b>LL-PSBF</b>					
Standard Dev	6.12E-02	1.12E-02	1.03E-02	4.18E-04	5.97E-04
SNR	5.11	3.38	4.19	5.25	4.06
<b>HH-PFBS</b>					
Standard Dev	6.11E-02	4.72E-03	9.70E-03	7.54E-04	1.01E-03
SNR	5.97	3.22	4.05	4.48	3.03

Two minor issues in the DIC data caused some error. A few locations along the box had inadequate lighting and/or a poor paint pattern. This resulted in voids in the computed full-field strain image. The voids are present in less than 1% of the total field. The second issue was a slight misalignment between the pipe axis and the camera orientation. Because of this, the image computation grid orientation was roughly 6 degrees offset from the assumed axial ‘X’ and circumferential ‘Y’ directions as shown in Figure 3.5. While the error induced here is small, future imaging should include fiduciary marks to orient the image with the natural cylindrical coordinate system of the pipe.

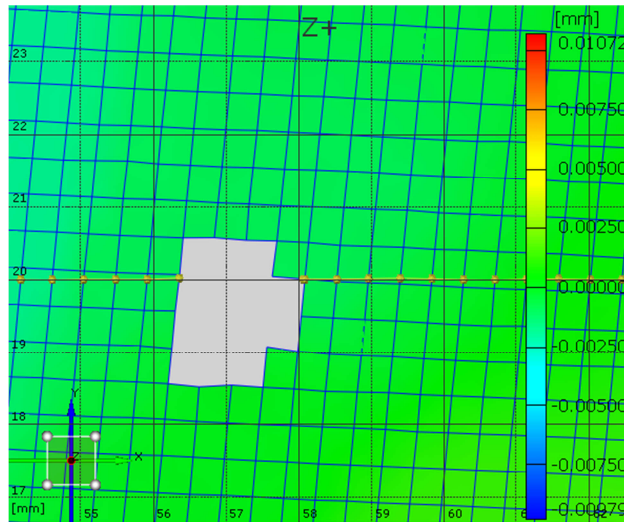


Figure 3.5: Two issues with the DIC data are highlighted. Inadequate lighting and/or a poor paint pattern in some areas produces a void in the computed data fields. The small offset between the image computation grid (blue) and the assumed system coordinates (black) produces a coordinate mismatch which prevents equal spacing between extracted section points (gold).

To overcome these issues and achieve a robust estimate of the DIC data fields, the output quantities are extracted at five sections designated by their circumferential coordinates. The five extraction sections were centered around an axis parallel to the pipe axis and closest to the cameras. Each section consists of approximately 450 data points. As shown in Figure 3.7 and Figure 3.8, there exists some variation in the DIC data fields with respect to the circumferential direction due to the mapping of the convex connection surface to a flat Cartesian plane for

extraction. This circumferential variation must be carefully eliminated in order to properly correlate the DIC data to an axisymmetric finite element model which does not allow for variation in the displacement or strain fields in the circumferential direction.

To collapse this data into a usable form, a median process was developed. The five sections are sampled at a desired axial coordinate. Because the differences in the alignment of the coordinate systems between the DIC image and the pipe/FE model coordinate system lead to the error described in Figure 3.5, a section point is not always available for extraction at a desired coordinate. To overcome this, the output variable of the closest section point is taken to be representative for that desired coordinate. This produces five output samples for each desired axial coordinate. The median value of these five output samples is recorded as the robust estimate of the DIC data, and passed on for correlation with the output of the finite element model.

## 3.5 Data Processing, Reduction, and Alignment

### 3.5.1 DIC Coordinate System Definition

Because fiduciary marks were not available to directly orient the DIC data sets, an alternative method was used to define the DIC coordinate system. Doing so allows the data exported from the DIC software to be registered with the natural coordinate system of the connection.

A least squares error method was used to project a best fit cylinder on the imaged surface. The axis of this best fit cylinder was used to define the DIC coordinate system as shown in Figure 3.6. By design, the connection imaged did not have constant outer diameter (OD) in the connection region. Because of this variation in the OD, the best fit cylinder needed to be tailored to fit the area of greatest interest. The strongest displacement and strain signals for this particular connection were found between the connection shoulder and the outer seal. The area of the images chosen for the cylinder fitting extended from the outer seal to the shoulder in the axial direction, and from the bottom extraction set to the top extraction set in the circumferential direction. This measure forced the greatest coordinate system accuracy in the region of greatest interest. The DIC field data on the surface of the connection was transformed into the newly defined coordinate system.

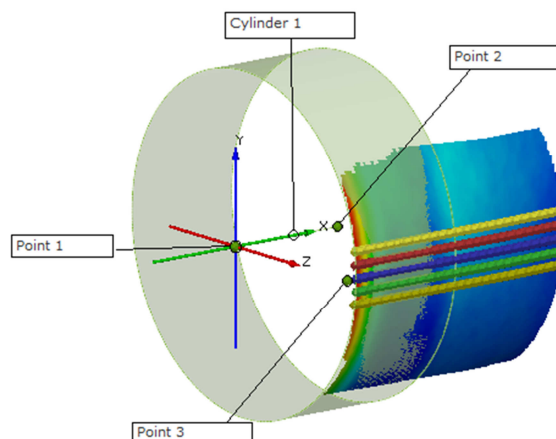


Figure 3.6: The fitted cylinder used to orient the DIC data. The coordinate system was defined by points projected from the image surface to the axis of the cylinder primitive.

A powerful advantage of the ARAMIS system is that the geometry can be measured as well as the deformation and strain of a body. This can come into great use when trying to reconcile DIC data with finite element models. As a check, the box outer diameter should be measured in the test facility and checked against 1) the DIC best fit cylinder diameter in the original undeformed state 2) the API outer diameter tolerance specifications for the given connection and 3) the outer diameter of the box in the finite element model. The reason for this is that a small variation in outer diameter can have a large impact when trying to reconcile displacement and strain fields, especially in the tangential direction. The outer diameters of the DIC data and the manufacturer supplied geometry in this study were found to be in agreement to within 0.2%.

### **3.5.2 Removing Rigid Body Motion**

As the make-up progresses, there is a tendency for the pipe to translate and rotate in the rigid body mode. When trying to measure small elastic deformations, the identification and subtraction of the rigid body mode is essential. Because stationary fiduciary marks were not available in the images to give a proper reference, the best practice of rigid body subtraction was to identify the region of the images with the smallest displacement throughout the make-up. The region of least deformation on the box outer diameter was found to be the area furthest from the outer seal as shown in Figure 3.7. The mean displacement of this region was first calculated and then subtracted from the full displacement field, thus removing the rigid body translation as much as possible.

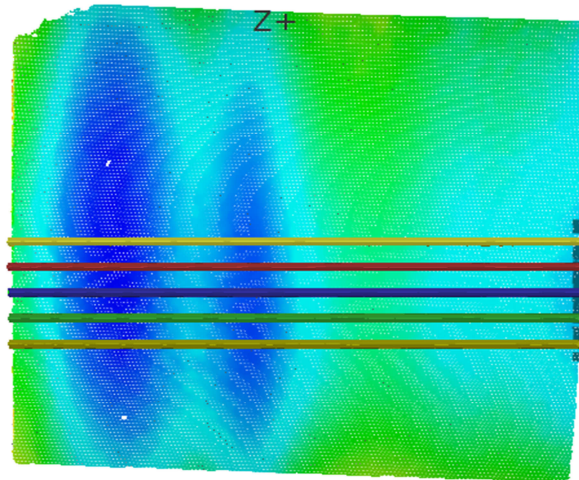


Figure 3.7: The region of least deformation used to identify the rigid body mode is shown in dark grey to the far right of the image. The extraction set locations are shown plotted over the result, and are designated by circumferential coordinate.

One consequence of using this rigid body motion removal technique is that the displacements are forced to zero at the far right of the extraction sets as shown in Figure 3.8. While the true value of the displacement field may not be zero in this location, the technique opens the door for the creation of a common reference point between the DIC and the finite element model. Displacements can now be measured and correlated relative to the far right pixel of the image. The strain signals are not affected by this procedure because they are spatial derivatives of the displacement field and not subject to rigid body offset.

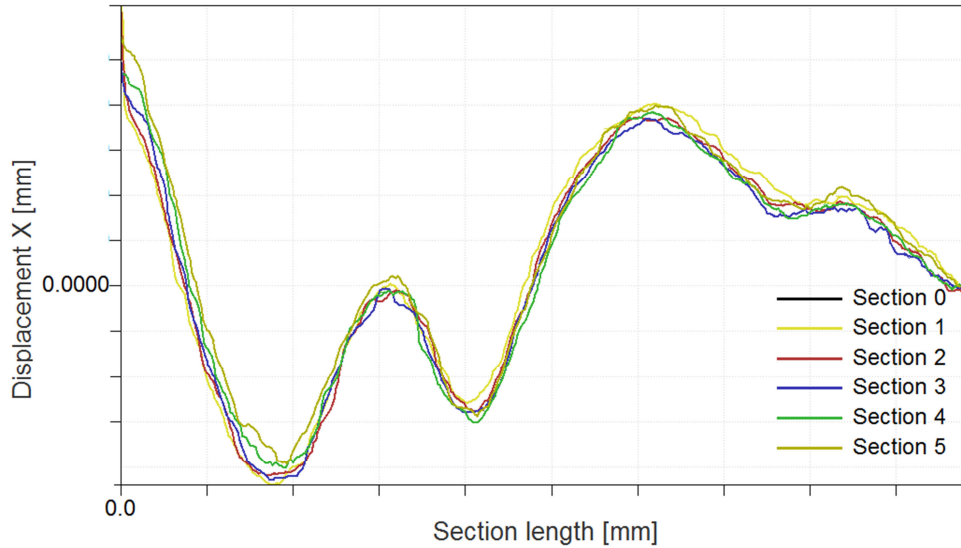


Figure 3.8: The extracted results from Figure 3.7. The displacement results are forced to zero at the far right of the extraction sets. The extracted axial displacement data is shown plotted as a function of the axial coordinate.

### 3.5.3 Data Extraction

The five output variables selected for extraction are the axial, circumferential, and radial displacements as well as the axial and circumferential strains. The radial strains were not extracted because the noise levels in this out-of plane strain measurement were too high for a reliable reading. The value of extracting both strains and displacements cannot be overlooked. The strength of the experimental displacement signals is the ability to calibrate the model to the scales of the connection behavior. The strain signals offer the ability to represent the trends present in the mechanics of the system. The displacement and strain data was exported in text file format from the ARAMIS software for further processing in MATLAB.

### 3.5.4 DIC Filtering

#### 3.5.4.1 Filtering by Discrete Operators

The ARAMIS software package offers several filtering options using discrete operators such as average, median, and gradient filters. These tools have the advantages of a quick and easy method to access and visualize an arbitrary DIC data field. Their disadvantage is that they attenuate the signal because they are an inherent smoothing operation. This attenuation can be cause for concern when trying to identify the peaks of a displacement or strain signal, especially if the signal is over filtered. In addition, generic discrete operators do not take the mechanics or features of the imaged system into account when operating on the data.

#### 3.5.4.2 Filtering by Spatial Frequency Content

An alternative to using discrete operators to filter a DIC signal is to make use of the Fast Fourier Transform to identify the spatial frequency content of the signal. The FFT provides an orthogonal view of the DIC data as illustrated in Figure 3.9. Separating out the spatial frequency components of the signal allows the signal to be reconstructed using the inverse FFT using only the low frequency content as demonstrated in Figure 3.10.

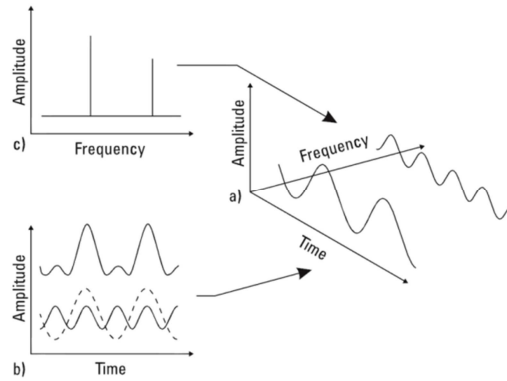


Figure 3.9: The relationship between the time and frequency domains. a) Three-dimensional coordinates showing time, frequency, and amplitude b) Time domain view c) Frequency domain view. © Agilent Technologies, Inc. 2000. Reproduced with Permission, Courtesy of Agilent Technologies, Inc. [20].

The ideal cutoff frequency varies between data sets, but a good starting point is the thread pitch of the connection because, in general, no feature of interest exists in the displacement or strain signals above the thread pitch frequency. This technique permits us to apply knowledge of the mechanics of the system at hand in our filter design. A disadvantage of this filtering technique is that by removing the high frequency content we are removing energy from the signal and the inverse FFT has difficulty representing the end conditions. The cutoff frequency should be tailored such that the error in representing the original signal is kept to a minimum. To evaluate the fit of the inverse FFT, the residuals should be closely monitored. A residual signal with a mean zero random distribution and small random amplitudes is desired.

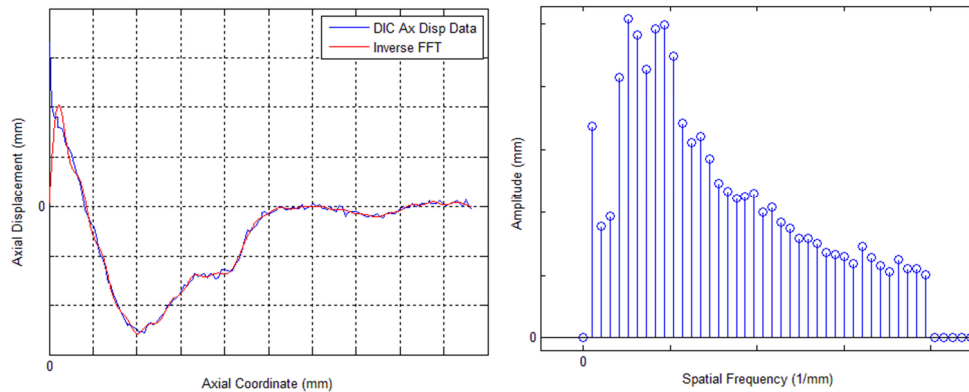


Figure 3.10: FFT Filtering demonstrated on a sample DIC extracted set. To the left, the original extracted signal in blue, and the reconstructed inverse FFT signal using only low frequency content in red. To the right, the spatial frequency content of the filtered signal after the high frequencies have been thrown out.

To perform an FFT, the signal must be sampled at evenly spaced intervals and the number of samples must be a power of two. Prior to performing the FFT, the signals were resampled at 1024 equally spaced points. To reduce the poor representation at the edges, the signal was mirrored to force the signal to be periodic in the window. The FFT was performed and the frequencies above the cutoff were replaced with zeros as shown in Figure 3.10. An inverse FFT was performed on this data and the filtered signal was passed for correlation to the finite element model.

# Chapter 4 The Finite Element Make-up Model

The direct measurement of seal conditions at make-up is currently infeasible, and the best approximations are made from finite element models calibrated with strain gauge data. The make-up configuration has an immense impact on the ability of a connection model to accurately predict seal performance. Current axisymmetric modeling practice relies on axial offset assumptions at various locations to generate this make-up stress state. These axial offset assumptions are nonphysical and have little technical basis available in the public domain. For this reason, the primary goal of this modeling effort is to achieve a mechanics-based finite element make-up solution using only the manufacturer supplied geometry, connection test data, and commercially available finite element software.

## 4.1 Overview of a Premium Connection Make-up

There are many variations of premium connections, but most have similar components with specific functions in the make-up process. Figure 4.1 illustrates an axisymmetric cross section of a generic integral connection with a mid-shoulder and two seals. The box is the outer (female) member; the pin is the inner (male) member.

A make-up begins when the pin and box are lubricated. The pin is aligned by hand and twisted to “hand-tight” with the box held fixed. Tongs are placed on the box and pin at approximately one-diameter’s length from the connection region. The pin is then rotated to “shoulder-tight” where the shoulders of the two members come into contact. To this point in the make-up the only torque generating mechanism of the connection is the radial interference of the thread features. The shouldering point can be easily identified as a spike in a plot of torque vs. rotation.

The pin is further rotated by a hydraulic torque wrench to “power-tight” at a manufacturer specified torque range. It is in this power-tight phase of the make-up that the seals are generated by the action of a more compliant member riding an inclined plane in a manner analogous to a cam follower. The shoulder is the surface perpendicular to the pipe axis that functions like a bearing surface for the threads to work against. The shoulder also serves as a gauging point to align the seals in their proper axial locations. As the torque is applied, the threaded sections are elastically stretched as the pin translates to the right as shown in Figure 4.1.

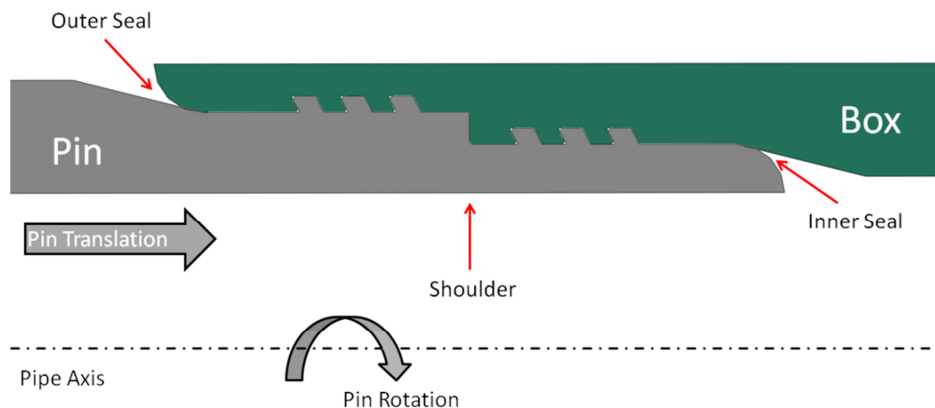


Figure 4.1: A generic axisymmetric connection geometry shown in the shoulder-tight configuration.

## 4.2 Reducing Run Time

### 4.2.1 The Full 3D Model

The truest available finite element model of a connection make-up is a full 360-degree representation of the box and pin using 3D continuum elements. This representation has no associated modeling assumptions. The geometry, boundary conditions, loads, and stiffness distributions can be represented exactly. Unfortunately, this type of model is often intractable because of

- 1) The extreme geometric complexity of the connection
- 2) The overall aspect ratio of the connection
- 3) The level of mesh refinement required to achieve an acceptable seal solution
- 4) The number of degrees of freedom required to calculate a 3D continuum element solution

A 360-degree representation of the desired connection at an acceptable level of convergence would likely require over 1 million 3D brick elements. Such representations were attempted but the solution was found to be intractable with the time and resources available. As a result, modeling assumptions were made to reduce run times and achieve a working solution.

### 4.2.2 The Axisymmetric Form

OCTG connections are usually modeled in an axisymmetric form. The axisymmetric assumption is valid for models that meet the following requirements:

- 1) There is no variation in the geometry with respect to the circumferential coordinate.
- 2) There is no variation in material properties with respect to the circumferential coordinate.
- 3) There is no variation in loading with respect to the circumferential coordinate.
- 4) There is no variation in displacement with respect to the circumferential coordinate.
- 5) There is no radial rigid body displacement.

When recognized and appropriately exploited, axisymmetry can reduce the number of degrees of freedom in a finite element model considerably while maintaining sufficiently accurate solutions. For decades, OCTG models have applied the axisymmetric assumption to make the problem tractable. However, OCTG connections are not axisymmetric because the helix angle of the thread form causes a variation in geometry with respect to the circumferential coordinate. In addition, the mechanism of rotating the pin at make-up results in a variation in the displacement field with respect to the circumferential coordinate. Such a variation in displacement under an applied torque can be easily seen in the analogous cantilevered torsion bar problem. For these reasons, an axisymmetric model does not have the degrees of freedom required to represent the geometry or the true connection behavior.

The mechanism often employed to simulate the applied torque in an axisymmetric connection make-up is the pretension section, also known as a bolt load [21]. This load method was originally developed for use in bolted joint analysis and its intention is to mimic the effect of a bolt with minimal computational effort. A traditional application of a pretension section is the modeling of a bolted flange. In this type of analysis, the length of the bolt shank can be artificially shortened in order to study the flange and gasket members in compression. The object of this type of study is rarely the bolt itself, but rather the members under the effects of the

bolt. It is an efficient loading trick for a problem of this caliber, but its modeling capacity is limited.

In the implementation of a pretension section load, there is no inherent link between the pretension section offset and the torque applied to the bolt, but rather the force-displacement coupling is assumed and artificially inserted by the user. The application of a pretension section also assumes that the distributed elasticity of the bolt can be represented by an axial offset at a single point.

Pretension sections have been extended and applied in the analysis of OCTG premium connections in an effort to simplify the loading mechanism by only considering the axial component. They operate by defining an axis of rotation and a perpendicular surface that cuts through the connection member. A layer of elements on this perpendicular surface is designated in the box and pin. This layer of elements is then dilated or contracted by a certain distance to mimic an axial advance of the pin into the box as shown in Figure 4.2.

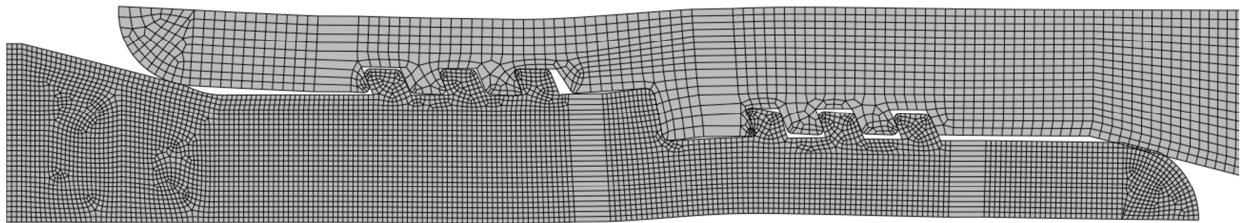


Figure 4.2: An axisymmetric pretension section using four dilated pretension sections. The deformations have been exaggerated for visualization purposes.

The pretension section scheme can effectively place the shoulder and seals in compression. However, a plot of the axial displacement field will reveal that the loading mechanism is entirely nonphysical as shown in Figure 4.3.

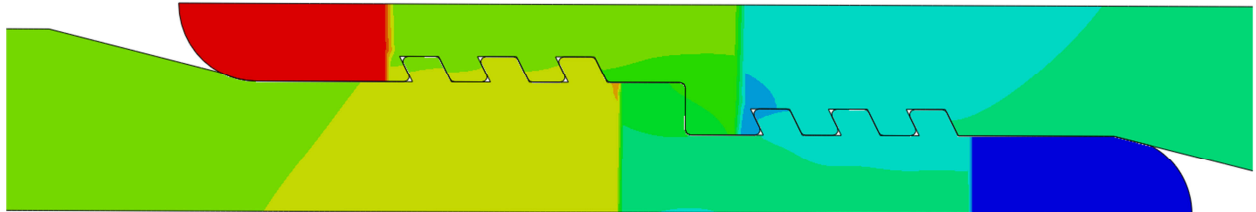


Figure 4.3: The axial displacement field of an axisymmetric pretension model.

The axial displacements are extracted on the box outer diameter as shown in Figure 4.4. A clear point of singularity can be seen in the axial displacement field, but cannot be detected from the radial displacements. Similarly in a plot of strain or stress components the effects of the pretension section mechanism are easily masked. A plot of von Mises stress further masks this mechanism to the point that it is nearly undetectable. Because the pretension sections can be dilated or contracted independent of any force-displacement relationship, the displacement and strain fields can be tuned at discrete points to correlate perfectly with experimental strain gauge measurements.

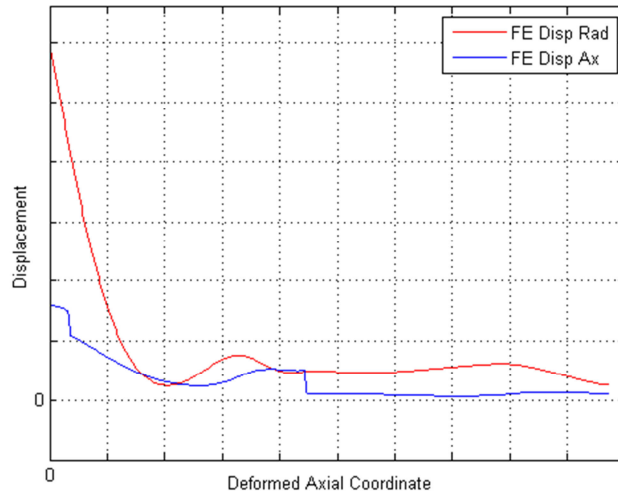


Figure 4.4: The extracted axial displacement field.

However, when attempting to reconcile these displacement results with full-field DIC data as shown in Figure 4.5, the inherent flaws of the modeling technique become painfully apparent. This axisymmetric pretension section modeling technique can only achieve a very limited level of correlation even when optimized. Furthermore, application of pretension sections often applies identical offsets in different locations of the connection. This practice neglects the difference in stiffness in the regions above and below the shoulder as well as the difference in stiffness between the box and pin.

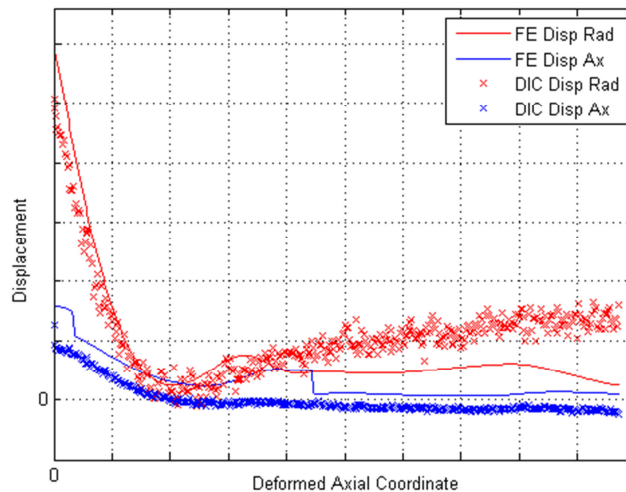


Figure 4.5: The resulting axial displacement field overlaid on the DIC displacement data.

A pretension section can only be deemed an acceptable representation of a connection make-up if a concrete, mechanics-based link is made between the applied torque and the axisymmetric displacement field. Relying on a turn-pitch calculation to determine the axial offset at the pretension section neglects the fact that the connection is a complex distributed elastic system. To find the link between the applied torque and a representative axisymmetric displacement field, a 3D representation is required.

### ***4.2.3 The 3D-Wedge Assumption***

A middle ground between the full 3D model and the axisymmetric formulation was investigated by modeling a sector of the full box and pin. This 3D-wedge model offers the ability to capture the torque-theta relationship with considerably fewer degrees of freedom than the full 360-degree representation if a few assumptions are made:

- 1) The displacement field is representative of the 360-degree model at the center line of the wedge section.
- 2) The torque load is evenly distributed with respect to the circumferential direction.
- 3) The boundary conditions at the cut-planes are representative of the unmodeled cylinder section.

The wedge model pushes closer to the full 3D representation than the axisymmetric model because the circumferential degree of freedom is activated. This ability to capture variation in circumferential displacement allows the model to investigate the torsional stiffness of the members. Most importantly the kinematic relationship between the rotation and axial advance of the pin is now available.

## **4.3 Geometry**

### ***4.3.1 Axisymmetric Geometries***

It is essential to have an exact representation of the test geometry because slight variations in tolerances or thread profiles can result in large seal performance variations. Whenever possible, the geometries should be acquired directly from the manufacturer and should be generated in a format that relies on lines and radii specifications rather than spline representations. This will allow for easier model partitioning in later modeling steps.

### ***4.3.2 3D Geometry from Axisymmetric Geometries***

Because many manufacturers do not model connections in 3D, the wedge models were constructed by revolving the axisymmetric profile through a sweep angle. This can be a challenging procedure and requires careful consideration and manipulation of the geometry.

The thread helix angle causes a variation of geometry with respect to the circumferential coordinate in the threaded regions, but not in the shoulder or seal regions. To overcome this discrepancy, the original axisymmetric profile is split into five main sections and four transition regions as labeled in Figure 4.6. Each section is revolved through the sweep angle, and a helix revolution is specified for the threaded sections according to the pitch of the thread form. The five sections are later merged and all interior features are discarded as illustrated in Figure 4.7.

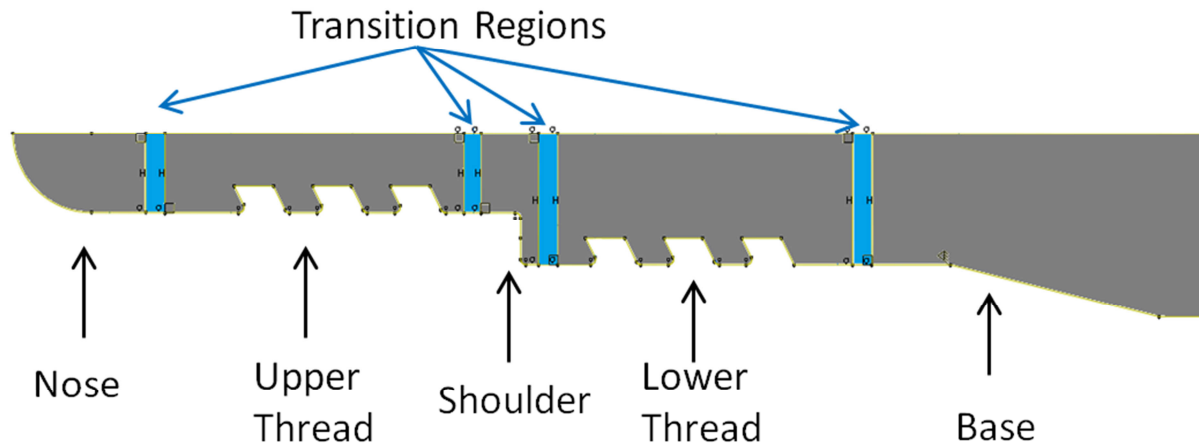


Figure 4.6: Simplified axisymmetric profile illustrating the cut-planes and transition regions used to generate the 3D swept sections. The Nose, Shoulder, and Base sections are revolved without a helix angle. The threaded regions include a helix angle in the revolution.

To make this merge possible, cuts are made in the axisymmetric profile such that an axial overlap creates a transition region between the five sections. The axial length of this transition region corresponds to the axial advance of the threaded section due to the helix when swept through the revolution angle. To ensure that the revolution and merge operations are executed flawlessly, the cut-planes must be perpendicular to the axis of revolution. Similarly, the transition regions work best when they are bounded on the inner and outer diameters by edges parallel to the axis of revolution. To ensure this, the geometry may require slight modification.

The axial length of the transition regions should be given an additional margin to prevent an acute angle from forming in the merge operation between the helix swept threaded regions and the flat swept seal and shoulder regions. If a severely acute angle is formed in the transition region by the merge operation, aspect ratio issues will be inevitable in the meshing phase.

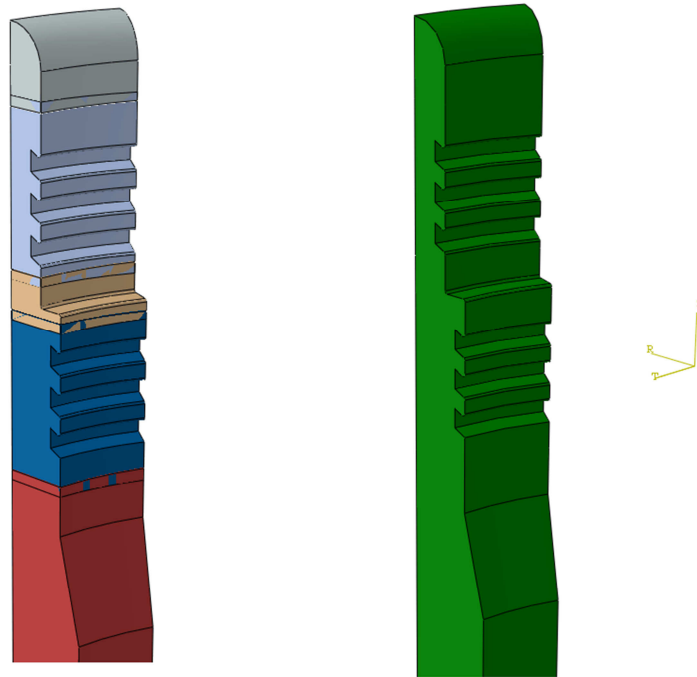


Figure 4.7: The five 3D swept regions with transition regions before (left) and after (right) the merge operation. All interior surfaces are discarded and the single solid part remains.

The geometries for box and pin are generated so that they can be instantiated in the shoulder tight configuration. Once instantiated, a contact resolution method is used to resolve the thread and seal interferences as discussed in Section 4.6.

## 4.4 Material Models

To characterize minimum seal performance for a given connection, the worst case material properties must be assumed. In order to identify these minimum strength material properties for modeling purposes, an extensive material evaluation was performed [22]. After completing the connection tests, tensile coupons were cut from the box and pin in the nominal pipe body and the connection zone as shown in Appendix C [18]. Two longitudinal and two transverse samples were cut every 90 degrees around the circumference of the box and pin at the indicated axial locations. Tensile tests were performed on these coupons at ambient and elevated temperatures. The minimum strength coupons were identified based on the yield stress corresponding to 0.65% strain offset for both the ambient and elevated temperature cases. The tensile test data of the minimum strength coupon was used to construct the material model for use in the finite element analysis.

### 4.4.1 Optimizing the Ramberg-Osgood Deformation Plasticity Model

A Ramberg-Osgood deformation plasticity material model was chosen to represent the stress-strain constitutive behavior [23]. This form was chosen because it allows both the elastic and plastic material behavior to be represented by a single smooth curve. The proper definition of a continuous transition between elastic and plastic behavior is necessary to appropriately

capture the plastic zones that develop throughout the connection analysis. The general 1D form of the deformation plasticity material model [21] is given by Equation (4.1)

$$\epsilon = \frac{\sigma}{E} + \frac{\sigma\alpha}{E} \left( \frac{|\sigma|}{\sigma^o} \right)^{n-1} \quad (4.1)$$

Where  $\epsilon$  is the total strain,  $\sigma$  is the stress,  $E$  is the Young's modulus,  $\alpha$  is the yield offset,  $n$  is the hardening exponent for the plastic term, and  $\sigma^o$  is the yield stress such that when  $\sigma = \sigma^o$ , Equation (4.2) is satisfied.

$$\epsilon = \frac{(1 + \alpha)\sigma^o}{E} \quad (4.2)$$

Stress and strain values were read from the tensile test data of the minimum strength coupon. In addition, initial estimates for the Young's Modulus  $E_0$  and the yield offset  $\sigma_0^o$  were determined from the data. Equation (4.2) was solved for  $\alpha_0$  as shown in Equation (4.3), and an initial estimate of unity was made for  $n_0$ .

$$\alpha_0 = \left( \frac{\epsilon_o * E_0}{\sigma_0^o} \right) - 1 \quad (4.3)$$

Where  $\epsilon_o$  is the measured strain corresponding to  $\sigma_0^o$ . In this way, an initial estimate of the deformation plasticity model was made. The initial estimate vector  $x_0 = \{\alpha_0, n_0, \sigma_0^o, E_0\}$  was constructed and passed to a nonlinear least squares optimization algorithm [24] as shown in the example code of Appendix D. The optimization algorithm began at the starting point  $x_0$  and used a search method to minimize the error in a least-squares sense between the deformation plasticity model given in Equation (4.1) and the extracted material test data. The fitted curve was plotted against the material test data and is shown below in Figure 4.8.

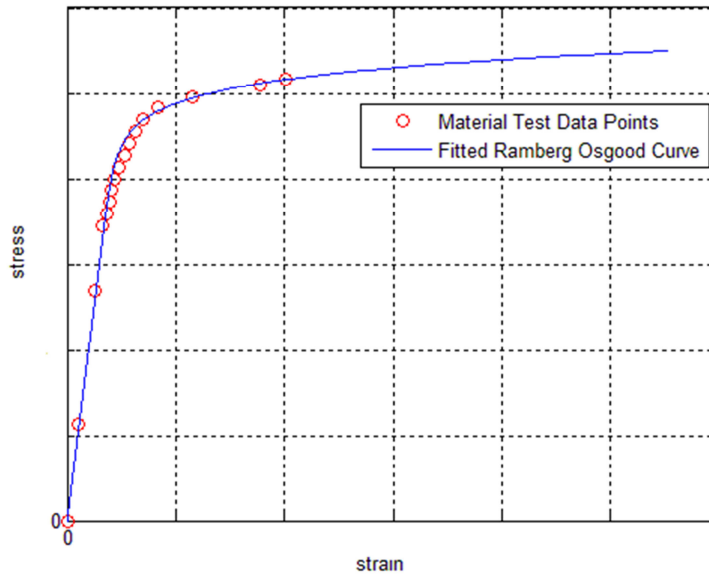


Figure 4.8: A fitted Ramberg-Osgood deformation plasticity material model

The optimized coefficients  $\alpha$ ,  $n$ ,  $\sigma_0$  and  $E$  were used to construct the Abaqus deformation plasticity model. In cases where the deformation plasticity formulation was prohibited (Abaqus/Explicit) a suitable table of stress and strain values was constructed from the Ramberg-Osgood fit and interpolated by Abaqus.

## 4.5 Meshing Schemes

Premium connections are some of the most difficult geometries to effectively mesh. It is for this reason that leading commercial meshing algorithms use premium connection geometries as test cases for development and benchmarking purposes. The axisymmetric profile of a premium connection will often have a geometric aspect ratio above 30. The seals are the main focus of the connection model, yet the entire seal region will never comprise more than 0.01% of the total meshed area. In the threaded region, there is a lack of regularity among the thread profiles, and rarely will two threads have the same dimensions. Rarely are two surfaces parallel to each other, and rarely do two edges meet at a right angle.

Because of this, the meshing scheme will make or easily break the connection model. Great care and effort must be devoted to the meshing scheme to achieve a stable mesh that can successfully converge a difficult contact solution in a reasonable amount of time. Several meshing techniques were investigated on the axisymmetric model and extended to the 3D case.

### 4.5.1 Axisymmetric Meshing

Partitioning is required to efficiently isolate regions of higher mesh resolution from regions of lower mesh resolution as shown in Figure 4.9. Often it is most efficient to use structured meshing in regions of high resolution, which comprise the immediate vicinity of the seals and shoulder. The second region to be isolated is the threaded region, with medium mesh density. The third region to be isolated is the area in the connection region behind the threads and the shoulder. These areas are given a medium to sparse mesh density and use a structured meshing technique. The final region to be isolated is the nominal pipe body which is assigned a sparse mesh density with longitudinal biasing toward the connection. The above regions are meshed, and then mesh transition regions between the sections are generated to bind these sections together using swept and free meshing techniques.

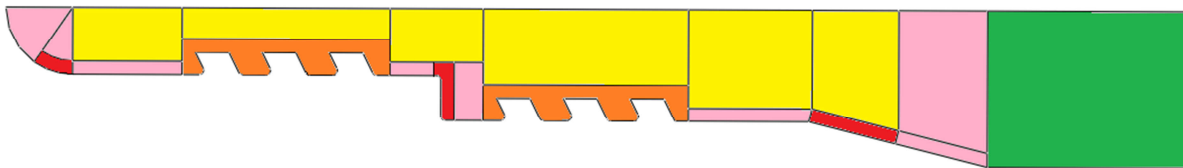


Figure 4.9: Partitioning scheme used for assignment of mesh parameters. High mesh density regions shown in red, medium density thread regions in orange, medium-sparse density shown in yellow, sparse density in green, and transition regions in pink.

The seal and shoulder areas are usually the starting point for any connection mesh because they have the greatest strain energy density and require the highest resolution to capture the steep stress gradients. The seal and shoulder surfaces are first lofted to provide parallel edges as a framework for the structured seal mesh. These surfaces should have several layers of elements with aspect ratios near 1. It is essential that the mesh maintains good aspect ratio in the

seal areas under load. To accomplish this, the elements can be tailored such that compression at the seal surfaces forces them into an ideal shape.

The thread regions are meshed second. The threads are not meshed at the high resolution of the seals to save computation time, but the thread mesh must be dense enough to adequately capture the thread geometry and effectively resolve the thread interference. The seals must be properly energized by resolving the thread and shoulder contact. Efficient structured thread meshing consisting of regularly shaped elements and good resolution at rounded edges can save a great deal of time when trying to resolve contact interference. Each thread should be partitioned into its own cell by extending lines from the thread root corners to the nominal ID or OD as shown in Figure 4.10. Further partitioning of the thread cell to isolate radii helps provide a more rectangular shape for efficient structured meshing in the thread interior.

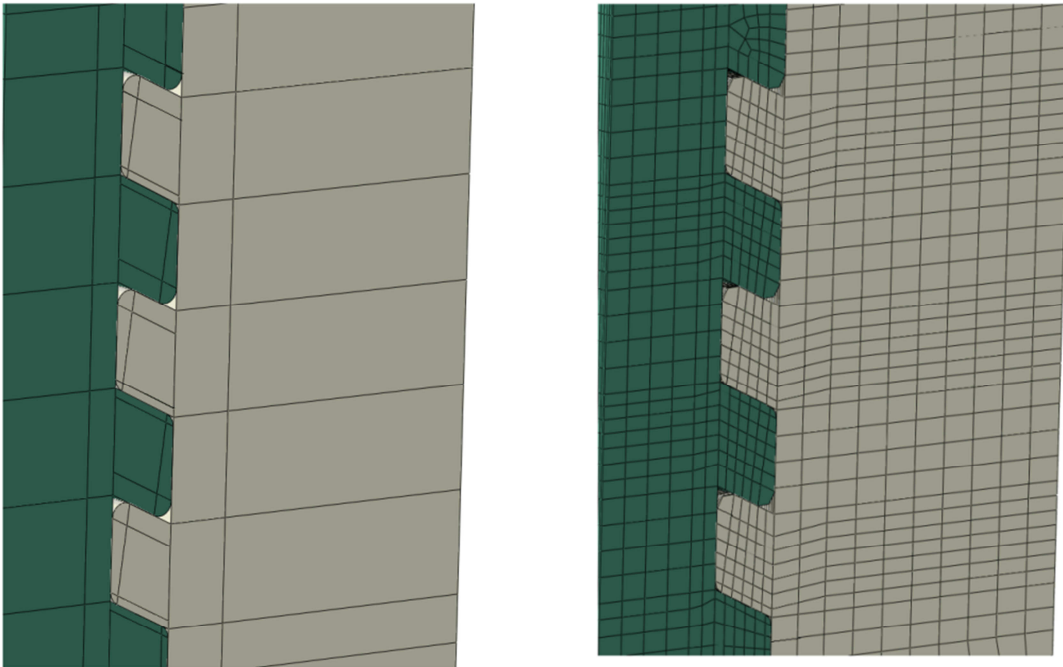


Figure 4.10: Thread partitioning (left) and meshing scheme (right).

All contact regions must be meshed with the interaction properties in mind. When selecting node densities, the elements on the slave contact surface should be kept smaller than those of the master surface. Best results were found with the pin contact surface treated as the slave and the box contact surface as the master. Slave elements were kept at roughly two thirds the size of the master elements. A guideline to element sizing with ballpark element distributions and compute times for axisymmetric models at various levels of refinement is given in Table 4.1.

Table 4.1: Seeding guidelines and element distributions for axisymmetric meshes at different levels of refinement

Assigned Node Density (mm)	Level 1	Level 2	Level 3	Level 4	Level 5
Pin Seal and Shoulder Regions	0.375	0.150	0.050	0.025	0.010
Pin Thread Regions	0.375	0.375	0.281	0.225	0.188
Box Seal and Shoulder Regions	0.500	0.200	0.100	0.050	0.020
Box Thread Regions	0.500	0.500	0.375	0.300	0.250
% of Total Elements in Region	Level 1	Level 2	Level 3	Level 4	Level 5
Pin	52	53	71	73	75
Box	48	47	29	27	25
Pin Seal and Shoulder	2	8	26	38	53
Box Seal and Shoulder	1	5	8	11	15
Pin Thread	30	24	11	5	2
Box Thread	28	23	9	4	1
Pin Transition	16	18	34	30	20
Box Transition	15	15	11	12	9
Pin Nominal Body	4	3	1	< 1	< 1
Box Nominal Body	5	4	1	1	< 1
Total CAX4 Elements in Model	6000	7500	20700	57600	244100
Total DOF	4.80E+04	6.00E+04	1.66E+05	4.61E+05	1.95E+06
Desktop PC Compute Time (min)	1	1	5	20	169

There is a constant battle between element count and aspect ratio. Best performance was identified for axisymmetric models with aspect ratio's less than 10 in the nominal pipe region, less than 5 in the connection region, less than 3 in the threaded regions, and less than 2 in the seal and shoulder region. All axisymmetric models were run with 4 node bilinear continuum axisymmetric elements (Abaqus CAX4 elements) using full integration. To improve compute time, reduced integration may be used selectively in the nominal sections and far from contact regions. Reduced integration should never be applied in contact sections or in the nose section where bending is the dominant mechanism.

#### 4.5.2 3D Meshing

With the shift from axisymmetric to 3D came a tremendous increase in the number of degrees of freedom and as a result, the mesh had to be efficiently tailored to permit fast model turnaround. 3D-wedge models consisting of a twenty-degree sweep of the connection geometry were used for both the box and pin. The meshing scheme in the radial-longitudinal (axisymmetric) plane was essentially unaltered.

Biasing was needed in the circumferential direction to keep element counts low. The priorities were to maintain good element quality at the cut-planes and at the wedge center line. The cut-planes required a low aspect ratio to aid the contact algorithm in resolving the edge

effects. The wedge centerline aspect ratio was kept low to provide optimum contact solutions and high quality elements for result extraction. In the seal region, aspect ratios were fixed at 1 as shown in Figure 4.11. A circumferential double bias was chosen as the best method to facilitate these needs. Radially, the biasing was toward the contact surfaces of the seals and threads and away from the connection OD and ID. Biasing was applied axially toward the connection zone in the nominal pipe body, but enough elements were kept in this nominal region to enforce the applied boundary conditions at the base of the part.

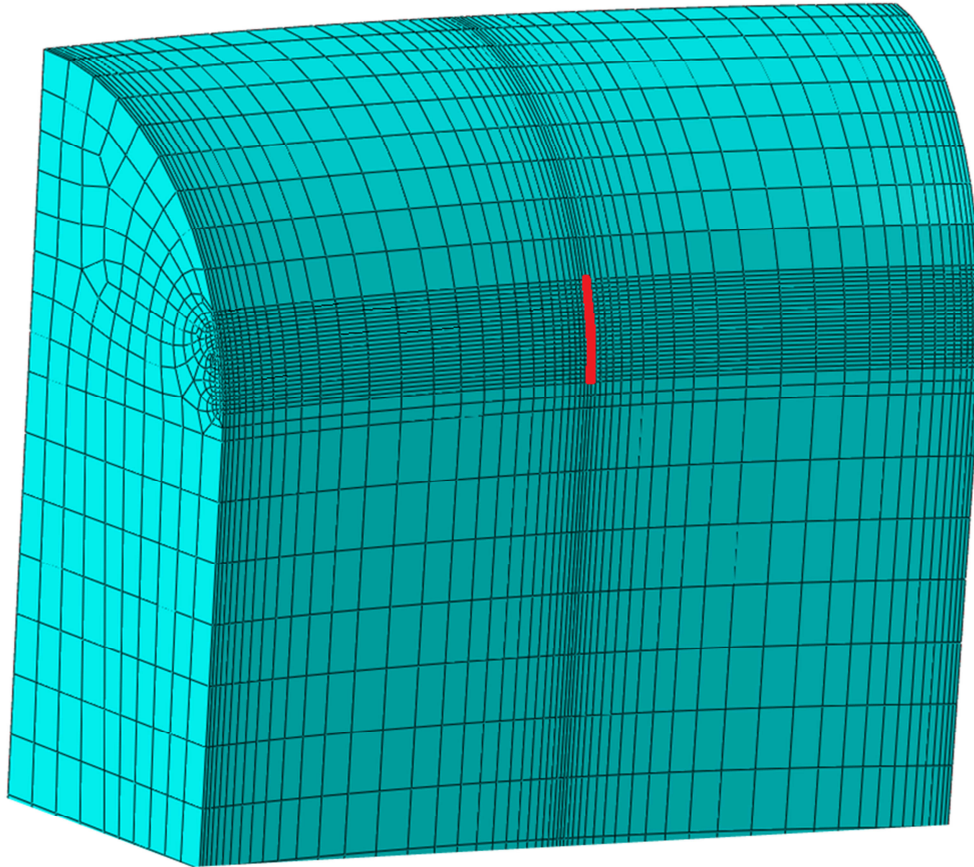


Figure 4.11: The circumferential double biasing scheme provides low aspect ratio at the wedge centerline and the edges. The aspect ratio of the elements on the wedge centerline at the seals is fixed at 1. Seal results are extracted from the area shown in red.

Mesh transition regions are much more expensive in 3D than in the axisymmetric models. To maintain efficiency, the transitions were tailored to produce changes in mesh density over a small volume while still maintaining acceptable aspect ratios. Considerable mesh savings were made by using a double transition in the area between the connection zone and the nominal region as illustrated in Figure 4.27. This transition was constructed by creating two axial partitions and using sweep meshing techniques. The first partition was seeded to provide a mesh reduction in the  $\theta - Z$  plane and then swept in the radial direction. The second partition was seeded to produce a reduction in the  $R - Z$  plane and swept in the circumferential direction. The

resulting mesh transition provided a very effective and concise reduction in mesh density between the dense seal regions and the sparse nominal section.

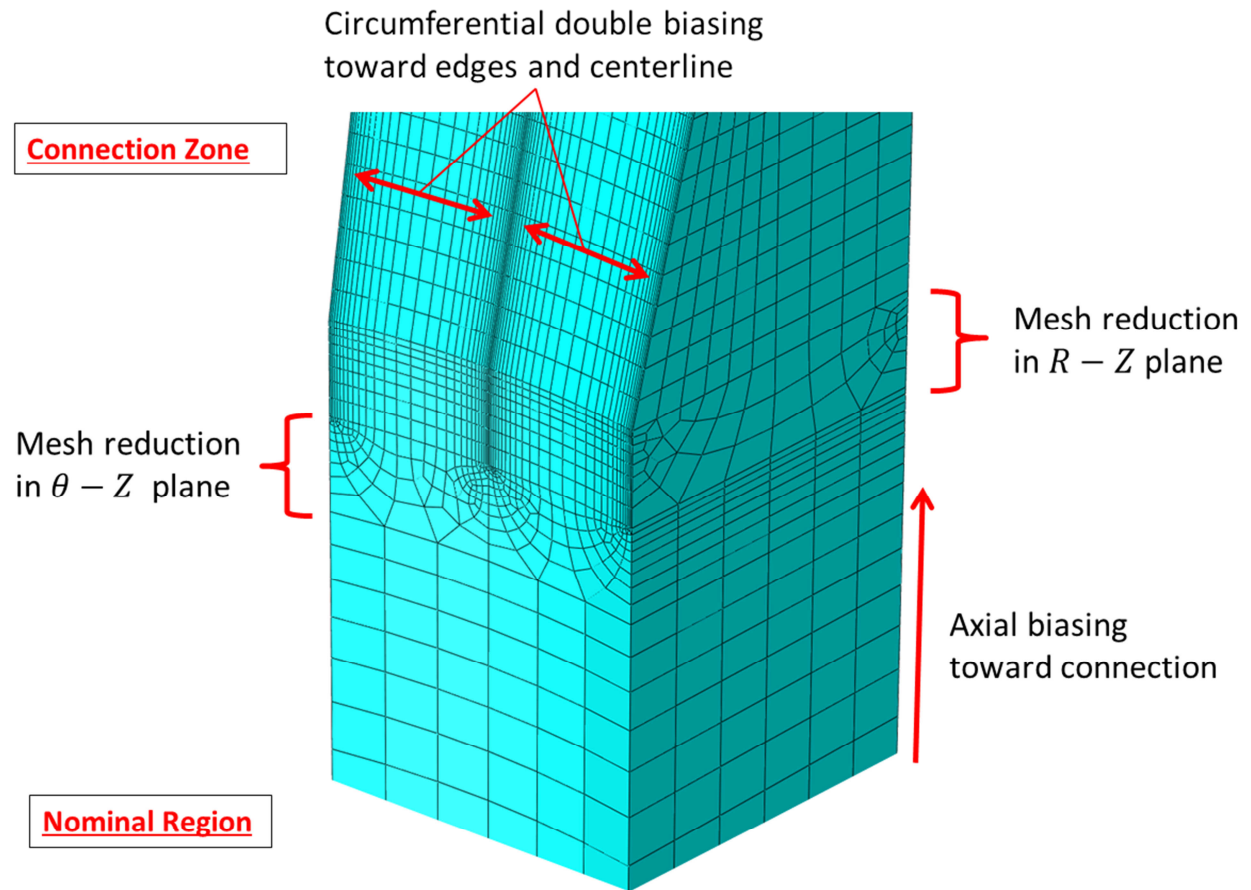


Figure 4.12: Meshing techniques used to achieve efficient mesh transitions.

The added degrees of freedom in the 3D models limit the ability to concentrate mesh refinement purely at the seals. This is apparent when comparing the percentage of elements allocated to the seal regions in both the axisymmetric and 3D models. As shown in Table 4.1 and

Table 4.2, at the highest levels of refinement the axisymmetric models allocate 68% of the total elements in the model to the critical shoulder and seal sections and 32% of the elements to capturing the “supporting” thread and transition regions. The 3D meshes can only allocate 21% of their elements to the critical sections, and must use 78% of the elements in the model to capture the threads and the mesh transitions. The reason for this is that mesh transitions are much more expensive in 3D. In addition the helix swept thread regions require additional mesh transition regions to maintain geometric continuity with the flat swept shoulder, nominal, and nose sections.

Table 4.2: Seeding guidelines and element distributions for 3D meshes at different levels of refinement

Assigned Node Density (mm)	Level 1	Level 2	Level 3
Pin Seal and Shoulder Regions	0.375	0.225	0.075
Pin Thread Regions	0.563	0.375	0.375
Box Seal and Shoulder Regions	0.500	0.300	0.100
Box Thread Regions	0.750	0.500	0.500
% of Total Elements in Region	Level 1	Level 2	Level 3
Pin	60	58	61
Box	40	42	39
Pin Seal and Shoulder	3	3	15
Box Seal and Shoulder	1	1	6
Pin Thread	35	33	22
Box Thread	25	25	15
Pin Transition	22	21	24
Box Transition	13	15	17
Pin Nominal Body	<1	<1	<1
Box Nominal Body	1	1	<1
Total Elements in Model (C3D8)	148400	225400	662400
Total Elements in Model (C3D8R)	42700	52800	169500
Total DOF	4.59E+06	6.68E+06	2.00E+07

Computation time was greatly increased in the 3D models because each element now had 24 degrees of freedom. To reduce computation time, reduced integration was used more generously than that in the axisymmetric models, but all contact regions used full integration. Level 1 meshes took 6-10 hours to complete on a desktop computer, and all other levels required the use of a compute server [25].

## 4.6 Resolving the Contact Problem

One of the greatest challenges in modeling premium connections is achieving an acceptable contact solution at the threads, seals, and shoulder. An acceptable contact solution is recognized by its ability to eliminate regions of overclosure in the geometry. In the physical connection make-up the interference in the threads is built up gradually between the hand-tight configuration and the shoulder-tight configuration as the pin is rotated into the box. This can be seen by the gradual and fairly linear torque buildup in the torque-turn plot as shown in Figure 4.13.

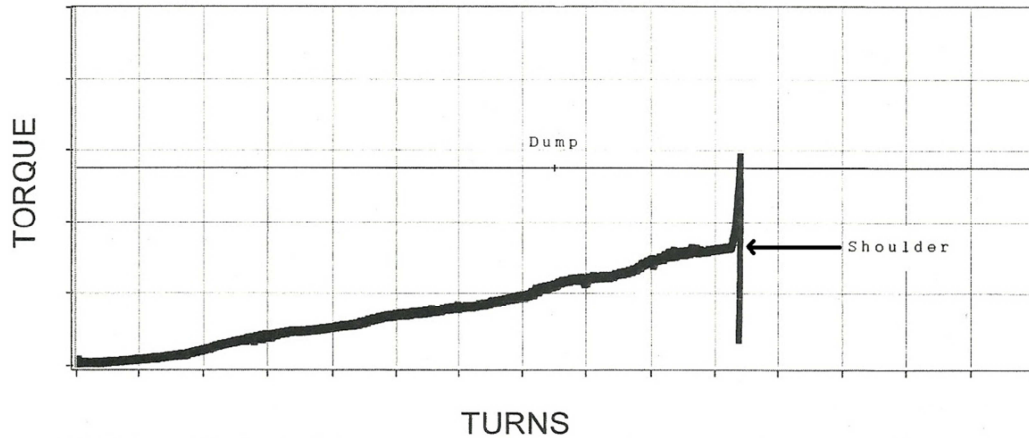


Figure 4.13: Sample torque-turn plot from experimental connection make-up illustrating the shoulder point and final torque dump. Used with permission of Hess Corporation [18].

This large deformation process is extremely expensive to capture with standard finite element formulations. It is more efficient to skip this gradual interference buildup and achieve a shoulder tight configuration by instantiating the box and pin directly in their shoulder tight locations. The tradeoff is that a highly nonlinear contact constraint must now be enforced. No single contact resolution method will satisfy every modeling case, and several complimenting methods have been developed for varying levels of contact severity.

There are three conceptual means to accomplish the contact constraint enforcement:

- 1) The transient dynamic effects of an impulse contact resolution can be ignored and the interference can be resolved by gradually enforcing the constraint in pseudo-time using many small increments. This is referred to as the standard interference fit formulation.
- 2) A thermal expansion process can be applied to the system to treat the event like a shrink fit problem. Once the overclosures have been eliminated by the mechanism of thermal expansion the contact property can be instantiated and the thermal gradient gradually removed to build up the contact pressures. This is referred to as the method of thermal expansion.
- 3) The transient dynamic effects of an impulse contact resolution can be taken into account. The kinetic energy of the impulse event can be dissipated by the model through the parallel mechanisms of the inertial effects and strain energy. Damping can then be applied to eliminate the inertial effects, and the resulting steady state solution remains with strain energy as the only remaining form. This is referred to as the explicit finite element contact formulation.

#### **4.6.1 Standard Interference Fit**

Often the fastest and most straightforward method of contact resolution is to initialize the model in the shoulder-tight configuration and specify the contact to be solved as a standard interference fit. This approach works well for most applications, but will have difficulty with high density seal meshes where the overclosures to be resolved are greater than several element thicknesses. In this case, the contact manager will force the volume of the slave elements in the immediate contact region to zero in an effort to satisfy the penetration requirements. This action

forces the Jacobian of those elements to zero which prohibits the stiffness matrix from being inverted, causing the model to fail. If this is the case, the method of thermal expansion should be used to resolve the make-up interference fit as shown in Section 4.6.2. Both contact resolution methods will produce consistent seal results.

#### 4.6.1.1 Contact Discretization and Tracking

When setting the contact properties for a standard interference fit, a surface to surface contact discretization is the best practice because it provides a built-in smoothing operation where slave penetrations are averaged over surface regions rather than at nodal points of singularity. Finite sliding formulations should be used because the large deformation in the contact areas means that the surface normals will need to be recomputed as the incremental solution progresses. Surface smoothing was applied in the 3D models to aid the representation of curved contact surfaces using linear element faces.

When selecting contact pairs and master/slave designations, the master surface in the contact definition should always be the stiffer member. The master surface consisted of the entire box contact surface, and the slave surface consisted of the entire pin contact surface as shown in Figure 4.14. Alternative combinations of master and slave surfaces could be used, such as splitting up the contact zone and using several contact definitions across the connection length, but the above configuration functioned well because only a single set of contact constraints was required.



Figure 4.14: Master box contact surface shown in red. Slave pin contact surface shown in pink.

#### 4.6.1.2 Contact Constraint Enforcement

The initial overclosures in the models were treated as interference fits. The slave node overclosures were gradually removed throughout the step duration by specifying a uniform allowable interference with a normalized smooth step amplitude curve. The generalized form of this cubic function is found in Equation (4.4) [21].

$$A(t) = A_i + (A_{i+1} - A_i)z^3(10 - 15z - 6z^2)$$

$$z = \left( \frac{t - t_i}{t_{i+1} - t_i} \right) \quad (4.4)$$

Where  $A(t)$  is the amplitude of the maximum allowable slave node penetration as a function of step time  $t$ ,  $A_i = 1$  is the initial normalized amplitude,  $A_{i+1} = 0$  is the final amplitude,  $t_i = 0$  is the initial step time, and  $t_{i+1} = 1$  is the final step time. This amplitude curve has the same form as a cam curve and was used because it provides a smooth application of the constraint with zero velocity and zero acceleration at the beginning and end of the time step as shown in Figure 4.15. By smoothing out the step application of the constraint the contact problem becomes tractable.

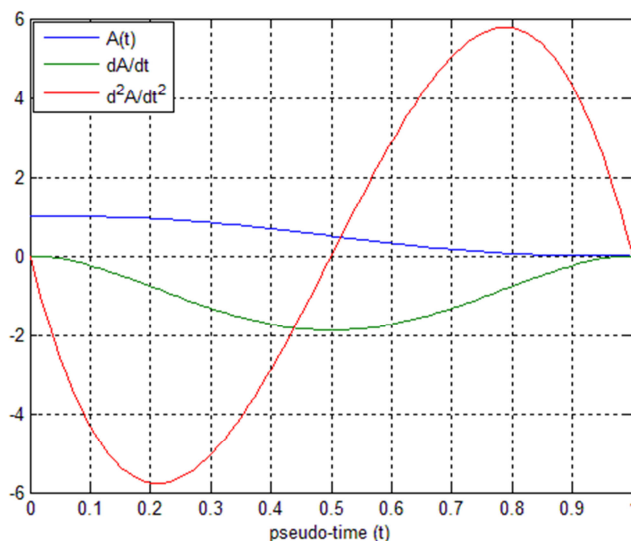


Figure 4.15: The smooth step amplitude curve used to apply the maximum allowable interference constraint in the contact formulation. First and second time derivatives also shown.

A penalty constraint enforcement method was specified in both the tangent and normal directions. The penalty method is an approximation of hard contact that replaces the step function boundary application with a stiff approximation. The penalty stiffness is calculated based on the underlying stiffness of the contact surfaces but a scaling factor can be applied to tune the penalty formulation for the application. A high penalty stiffness can result in a smaller stable time increment and a longer solve time. A small penalty stiffness can result in excessive penetrations at the end of the step. Best results were achieved using a penalty stiffness between 100 and 1000 based on the mesh density and interference magnitudes.

A penalty enforcement method was also applied to the tangential friction in the 3D models. There is no need to specify friction coefficients in axisymmetric connection models because the primary degree of freedom that the friction acts along is disabled. This is not the case in the 3D models. In 3D connection models, the assumed friction coefficient between the two bodies is linearly proportional to the torque that the model can achieve. Accurate torque-theta measurements in the lab can provide valuable data for tuning the appropriate 3D connection model friction coefficient(s). Appropriate friction coefficients were found in the range between 0.08 and 0.12. These friction coefficient values are in the same ballpark as those assumed for modeling and testing purposes in the industry today.

#### 4.6.2 Method of Thermal Expansion

At higher levels of mesh refinement, the interference can be so severe that elements in the contact region collapse to zero volume. To resolve this issue an additional measure was taken to aid the contact resolution.

The thermal expansion make-up simulation occurs in four steps. The pin and box are instantiated at a reference temperature of zero in the shoulder-tight configuration with no contact property defined. With the axial displacement fixed at the shoulder, a negative temperature is applied to the pin volume and it undergoes volumetric contraction until the radial interference between pin and box is eliminated. The standard contact definition as outlined in Section 4.6.1 is initiated in this interference-free state. The pin is then returned to its original temperature,

gradually building contact pressure in the thread, shoulder, and seal interference regions as it expands back to its original location.

In this process, the threads cannot simply translate radially because the thread load flanks make an angle with the radial-longitudinal plane as shown in Figure 4.16. To effectively shrink the pin in the radial direction, there must be a simultaneous axial translation in the threaded region. This issue is addressed by applying orthotropic thermal expansion coefficients in the threaded areas of the pin. Additionally, pretension sections can be used in the cool and warm steps to help prevent axial thread interference as the threads contract radially. These “thread location pretensions” must be zeroed out at the end of the warm step so the geometry is not skewed in any subsequent analysis steps.

The expansion coefficients must be applied with the fixed axial displacement boundary condition at the pin shoulder in mind. The threads above the shoulder require both radial and axial expansion with a positive temperature change, thus the signs of both the axial and transverse expansion coefficients should be positive. The threads below the shoulder boundary condition require radial contraction and axial expansion to maintain the kinematic thread requirements with a positive change in temperature; therefore the transverse expansion coefficients must be negative.

#### 4.6.2.1 Calculation of Orthotropic Thermal Expansion Properties

The expansion coefficients are calculated by first establishing a right-hand cylindrical coordinate system to define the intended thread translation vector  $\vec{V}$  and thread translation angle  $\beta$  measured counterclockwise from the positive  $Z$  axis in the  $Z$ - $R$  plane as shown in Figure 4.16. This coordinate system is also used to define the orthotropic material orientation.

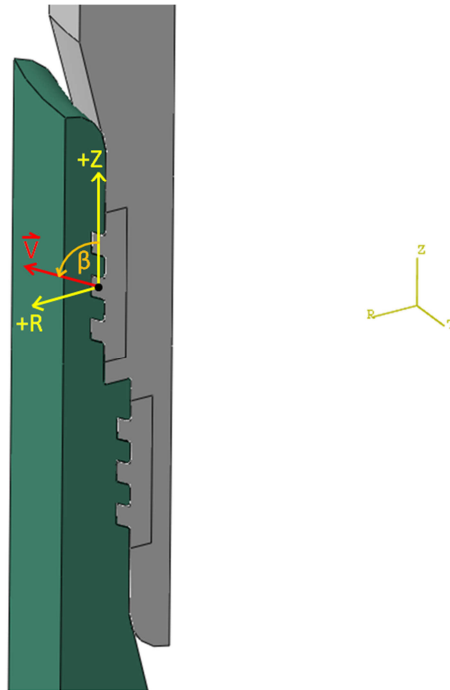


Figure 4.16: The coordinate system defined for the orthotropic expansion coefficients with desired thread translation vector  $\vec{V}$  and angle  $\beta$  corresponding to a positive temperature change. The box is displayed in green, and the pin in grey.

In order to have the pin threads translate in the proper direction  $\vec{V}$  with a positive temperature change, the strains in the radial direction  $\epsilon_{11}$  and in the axial direction  $\epsilon_{33}$  must be governed by Equation (4.5).

$$\tan(\beta) = \frac{\epsilon_{11}}{\epsilon_{33}} \quad (4.5)$$

It has also been found that enforcing a transverse isotropic expansion requirement produces the best results. This requires the transverse expansion coefficients in the radial  $\alpha_{11}$  and circumferential  $\alpha_{22}$  directions to be equivalent. The strains of a three dimensional thermal expansion problem are related by the relationships found in Equation (4.6)

$$\begin{aligned} \epsilon_{11} &= \alpha_{11}(\Delta T) - \nu(\epsilon_{22} + \epsilon_{33}) \\ \epsilon_{22} &= \alpha_{22}(\Delta T) - \nu(\epsilon_{11} + \epsilon_{33}) \\ \epsilon_{33} &= \alpha_{33}(\Delta T) - \nu(\epsilon_{11} + \epsilon_{22}) \end{aligned} \quad (4.6)$$

Substituting Equation (4.5) into Equation (4.6), enforcing the isotropic expansion requirement, and rearranging terms produce the following system that can be solved to find the transverse expansion coefficients.

$$\begin{Bmatrix} \epsilon_{11} \\ \epsilon_{22} \\ \alpha_{11} = \alpha_{22} \end{Bmatrix} = \begin{bmatrix} 1 + \nu \cot(\beta) & \nu & 0 \\ \nu + \nu \cot(\beta) & 1 & -\Delta T \\ \nu + \cot(\beta) & \nu & -\Delta T \end{bmatrix}^{-1} \begin{Bmatrix} \alpha_{11}(\Delta T) \\ 0 \\ 0 \end{Bmatrix} \quad (4.7)$$

### 4.6.3 Explicit Finite Element Contact Formulation

An alternative method to tackle the contact problem is to use an explicit finite element formulation. This formulation is inherently more stable because inertial effects work in parallel with the mechanism of strain energy to help dissipate energy as a result of the sudden ‘‘impact’’ of the contact constraint enforcement.

#### 4.6.3.1 Implicit solutions with Newton-Raphson Iterations

In the standard (implicit) formulation, the entire structure is forced into equilibrium with the externally applied loads at the end of each load increment. For nonlinear elasticity problems in which the stiffness of the structure is a function of the displacement field, several iterations must take place to reach the incrementally applied load. These problems were solved using Newton-Raphson iterations by first assuming an initial tangent stiffness  $[K_{t0}]$  to solve for the initial displacement estimate  $\{u_a\}$  under a small increment  $\{F_1\}$  of the total load  $\{F\}$  as shown in Equation (4.8) [26].

$$\{u_a\} = [K_{t0}]^{-1}\{F_1\} \quad (4.8)$$

The force error  $\{e_a\}$  for the initial displacement estimate  $\{u_a\}$  is then evaluated by Equation (4.9) where  $[K_{ta}]$  is the tangent stiffness evaluated using the displacement vector  $\{u_a\}$ .

$$\{e_a\} = \{F_1\} - [K_{ta}]\{u_a\} \quad (4.9)$$

Equilibrium iterations are executed to minimize this force error by beginning at  $\{u_a\}$  and using  $[K_{ta}]$  to solve for the next displacement estimate  $\{u_b\}$  as shown in Equation (4.10).

$$\{u_b\} = [K_{ta}]^{-1}\{F_1\} \quad (4.10)$$

$\{u_b\}$  is then used to calculate  $[K_{tb}]$  and the force error  $\{e_b\}$  is evaluated using Equation (4.11).

$$\{e_b\} = \{F_1\} - [K_{tb}]\{u_b\} \quad (4.11)$$

The process continues until the force error  $\{e_i\}$  is sufficiently minimized and the displacement vector  $\{u_i\}$  approaches the correct value  $\{u_1\}$  which is equivalent to the product of  $[K_{t1}]^{-1}$  and  $\{F_1\}$ . The load increment  $\{F_i\}$  is then increased by the contact algorithm until all slave node penetrations are eliminated.

This solver has the advantage of being unconditionally stable which allows for fewer increments in nonlinear problems, but the drawback of using Newton-Raphson iterations is that the stiffness matrix  $[K_{ti}]$  must be assembled and inverted every time the displacement vector  $\{u_i\}$  is updated. This is an extremely memory intensive operation that tends to be limited by the data transfer capabilities of the computer. Implicit alternatives to the Newton-Raphson method exist but the quadratic convergence rate of this method was found to be superior in terms of solution time for this problem.

#### 4.6.3.2 Explicit Solutions of Nonlinear Elasticity

The explicit formulation does not enforce this static equilibrium at the end of each increment; rather the contact constraint enforcement is modeled in the same manner as a wave propagation problem using Equation (4.12).

$$[K]\{u\} + [M]\{\ddot{u}\} = \{F\} \quad (4.12)$$

Where  $[M]$  is the global assembled mass matrix,  $\{\ddot{u}\}$  is the vector of nodal accelerations, and  $\{F\}$  is the vector of loads which may now vary in time. The most powerful advantage of the explicit finite element formulation in solving nonlinear elasticity problems is that the stiffness matrix no longer needs to be inverted. Instead, the internal forces of the system  $F_{int} = [K]\{u\}$  can be calculated in element-by-element fashion by Equation (4.13) [26].

$$\{F_{int}\} = \sum_{i=1}^{N_{el}} (\{f_{int}\}_n) \quad (4.13)$$

Where the elemental internal forces  $\{f_{int}\}_n$  are calculated using the strain-displacement matrix  $[B]$  and the elemental stress vector  $\{\sigma\}_n$  by Equation (4.14)

$$\{f_{int}\}_n = \int [B]^T \{\sigma\}_n dV \quad (4.14)$$

By removing the formation and storage of  $[K]$ , the problem is freed from the limiting data transfer capabilities of the computer and is now limited only by the processor speed.

Explicit contact solutions were found to be faster on extremely large models (over 1 million elements) because of their ability to scale well on large compute servers. This method of resolving the contact problem is likely the best way forward if a full 360-degree model were to be attempted.

The disadvantage to the explicit method is that it is conditionally stable. The time increment  $\Delta t$  is limited by the natural frequency of the smallest element in the mesh as shown in Equation (4.15) [26].

$$\Delta t \leq \frac{2}{\omega_{\max}} \quad (4.15)$$

Where  $\omega_{\max}$  corresponds to the highest natural frequency of the undamped system in Equation (4.16)

$$([K] - \omega^2[M])\{u\} = \{0\} \quad (4.16)$$

This requirement presents a challenge when trying to use a high resolution mesh in the seal region. The result is often an extremely small stable time increment and many time steps to reach a solution. The ratio of the kinetic energy to the total energy of the model must be monitored and brought to less than 1% at the end of the step. The kinetic energy can be reduced by using smooth step amplitude curves to apply loads, contact constraint enforcements, and boundary conditions as shown in Section 4.6.1.2. Damping can also be added to the system to reduce kinetic energy levels.

## 4.7 Loading Schemes and Boundary Conditions

Once the initial contact resolution has completed and the connection is shouldered, torque must be applied to the system to generate the final make-up state. Several methods of applying loads and boundary conditions were investigated to find the most representative make-up configuration in an acceptable amount of time.

### 4.7.1 3D Loading Methods

#### 4.7.1.1 Decomposition of the Connection Make-up

The full 360-degree finite element model is almost intractable due to the geometric complexity of premium connections and the high mesh resolution required to achieve a meaningful seal result. To achieve a 3D model yet keep runtimes low the 3D-wedge model was developed. For the wedge model to represent the full 360-degree system, the unmodeled portion of the connection must be sufficiently represented using loads and boundary conditions. To find the proper set of loads and boundary conditions the make-up problem was broken down into its dominant features.

The connection make-up can be thought of in terms of a superposition of the composite cylinders problem and the torsion bar problem. Such problems seem trivial, but isolate subtle details that contribute to the proper modeling technique of the 3D-wedge.

#### 4.7.1.2 The Composite Cylinders Problem

In its simplest form, the radial metal-metal seal of an OCTG connection can be viewed as a composite cylinder made up of an inner and outer member. If we consider only a section far from the ends so that edge effects can be neglected, and maintain linear elastic isotropic material behavior, it is possible to construct some basic relations from the equations of equilibrium and the compatibility conditions. We shall assume that the deformations of the cylinder are axisymmetric, that the cylinder is open ended (i.e. no end caps), and that the deformations are independent of the axial coordinate  $z$ . Only axisymmetric loads and constraints will be permitted, and thus our solution will be purely a function of the radial coordinate  $r$ . The circumferential coordinate shall be referred to as  $\theta$ . The cylindrical deformations  $u, v, w$  will correspond to the directions  $r, \theta, z$  respectively. If we neglect all body force components, the equations of equilibrium become [27]

$$r \frac{d\sigma_{rr}}{dr} = \sigma_{\theta\theta} - \sigma_{rr} \quad (4.17)$$

Which when rearranged shows

$$\sigma_{\theta\theta} = \frac{d}{dr} (r \sigma_{rr}) \quad (4.18)$$

Thus the strain components become

$$\epsilon_{rr} = \frac{\partial u}{\partial r}, \quad \epsilon_{\theta\theta} = \frac{u}{r} + \frac{1}{r} \frac{\partial v}{\partial \theta}, \quad \epsilon_{zz} = \frac{\partial w}{\partial z} \quad (4.19)$$

The shear components  $\gamma_{r\theta}, \gamma_{rz},$  and  $\gamma_{\theta z}$  become zero due to the radial symmetry. By these equations we can see that

$$r \frac{d\epsilon_{\theta\theta}}{dr} = \epsilon_{rr} - \epsilon_{\theta\theta} \quad (4.20)$$

Which when rearranged yields the strain compatibility equation for the thick walled cylinder.

$$\epsilon_{rr} = \frac{d}{dr} (r \epsilon_{\theta\theta}) \quad (4.21)$$

For a cylinder of inner radius  $a$  and outer radius  $b$  subject to inner pressure  $p_i$  and outer pressure  $p_o$  in the absence of temperature changes, the radial displacement as a function of  $r$  is

$$u = \frac{r}{E(b^2 - a^2)} \left[ (1 - \nu)(p_i a^2 - p_o b^2) + \frac{(1 + \nu)a^2 b^2}{r^2} (p_i - p_o) \right] \quad (4.22)$$

If the cylinder exists in the absence of an axial force and at constant temperature the stress relationships are

$$\begin{aligned}
\sigma_{rr} &= \frac{p_i a^2 - p_o b^2}{b^2 - a^2} - \frac{a^2 b^2}{r^2 (b^2 - a^2)} (p_i - p_o) \\
\sigma_{\theta\theta} &= \frac{p_i a^2 - p_o b^2}{b^2 - a^2} + \frac{a^2 b^2}{r^2 (b^2 - a^2)} (p_i - p_o) \\
\sigma_{rr} + \sigma_{\theta\theta} &= \frac{2(p_i a^2 - p_o b^2)}{b^2 - a^2} = \text{constant} \\
\sigma_{zz} = \tau_{r\theta} = \tau_{rz} = \tau_{\theta z} &= 0
\end{aligned} \tag{4.23}$$

At this point we shall assume a linear elastic isotropic material condition. The stress-strain relations for a linearly elastic isotropic material are

$$\begin{aligned}
\epsilon_{rr} &= \frac{1}{E} [\sigma_{rr} - \nu(\sigma_{\theta\theta} + \sigma_{zz})] \\
\epsilon_{\theta\theta} &= \frac{1}{E} [\sigma_{\theta\theta} - \nu(\sigma_{rr} + \sigma_{zz})] \\
\epsilon_{zz} &= \frac{1}{E} [\sigma_{zz} - \nu(\sigma_{rr} + \sigma_{\theta\theta})] = \text{constant} \\
\gamma_{r\theta} = \gamma_{rz} = \gamma_{\theta z} &= 0
\end{aligned} \tag{4.24}$$

As an example, let a composite cylinder be made up of two members as shown in Figure 4.17. The inner member (the pin) has an inner radius of  $a = 108$  mm and an outer radius of  $c_i = 118$  mm. The outer member (the box) has an inner radius of  $c_o = 117.5$  mm and an outer radius of  $b = 125$  mm. After make-up, the interface shown at point  $c$  reaches equilibrium.

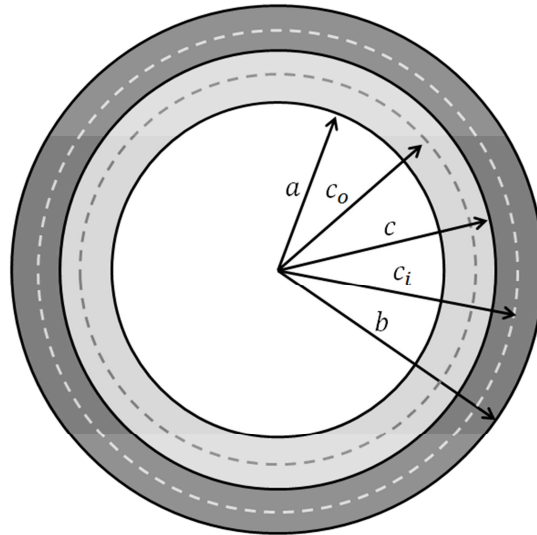


Figure 4.17: The composite cylinder example problem.

The displacement at the interface for the pin uses  $p_i = 0, p_o = p_s, r = c_i, a = a, b = c_i$  in Equation (4.22).

$$u_{pin} = \frac{c_i}{E(c_i^2 - a^2)} [(1 - \nu)(-p_s c_i^2) + (1 + \nu)a^2(-p_s)] \quad (4.25)$$

The displacement at the interface for the box uses:  $p_i = p_s, p_o = 0, r = c_o, a = c_o, b = b$

$$u_{box} = \frac{c_o}{E(b^2 - c_o^2)} [(1 - \nu)(p_s c_o^2) + (1 + \nu)b^2(p_s)] \quad (4.26)$$

Where  $p_s$  is the pressure between the two cylinders at their interface. We know that the sum of the deflections at the interface must be the difference between  $c_i$  and  $c_o$ .

$$c_i - c_o = u_{box} - u_{pin}$$

$$0.5 = \left\{ \frac{c_i}{E(c_i^2 - a^2)} [(1 - \nu)(-p_s c_i^2) + (1 + \nu)a^2(-p_s)] \right\} - \left\{ \frac{c_o}{E(b^2 - c_o^2)} [(1 - \nu)(p_s c_o^2) + (1 + \nu)b^2(p_s)] \right\} \quad (4.27)$$

This equation can be solved to find the interfacial pressure  $p_s = 30.9 \text{ MPa}$ . The deflection can be calculated at the interface based on this interfacial pressure.

$$u_{pin} = -0.201 \text{ mm}$$

$$u_{box} = 0.299 \text{ mm}$$

Here the negative sign on  $u_{pin}$  shows the deflection is towards the center of the radius. The interface between the two cylinders can be calculated as  $c = c_o + u_{box} = 117.80 \text{ mm}$ . The resulting stresses and strains at various locations can now be computed by the relations given above. For the pin we use the following values in the displacement equation:  $p_i = 0, p_o = p_s, a = a, b = c_i$ . For the box the following values are used:  $p_i = p_s, p_o = 0, a = c_o, b = b$ . The principal stresses and strains are plotted in Figure 4.18 as a function of the composite cylinder wall thickness.

#### 4.7.1.3 The Composite Cylinder Finite Element Model

This solution can also be achieved by the Finite Element Method. Consistent with the plane stress assumption of the formulation in Section 4.7.1.2, a 2D plane stress finite element model was constructed for the case of the full 360-degree composite cylinders problem. Stress results were extracted through the connection thickness. There is a slight variation between the hand solution and the finite element solution at the inner and outer diameters in the radial stress result due to the challenge of representing a free boundary condition. Despite these differences the radial stress results can be shown to agree to within 1.9% of the hand solution and the tangential stress results agree with the hand solution to within 0.7% as shown in Figure 4.18.

By assuming the full 360-degree composite cylinders problem can be modeled using only a sector, an acceptable finite element result can be achieved while significantly reducing the number of degrees of freedom. A twenty-degree sector was used to model the plane stress composite cylinder problem. The best way to approximate the effect of the removed 340-degree section in the composite cylinders problem is to apply symmetry boundary conditions to the cut-

planes in the tangential direction. These boundary conditions produce stress results that agree with the hand solution to within 2.3% in the radial direction and to within 0.7% in the tangential direction as shown in Figure 4.18.

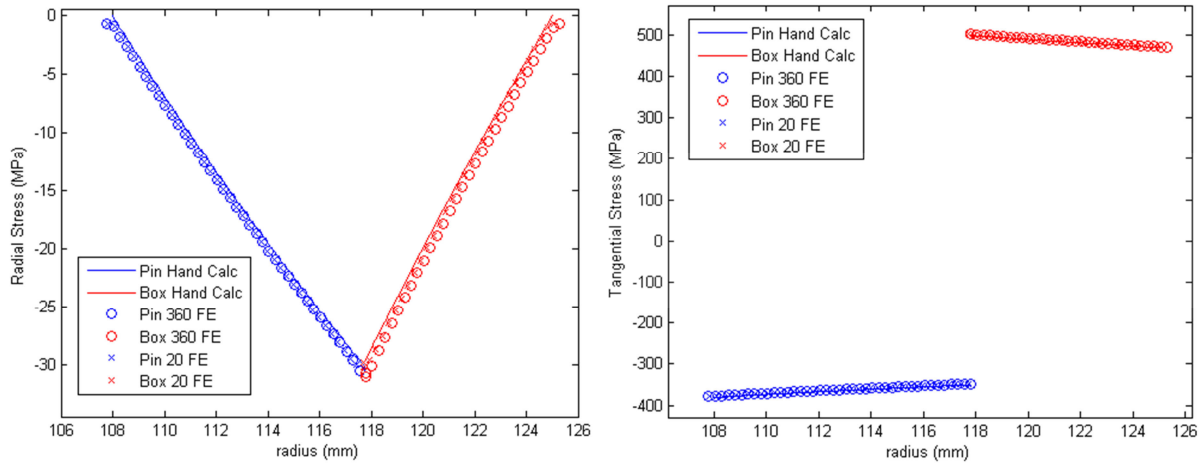


Figure 4.18: An overlay of three solutions for the composite cylinders problem.

Modeling features used in the 360-degree and wedge models are provided in Table 4.3. It should also be noted that the twenty-degree wedge model produces the same result as the 360-degree model with 1/18<sup>th</sup> of the required elements.

Table 4.3: Features for the composite cylinders finite element models

Model Feature	Plain Strain 360 Degree Composite Cylinders	Plain Strain 20 Degree Wedge Composite Cylinders
Boundary Conditions (In cylindrical coordinate system)	Single node at base of box OD: $U_1 = U_2 = U_3 = 0$	Edges of box cut-planes: $U_2 = 0$ Edges of pin cut-planes: $U_2 = 0$
Contact Property	Type: Surface to Surface Constraint Enforcemet: Penalty	Type: Surface to Surface Constraint Enforcemet: Penalty
Element Type	CPS4, a 4-node bilinear plane stress element	CPS4, a 4-node bilinear plane stress element
Number of Elements	212040	11780

#### 4.7.1.4 The Torsion Bar Problem

The second step in a make-up analysis is taking a connection in the shoulder-tight configuration and applying a torque  $T$ . This process can be idealized as a cantilevered cylindrical member under a torsion load. This idealization in the finite element model removes expensive thread features from the problem and allows for quick turnaround and boundary condition experimentation. It also allows the model to be calibrated by reference to a hand calculation.

The hollow cylinder from the composite cylinders problem is 300 mm long with an inner radius of 108 mm and an outer radius of 125 mm is subject to a torsion load of 40,000 N\*m. The circumferential displacement  $v$  of the cylinder is given by Equation (4.28).

$$v = \frac{Tl}{GJ} \quad (4.28)$$

$$J = \frac{\pi}{2}(b^4 - a^4) \quad (4.29)$$

Where  $J$  is the polar moment of inertia as shown in Equation (4.29) and  $G$  is the shear modulus. The stresses in the torsion bar are zero except for the in-plane shear component which can be calculated by Equation (4.30).

$$\tau_{rz} = \frac{TC}{J} \quad (4.30)$$

Where  $C$  is the radius measured from the middle of the cylinder.

#### 4.7.1.5 The Torsion Bar Finite Element Model

An identical solution to the torsion bar problem can be found using a full 360-degree 3D finite element model. As presented in Table 4.4, the bottom surface of the pipe was fixed in all directions and torque was applied at a reference point on the axis of symmetry which was kinematically constrained to the pipe top surface. The displacement results measured along the longitudinal axis of the 360-degree model agree with the hand solution to within 1%. The shear stress results for these two formulations also agree to within 1% as shown in Figure 4.20.

An equally acceptable solution can be found with far less computational effort by using the 20-degree wedge. The best method of loading the wedge for the torsion problem is to use displacement controlled loading to and measure the torque reaction at the base as illustrated in Figure 4.19. These boundary conditions are also given in Table 4.4 and Table 4.5. The method of prescribing displacements is simpler to apply and more stable than loading the model by application of surface tractions. The bottom surface was kinematically constrained to a reference point on the axis and held fixed in all directions. Antisymmetry boundary conditions are the best choice for the cut-planes in the torsion bar problem. This means that the cut-planes are restricted in the longitudinal and radial directions but are free to move tangentially. It is the complete reciprocal of the cut-plane boundary conditions applied in the composite cylinders problem.

Table 4.4: Features for the torsion bar finite element models

Model Feature	360 Degree Torsion Bar	20 Degree Wedge Torsion Bar
Loads / Boundary Conditions (In cylindrical coordinate system)	Base surface: BC on reference point $U1 = U2 = U3 = 0$	Base surface: BC on reference point $U1 = U2 = U3 = 0$
	Top surface: Torque at reference point: 40,000 N*m	Cut-plane surfaces: $U1 = U3 = 0$ Top edges: U2 Prescribed Displacement See Table 4.5
Contact Property	Type : Surface to Surface Constraint Enforcemet: Penalty	Type : Surface to Surface Constraint Enforcemet: Penalty
Element Type	C3D8, an 8-node linear brick element	C3D8, an 8-node linear brick element
Number of Elements	37440	2080

Table 4.5: Tangential boundary conditions at the top surface for the torsion bar wedge problem.

Boundary Condition	Radius (mm)	U2 Prescribed Displacement
Inner Radius	108	0.0993
Middle Radius	116	0.1071
Outer Radius	125	0.1149

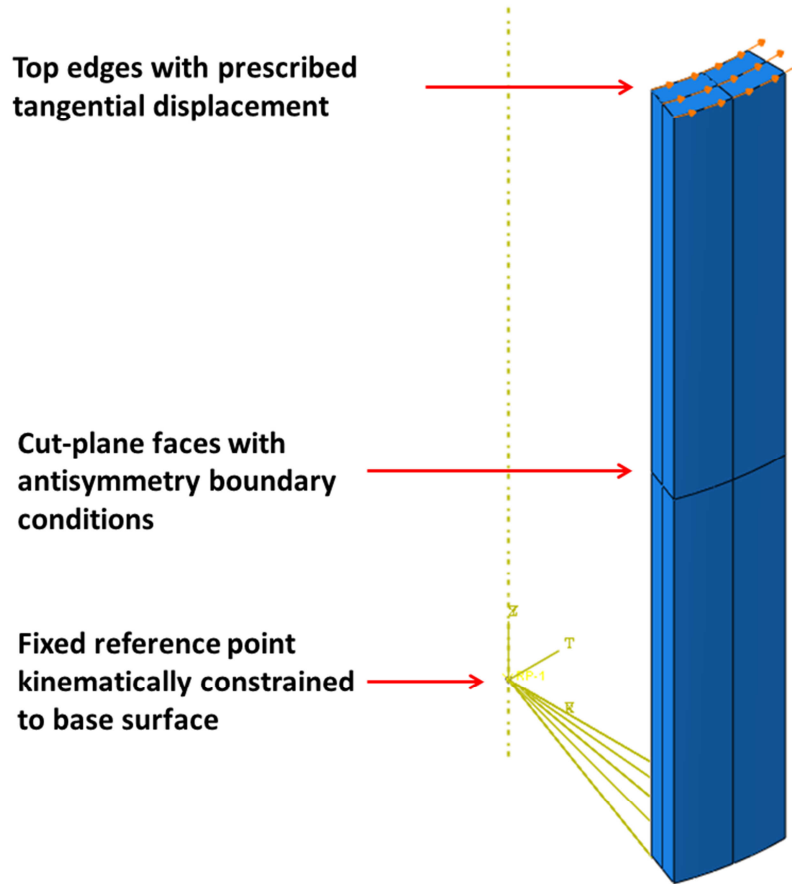


Figure 4.19: The 20-degree wedge model illustrating the displacement controlled loading method.

The displacement at the top of the 360-degree pipe model was measured as  $9.19 * 10^{-4} \text{ rad}$ . Because Abaqus designates the 2-direction for a model in the cylindrical coordinate system to be the tangential direction rather than the circumferential direction, all rotational prescriptions are calculated using Equation (4.31).

$$U_2 = r * \theta \quad (4.31)$$

Where  $U_2$  is the tangential displacement,  $r$  is the radius at a given point, and  $\theta$  is the angle of circumferential rotation measured in radians. Three sections designated by radial coordinate were used on the top surface to apply the tangential boundary condition calculated by Equation

(4.31) using  $\theta = 9.19 * 10^{-4} \text{ rad}$  and given in Table 4.5. The reaction torque measured at the base was  $2.20 * 10^6 \text{ N} * \text{mm}$  which meets the intended torque for a 1/18<sup>th</sup> model to within 0.8%.

The resulting displacement field for the 20-degree wedge agreed with the hand calculation to within 1% and the resulting stress distribution agreed to within 1.7% as shown in Figure 4.20. The twenty-degree wedge has again shown itself able to produce acceptable results using 1/18<sup>th</sup> the number of elements and completing in 1/10<sup>th</sup> of the time needed for the full 360-degree model.

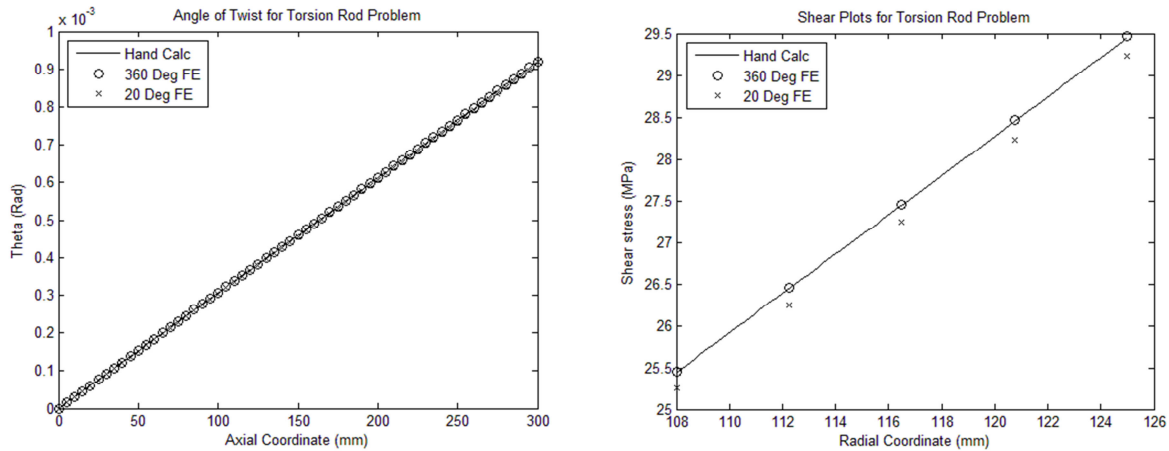


Figure 4.20: An overlay of three solutions for the Torsion bar problem.

#### 4.7.1.6 Characteristics of an Ideal Wedge Model

The actual connection wedge model is a combination of the two models described above. Once the make-up is achieved, the ideal 3D-wedge connection model will have a perfectly symmetric contact pressure distribution about the wedge centerline. The seals will be in contact and the torque reaction measured at the base will be the same as that measured in the lab. At the base, a state of pure torsion will be realized by the absence of reaction forces and the presence of a single reaction moment about the axis. This state of pure torsion will have no reaction moments in the off axis directions.

#### 4.7.1.7 The Difficulty of the Ideal Wedge Model

Currently this ideal wedge model has not been completely achieved with the OCTG premium connection. The torsion bar problem described above assumes the body is continuous, but the actual OCTG premium connection geometry has a discontinuity between the box and pin. This discontinuity in the joint introduces many additional degrees of freedom to the problem which makes it difficult to replicate with simple boundary conditions.

In addition, while the connection make-up displays characteristics of both the composite cylinders problem and the torsion bar problem, the boundary conditions applied to the cut-planes for these two problems are mutually exclusive. If the antisymmetric boundary conditions of the torsion problem are applied to the composite cylinders problem, there will be no restoring moment applied at the cut-plane faces to keep the cylinder wedges in contact where seal results are collected at the midplane. The result of the contact resolution step is a bowing behavior as illustrated in Figure 4.21 which prevents the seals from being in contact at the desired location.

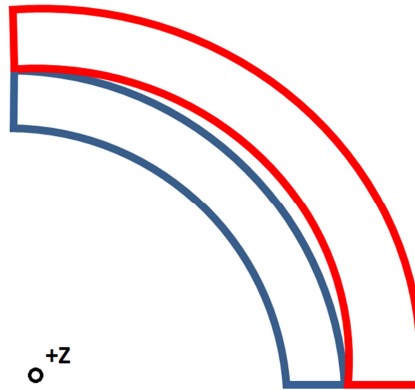


Figure 4.21: Depiction of composite cylinder wedge model behavior with antisymmetric boundary conditions on the cut-planes. The box is shown in red, the pin in blue, and the pipe axis is out of the page.

Despite these boundary condition challenges, the 3D-wedge model still provides the ability to capture the torque-theta relationship of a rotating thread form driving a seal contact. Further study should point to a more representative boundary condition configuration at the cut-planes. By storing the stress state of the composite cylinders solution at the cut-planes and later applying it as a predefined field to construct an initial state for the torsion problem, both constituent problems could be honored.

#### 4.7.1.8 3D-Wedge Loading Scheme

After investigating numerous combinations of boundary conditions and loading schemes for the 3D-wedge model, the best practice was determined as shown in Figure 4.22. The boundary condition application was intended to simplify the final calculation of the connection torque. With only three reaction nodes to produce a moment about the pipe axis on the box, the torque calculation was simplified immensely.

Two reactions were developed at the cut-planes of the box. A large portion of the left and right cut-planes were kinematically constrained to a reference point on the cut-plane surface. Symmetry boundary conditions were applied to these reference points in the tangential direction. The entire cut-plane could not be restricted in the tangential direction to provide flexibility for the contact solution near the seal and threaded regions. Overconstraining this region restricts the slave from moving to accommodate the master surface.

An additional reaction was developed at the base of the box. The bottom surface of the box was kinematically constrained to a reference point located on the pipe axis at the same axial coordinate. This reference point was held fixed throughout the entire analysis. The nominal pipe region of the pin was restricted in the radial direction on the inner diameter to help maintain the radial interference of the seals and threads.

The analysis took place in two steps. The first step was a contact resolution step similar to the composite cylinders problem. During this step, the top surface of the pin was restricted in the axial direction. Several edge partitions of constant radius were created on the top pin surface as shown in Figure 4.19. In the second step, the tangential displacements at these edge partitions were prescribed according to Equation (4.31) to rotate the pin into the box. This displacement controlled loading scheme proved significantly faster than an equivalent force controlled method as the geometric complexity increased.

To prevent the pin and box from separating, an axial displacement was prescribed on the top surface of the pin according to Equation (4.32).

$$u_3 = -(p * \theta) \quad (4.32)$$

Where  $u_3$  is the axial displacement,  $p$  is the pitch of the threadform, and  $\theta$  is the angle of rotation. This top  $u_3$  prescription provided the moments necessary to prevent the pin from snagging at a point, separating from the box and cocking to one side as the rotation progressed. The issue of cocking was detected by a gradient in the tangential displacement field with respect to the axial coordinate as well as a non-symmetric contact pressure distribution. As an additional measure, the threads were prevented from separating once contact had been initiated. This contact constraint allowed the thread form to slide tangentially but prevented separation once surfaces were placed in contact. Checks were performed to ensure that any negative (tensile) contact pressures that developed were kept to a minimum.

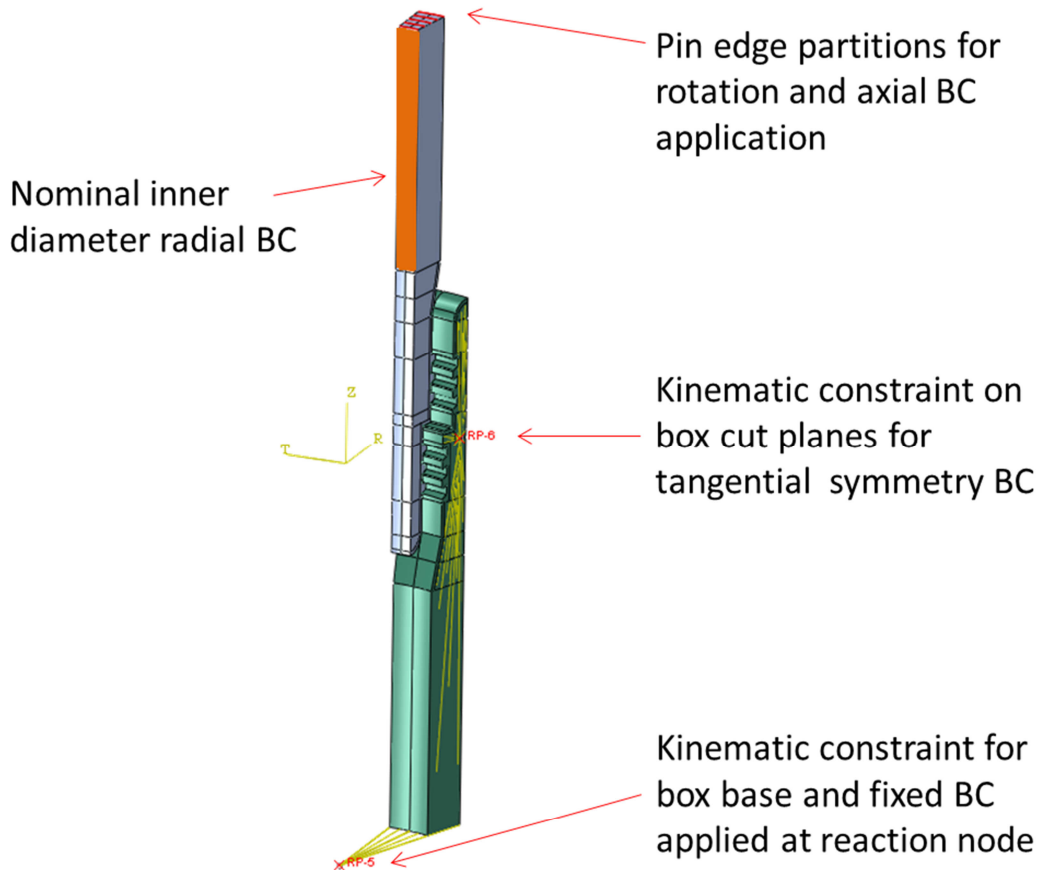


Figure 4.22: Boundary conditions and loading scheme for 3D-wedge model.

As the rotation of the pin progressed, the torque developed at the base reaction node was monitored. The pin rotation continued until the contact solution deteriorated, usually at the high stress concentrations at the seal(s). Several variables were critical to the torque achieved in the connection. The main factor was the quality of the mesh and the level of mesh refinement. The driving factor behind all meshing efforts was the ability to achieve good contact resolution as the

pin was driven into the box. Effectively representing the thread geometry was especially critical as compressive loads were developed in the thread root and crest corners.

A second major contributor to the torque achieved was the specified friction coefficient. It is appropriate to specify a friction coefficient in the 3D-wedge model because the tangential degree of freedom that the friction forces act primarily upon is present. For this reason, the 3D model alone provides the means to determine a representative friction coefficient. Values between  $\mu = 0$  and  $\mu = 0.12$  were tested on the same mesh with the same loads and boundary conditions. The pin was rotated until the contact solution could not accommodate further rotation, and the maximum torque was recorded as shown in Table 4.6.

Table 4.6: Maximum torque achieved by model as a function of friction coefficient.

<b>Friction Coefficient <math>\mu</math></b>	<b>% of Experimental Torque Achieved</b>
0	1.5 %
0.04	37.6 %
0.08	73.8 %
0.12	102.6 %

In the frictionless case, the only mechanism available in the connection to hold torque is the coupling of the pin rotation to the axial compression of the shoulder surface. This mechanism only accounts for a small percentage of the total torque achieved in an experimental connection test. As friction is introduced the tangential forces at the threads, shoulder, and seal surfaces develop and quickly become dominant. Contact convergence becomes more difficult as the friction coefficient exceeds 0.08 and the tangential forces deform elements beyond their useful aspect ratio. A solution was found using a friction coefficient of  $\mu = 0.12$  that achieved the experimental torque values. While this final model did not achieve the idyllic state of pure torsion, it is the closest approximation of the connection make-up state available.

#### 4.7.1.9 Future Application of Predefined Fields to the Torsion Problem

Future improvements could be made to this loading formulation by applying predefined stress fields to superimpose the composite cylinders and torsion problems. Recognizing that the symmetry conditions applied to the cut-planes is only a best approximation of the 360-degree force-displacement relationship, the stress fields at the cut-planes of the composite cylinders solution could be stored and subsequently applied to the torsion wedge cut-planes.

#### 4.7.1.10 360-degree recommendations

Rather than using only a wedge of the connection, an alternative method to solve the make-up problem is to use a simplified version of the full 360-degree geometry. This type of model would have the ability to achieve a state of pure torsion. The tradeoff is that the geometric complexity could not be honored for most premium connections. The fastest way to remove degrees of freedom from the model is by reducing the number of threads, or removing the thread features all together. The thread features could be replaced by a kinematic constraint linking the tangential and axial degrees of freedom of the pin. Approximations would also need to be made for the torque held by the thread form. For simpler connection geometries, a full

360-degree model could be made if great care is taken to concentrate compute effort in only the most critical regions.

#### 4.7.2 3D Inspired Axisymmetric Pretension Loading

The 3D-wedge model has the capability to produce a direct torque-theta relationship and can therefore serve as the link between the experimental connection data and the computationally efficient axisymmetric representation. Because of the extreme jump in modeling complexity, the 3D-wedge model could not attain the level of refinement needed for seal analysis. It can, however, provide valuable information for the proper calibration of the axisymmetric connection model. Without this calibration, a connection analyst is forced to make a best guess assessment of the make-up state when applying pretension section settings. These nonphysical pretension settings can have tremendous impact on the models' seal performance and can be improved with the help of the 3D results.

A technique was developed to replicate 3D seal conditions in axisymmetric form using pretension sections. The resulting make-up seal conditions were converged in the axisymmetric make-up models and stored for later use in service load studies. The 3D to axisymmetric correlation was based on the assumption that the seal condition is primarily a function of the connections' distributed axial displacement on the contact surfaces. The 3D axial displacements at the contact surfaces on both the box and pin were extracted as illustrated in Figure 4.23. These values and the corresponding axisymmetric displacements are plotted on top of each other in Figure 4.24 and Figure 4.25. An iterative process was used to dial in the boundary conditions and pretension section loads that provided the least error at the seals and shoulders. Throughout this process, it was critical to monitor the displacement fields on both the pin outer diameter and the box inner diameter because it is the relative displacement of the two surfaces that affects the seal properties.

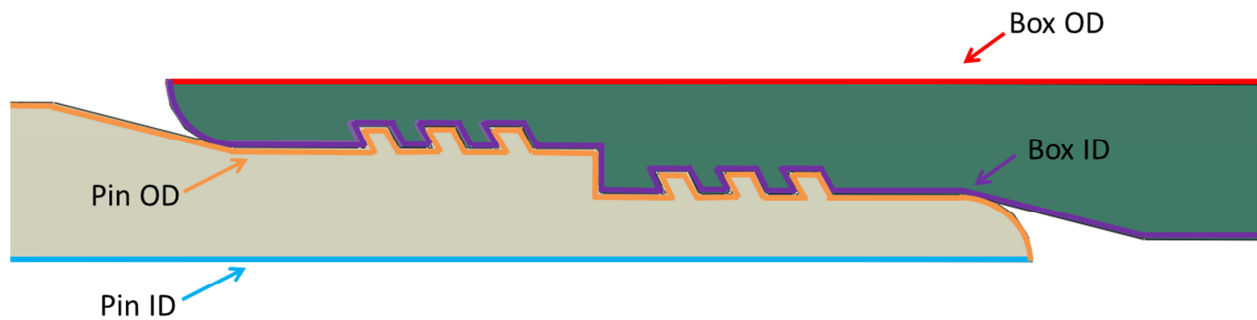


Figure 4.23: Naming conventions shown for Pin and Box surfaces. Displacement results were extracted on both the Box ID and the Pin OD for the 3D-axisymmetric seal calibration.

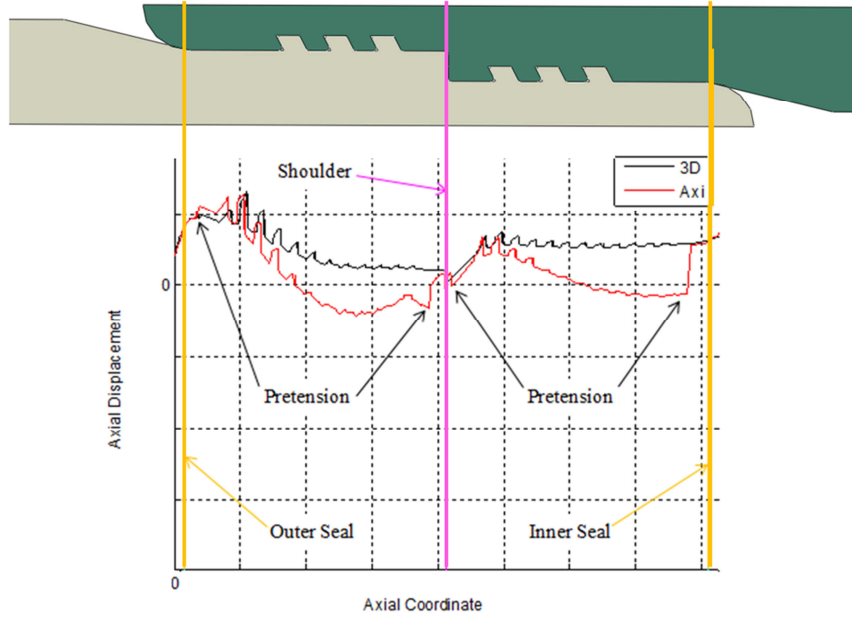


Figure 4.24: Displacement field of the Box ID for the both the 3D and axisymmetric models. The pretension sections are shown as well as the shoulder, inner seal, and outer seal locations.

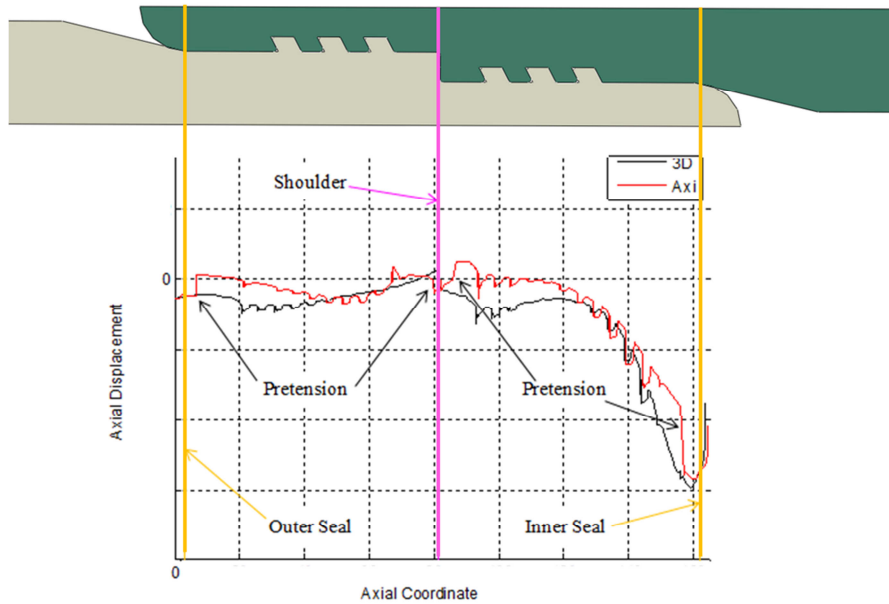


Figure 4.25: Displacement field of the Pin OD for the both the 3D and axisymmetric models. The pretension sections are shown as well as the shoulder, inner seal, and outer seal locations.

One noticeable feature of the final correlated axisymmetric model in Figure 4.24 and Figure 4.25 is that the optimized pretension section offsets are unequal between the regions above and below the shoulder for each member. In addition the pretension offsets are unequal at each seal between the box and pin. At the inner seal, the axial displacement is nearly six times greater in the pin than in the box. This optimized axisymmetric loading scheme reflects the

relative stiffness of the members and would be extremely difficult to accomplish without a 3D calibration.

Several pretension schemes are in practice today, but they are rarely discussed in detail because of their proprietary nature. The pretension section scheme used for this study was selected because it minimized the error with respect to the 3D axial displacement field at the seals and shoulder. The displacement values at the seals and shoulder were given priority over those at the threads because these regions are believed to have the greatest impact on seal performance.

The axisymmetric loading scheme began by defining several surfaces that cut through the geometry at different locations perpendicular to the pipe axis. Pretension sections were then applied at eight locations as shown in Figure 4.26. These pretensions were able to target regions above and below each threaded section. The four pretension sections located near the shoulder were complimented by four axial boundary conditions that provided additional control over the shoulder displacements. These eight modeling features were used to place the shoulder in compression and calibrate the axisymmetric shoulder displacements. The remaining pretensions were used to align the displacements of the seal surfaces through an iterative process.

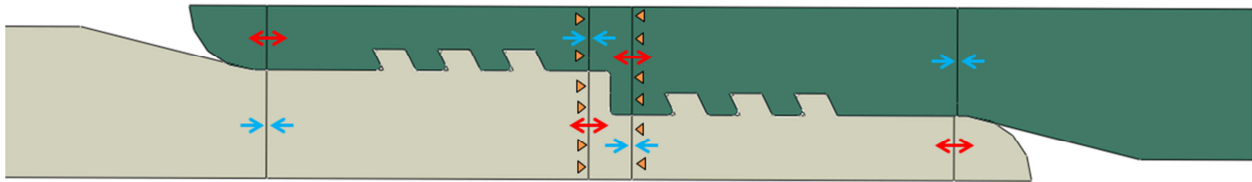


Figure 4.26: Axisymmetric pretension loading scheme shown. Pretensions which dilate shown in red. Pretensions which contract shown in blue. Fixed axial boundary conditions shown in orange.

## 4.8 Seal Metrics

With a loaded connection model in place, several metrics were developed to characterize the effectiveness of the seal. These metrics are based on prior experimental work [8] as well as interviews with engineers in the field. While the absolute indicators of seal integrity are a subject of debate, several theories on the major contributors exist and are presented below.

### 4.8.1 Contact Pressure and the Pressure Penetration Routine

Several models are evaluated under service loads with the help of the Abaqus Pressure Penetration Routine [21]. This routine is indeed a helpful tool when it comes to loading the connection, and for some connection analysts, pressure penetration is the chief evaluation metric in connection analysis. The pressure penetration routine operates by first defining a master and slave contact surface, a critical contact pressure, and a fluid entry point on the seal surface. The critical contact pressure is defined such that it accounts for the asperities present in the seal surface. With the connection under load, the pressure penetration operates such that a simulated fluid pressure is applied normal to the contacting surfaces beginning at the specified fluid entry point until a point is reached on the contact surface where the contact pressure exceeds the specified critical value. At this point the simulated fluid pressure is “stopped” and the seal holds. Conversely, if the contact pressure does not reach the specified critical value, the fluid passes through and the seal fails.

To use the pressure penetration routine as the sole seal metric is to rely purely on the mechanism of contact pressure in the evaluation of seal integrity. However, a closer examination of the seal mechanics reveals that there may be a more comprehensive way to represent the problem. In addition, the intent of the pressure penetration routine does not seem to be that of a conclusive seal metric, but merely a more representative loading mechanism.

#### **4.8.2 Contact Normal Strain**

If the material state of the connection is examined, it is often found that the seal is at a stress state very close to or above the yield stress. Heijnsbroek maintains that in his experiments of dry conical metal-to-metal seals that “No sealing whatsoever was observed with the contact surfaces in the elastic state” and that, “seals must have plastic deformation at the contact surface in order to seal” [8]. The manipulation of seal plasticity is a common technique used by connection designers to ensure that any asperities in the seal surfaces are not able to produce a leak path.

A much more precise evaluation metric may be the use of the normal strain in the contact region rather than the contact stress. By examining the stress strain curve from uniaxial tensile test data such as in Figure 4.8, one can see that in steel near or beyond the onset of yield a small deviation in the measured stress can correspond to a large variation in strain. The converse however is not true. This has led many to believe that the sealing mechanism in metal-to-metal premium connections is strain dominated rather than stress dominated.

#### **4.8.3 Contact Length and Contact Area**

An additional metric commonly monitored in the industry is the length of the seal contact region itself. There is a clear distinction in seal robustness between narrow seals with very large maximum contact stresses and wider seals with lower contact stresses [8]. Some manufacturers require a connection to maintain what is known as a minimum contact area, defined as the area below the contact pressure curve as shown in Equation (4.33).

$$A_c = \int_0^L \sigma_n dl_s \quad (4.33)$$

Where  $A_c$  is the contact area,  $\sigma_n$  is the normal component of the stress tensor,  $l_s$  is the coordinate of length along the seal contact region, and  $L$  is the measured length of the seal contact region.

#### **4.8.4 Strain Energy Density and the Seal Number**

As in many engineering systems, a more appropriate model can often be constructed by applying energy methods rather than using a force based technique [28]. Seals are no different. If we approach the sealing problem from an energy perspective, a more robust indicator of seal performance and convergence can be obtained.

The first law of thermodynamics states that for a system in static equilibrium and under adiabatic conditions, the variation in work of the external forces on the system  $\delta W$  equals the variation in internal energy  $\delta U$  as shown in Equation (4.34) [27].

$$\delta W = \delta U \quad (4.34)$$

The internal energy  $U$  of a volume  $V$  can be expressed in terms of the internal energy density  $U_0$  which is the energy per unit volume. The variation in strain energy density can thus be used to describe the variation in internal energy as shown in Equation (4.35).

$$\delta U = \int_V \delta U_0 dV \quad (4.35)$$

Combining equations (4.34), (4.37), and (4.35) yields an expression for the internal energy density at a point in terms of the stress components and the variation in the strain components.

$$\begin{aligned} \delta U_0 = & \sigma_{xx} \delta \epsilon_{xx} + \sigma_{yy} \delta \epsilon_{yy} + \sigma_{zz} \delta \epsilon_{zz} + 2\sigma_{xy} \delta \epsilon_{xy} + 2\sigma_{yz} \delta \epsilon_{yz} \\ & + 2\sigma_{zx} \delta \epsilon_{zx} \end{aligned} \quad (4.36)$$

In the absence of body forces, the variation of work can be given as a summation of the products of the components of stress and strain as shown in Equation (4.37).

$$\begin{aligned} \delta W = & \int_V (\sigma_{xx} \delta \epsilon_{xx} + \sigma_{yy} \delta \epsilon_{yy} + \sigma_{zz} \delta \epsilon_{zz} + 2\tau_{xy} \delta \gamma_{xy} + 2\tau_{yz} \delta \gamma_{yz} \\ & + 2\tau_{zx} \delta \gamma_{zx}) dV \end{aligned} \quad (4.37)$$

When a connection make-up is performed, the component of strain energy normal to the seal surface provides sealing capability. By performing a coordinate transformation on the principal stress and strain components, the normal component of the strain energy density can be extracted.

If first order axisymmetric elements are used in the seal region, the normal vectors  $\hat{n}_i$  for each element  $i$  may be calculated from the nodal coordinates as shown below. The easiest way to find the normal vectors to each element seal face is to first find the unit vector tangent to the element face  $\hat{n}_{t,i}$  by subtracting the consecutive nodal coordinates in the seal set as shown in Equation (4.41)

$$\hat{n}_{t,i} = \frac{(x_{i+1} - x_i, y_{i+1} - y_i, 0)}{\sqrt{(x_{i+1} - x_i)^2 + (y_{i+1} - y_i)^2}} \quad (4.38)$$

Where  $x$  signifies the axial nodal coordinate, and  $y$  signifies the radial nodal coordinate for element  $i$ . For an axisymmetric problem, the circumferential coordinate is fixed at zero. The unit vector normal to the seal face for element  $i$  is then found by Equation (4.39)

$$\hat{n}_i = \frac{(y_{i+1} - y_i, x_i - x_{i+1}, 0)}{\sqrt{(x_{i+1} - x_i)^2 + (y_{i+1} - y_i)^2}} \quad (4.39)$$

The direction cosines  $l$ ,  $m$ , and  $q$  can be found for the unit normal vector by taking the dot product of the unit normal vector and  $\hat{n}_i$ . For an axisymmetric problem, the direction cosine between  $\hat{n}_i$  and the circumferential unit vector is unity. The transformation vector  $T_i$  can be assembled as shown in Equation (4.40).

$$l_i = [1,0,0] \cdot [n_i] \quad (4.40)$$

$$m_i = [0,1,0] \cdot [n_i]$$

$$q_i = [0,0,1] \cdot [n_i] = 1$$

$$T_i = [l_i, m_i, q_i]$$

The elastic and plastic strains can be extracted at the nodes in the global coordinate system, summed, and transformed into the seal coordinate system by Equation (4.42). In an axisymmetric problem, the strain components  $\gamma_{yz}, \gamma_{xz}$  will be zero. The result is a 1x3 strain tensor transformed into the local seal coordinate system with normal, tangent, and out of plane components.

$$[\epsilon_{total,i}] = [\epsilon_{e,i} + \epsilon_{p,i}] = \begin{bmatrix} \epsilon_{xx} & \gamma_{xy} & 0 \\ \gamma_{xy} & \epsilon_{yy} & 0 \\ 0 & 0 & \epsilon_{zz} \end{bmatrix} \quad (4.41)$$

$$[\epsilon_{seal,i}] = [\epsilon_n, \epsilon_{tan}, \epsilon_{out}] = [T_i][\epsilon_{total,i}] \quad (4.42)$$

Because the normal unit vectors are defined for each element, and the strains are extracted at the nodes, there will always be one more node in the seal set than the number of normal vectors if first order elements are used (See Figure 4.27). This issue can be overcome for the interior nodes in the set by averaging the two normal vectors  $n_i$  and  $n_{i-1}$  in the computation of  $T_i$ .

The calculation of the seal strain energy density continues with the extraction of the contact pressure in the seal region,  $\sigma_n$ . This contact pressure is readily available to users of most commercial finite element packages, but it can also be calculated in the same manner as  $\epsilon_n$ . The normal strain energy density  $U_{0,n}$  can now be calculated at each node as shown in Equation (4.43).

$$U_{0,n} = \sigma_n * |\epsilon_n| \quad (4.43)$$

If the normal strain energy is integrated along the length of the seal, a single representative number describing the seal state under a given load configuration results. This Seal Number is shown in Equation (4.44).

$$SN = \int_0^L (U_{0,n}) dl_s = \sum_{i=1}^j \sigma_{n,i} * |\epsilon_{n,i}| * L_i \quad (4.44)$$

Where  $SN$  is the Seal Number,  $L$  is the length of the seal,  $l_s$  is the seal coordinate as shown in Figure 4.27, and  $j$  is the number of elements in contact in the seal region.

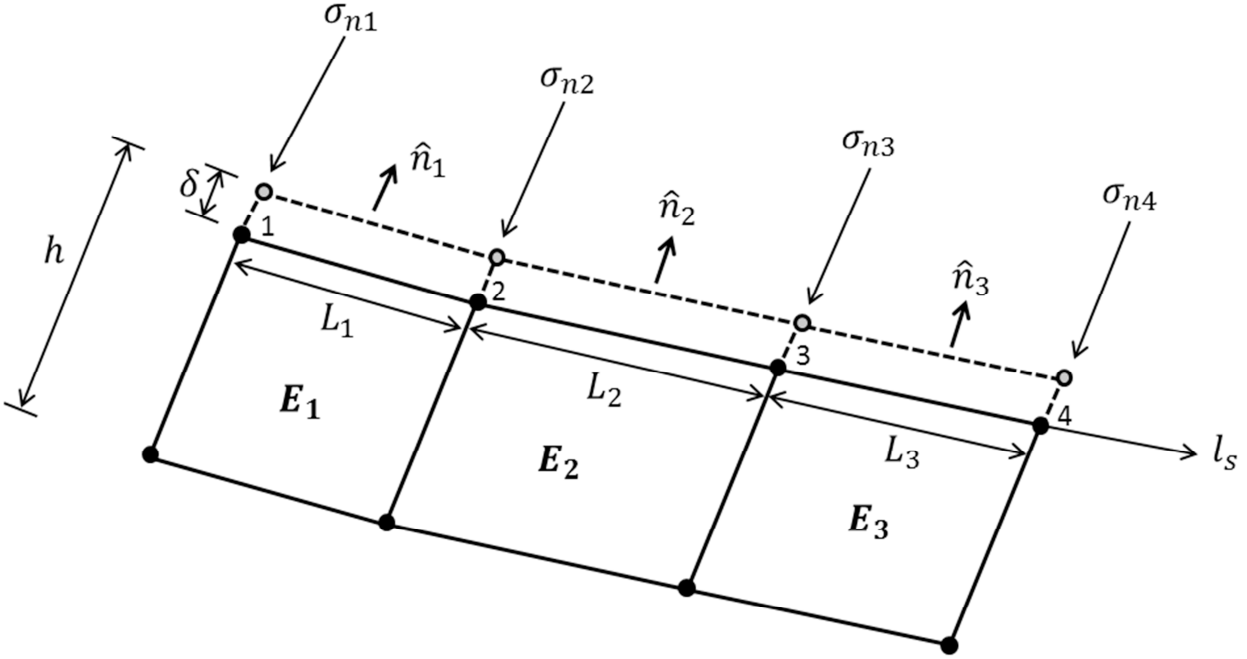


Figure 4.27: Components used in the calculation of the Seal Number; the element height  $h$ , change in element height due to load  $\delta$ , the component of the stress tensor normal to the seal surface projected to the node  $\sigma_{ni}$ , the seal surface unit normal vectors  $\hat{n}_i$ , the element seal face lengths  $L_i$ , and the seal coordinate  $l_s$ . The normal strain can be visualized as  $\epsilon_n = \delta/h$ .

Because it uses an integration scheme, the Seal Number is able to smooth out the noise often found in contact pressure and normal strain data extractions and has shown to be a robust indicator of seal convergence. The Seal Number allows the analyst to give credit to the seal characterization methods of contact pressure, contact area, contact strain, and contact length while concisely representing the state of the seal with a single energy based value.

#### 4.8.5 Convergence of Seal Metrics

None of the above seal metrics can be considered representative without an accompanying convergence plot. The percent convergence indicates how close the model is to representing a value extracted from an infinite-degree-of-freedom model under the same loads and boundary conditions. The percent convergence is calculated as shown in Equation (4.45) and is in essence the percent error between two meshes.

$$\% Conv = \frac{(x_i - x_{i-1})}{x_i} * 100\% \quad (4.45)$$

Where  $x_i$  is a result extracted from model  $i$ , and  $x_{i-1}$  is the same result extracted from the same model but containing fewer degrees of freedom. A sample of typical axisymmetric convergence values is given in Table 4.7. Seal metric convergence is best visualized as a function of the number of nodes in the seal region with a positive contact pressure as shown in Figure 4.28.

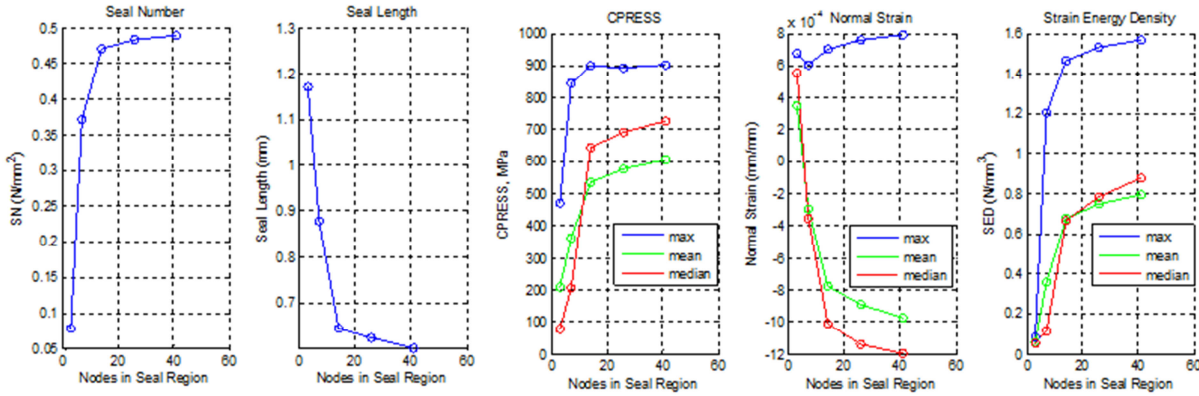


Figure 4.28: Convergence plots for each seal metric

Particular attention must be given to the seal length metric when examining model convergence. Typical industry mesh sizing only results in 8-9 seal nodes in contact. As seen Figure 4.28, this mesh sizing over predicts the seal length by nearly 45%. A false confidence will result if such a coarse mesh is used for the prediction of seal performance. Further refinement provides a much more accurate representation of the seal state at the expense of a slight increase in computation time. The seal length was converged to 3.7% in a model containing 125,000 bilinear axisymmetric elements which completed in 25 minutes on 12 cores.

Table 4.7: Typical seal metric convergence levels.

Metric	Convergence
Seal Number	1.2%
Seal Length	3.7%
Max Contact Pressure	1.1%
Mean Contact Pressure	5.0%
Median Contact Pressure	4.9%
Max Normal Strain	4.2%
Mean Normal Strain	8.7%
Median Normal Strain	4.9%

#### 4.8.6 Seal Metric Results and Discussion

The above seal metrics were evaluated on a connection provided by a major connection manufacturer. The connection type, weight, and grade were kept constant. Four geometric variants were made available for analysis: LL-PSBF, HL-PNBN, HL-PSBF, and HH-PFBS.

The above naming convention allows manufacturers to conceal design details while still providing customers with the geometric extremes within the allowable tolerances. The names are constructed to designate the connection thread interference, seal interference, and taper mismatch as illustrated in Figure 4.29. The first letter designates the thread interference: Low, Nominal, or High. Similarly the second letter designates the seal interference. The remaining four letters after the dash (-) designate the taper mismatch. The letter following the 'P' designates the pin taper: Low, Nominal, or High. Similarly the letter following the 'B' designates the box taper. The ideal connection is a NN-PNBN. This NN-PNBN geometry was not analyzed but would provide a good baseline for evaluation of the other variants. Often the

geometries analyzed by well designers are LL-PSBF, HL-PNBN, HL-PSBF, and HH-PFBS because it is commonly believed that one of these will provide the worst case performance under a given service load [4,9].

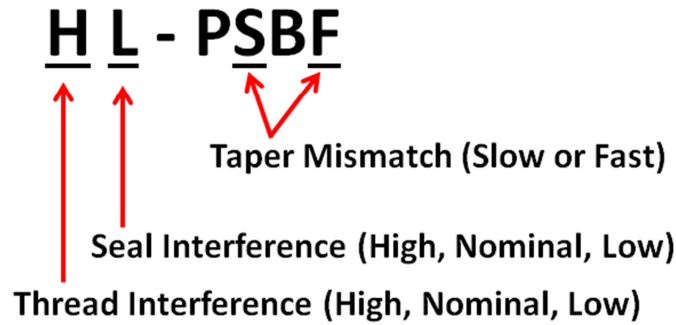


Figure 4.29: Diagram of connection naming conventions illustrating the “High Low – Pin Slow Box Fast” configuration.

Due to limitations in project scope, only the LL-PSBF model was generated in 3D. The process outlined in Section 4.7.2 was used to generate an equivalent LL-PSBF axisymmetric model with pretension section loading. The same pretension settings were then applied to the remaining axisymmetric geometries. This set of models provided a basis for geometric comparison as well as evaluation of seal metric capabilities. To preserve the proprietary information of the connection design, all results given below have been normalized or multiplied by an arbitrary scaling factor.

#### 4.8.6.1 Contact Pressure and Normal Strain

The contact pressure metric was able to provide valuable insight into the variation in sealing capacity present in a given connection pulled from the production line. Table 4.8 shows the maximum, mean, and median contact pressure in the seal region after make-up. These values have been normalized to the material’s yield offset stress  $\sigma^o$  calculated from uniaxial tensile test data in Section 4.4.1. HH-PFBS shows stress values far beyond the yield offset. It is indeed feasible that stress values beyond yield can be achieved because in some areas the seal is nearing a state of hydrostatic compression. The drastic contrast in seal contact pressure between the high seal interference of HH-PFBS and the low seal interference of HL-PSBF should also be noted. In addition, the contact pressure metric can distinguish between the nominal taper variation of HL-PNBN and the assumed worst case taper variation of HL-PSBF.

Table 4.8: Contact Pressure results from the comparative seal analysis. Results extracted from equivalent axisymmetric model configurations developed from 3-D wedge models and correlated with DIC data.

Model	Contact Pressure					
	Max ( $\sigma_n/\sigma^o$ )	Percent Converged	Mean ( $\sigma_n/\sigma^o$ )	Percent Converged	Median ( $\sigma_n/\sigma^o$ )	Percent Converged
LL-PSBF	1.02	0.9	0.69	5.2	0.79	-2.3
HL-PNBN	0.97	3.4	0.55	5.8	0.52	2.2
HL-PSBF	0.69	1.9	0.27	2.3	0.21	4.8
HH-PFBS	1.29	0.0	0.91	2.5	1.06	1.6

Statistics on the normal strain values ( $\epsilon_n$ ) are given in Table 4.9. The normal strain is the component of the total strain perpendicular to the contact surface as calculated in Equation (4.42). The values presented have been normalized to the offset yield strain ( $\epsilon^o$ ). Convergence of the normal strain values is more difficult than the contact pressure values because total strain levels at a point vary greatly with a small increase in stress beyond  $\epsilon^o$ .

Table 4.9: Normal Strain results from the comparative seal analysis. Results extracted from equivalent axisymmetric model configurations developed from 3-D wedge models and correlated with DIC data.

Model	Normal Strain					
	Max ( $\epsilon_n/\epsilon^o$ )	Percent Converged	Mean ( $\epsilon_n/\epsilon^o$ )	Percent Converged	Median ( $\epsilon_n/\epsilon^o$ )	Percent Converged
LL-PSBF	0.131	7.6	-0.167	9.1	-0.208	11.3
HL-PNBN	0.126	7.9	-0.116	11.3	-0.120	11.8
HL-PSBF	0.117	5.8	-0.011	38.8	0.010	-19.2
HH-PFBS	0.189	6.9	-0.201	5.0	-0.250	3.2

#### 4.8.6.2 Seal Length

The seal length's for the geometric variants have been multiplied by an arbitrary constant 'X' and are shown in Table 4.10. The negative sign on the convergence values indicates that the metric converges from above. As previously mentioned in Section 4.8.5 this level of convergence must be closely monitored if a minimum seal length requirement is imposed. By looking at Table 4.8 and Table 4.10 simultaneously it can be seen that HL-PSBF has both the lowest contact pressure and the greatest seal length. It is this phenomenon that leads many designers to impose both a seal length requirement as well as a contact pressure requirement. The converse, where the shortest seal length coincides with the highest contact pressure, does not exist in this data set.

Table 4.10: Seal Length results from the comparative seal analysis. Results extracted from equivalent axisymmetric model configurations developed from 3-D wedge models and correlated with DIC data.

Model	Seal Length (mm*X)	Percent Converged
LL-PSBF	0.81	-3.0
HL-PNBN	1.03	-4.3
HL-PSBF	1.57	-1.3
HH-PFBS	1.00	-0.3

### 4.8.6.3 The Seal Number

The seal number from Section 4.8.4 combines aspects of the contact pressure metric, the strain metric, and the seal length metric into a single energy based value. The seal number results for the available geometries have been scaled by an arbitrary constant 'X' and are given in Table 4.11. One noticeable aspect of the seal metric is that it converges much faster than the contact pressure or seal length. This can be attributed to the use of an integration scheme, shown in Equation (4.44), which has a smoothing effect on the data.

When comparing the seal number across the available geometries, a maximum is reached where expected on the high thread and seal interferences of HH-PFBS. The seal number reaches only half this value on the low thread and seal interference configuration of LL-PSBF. As the seal interference is further reduced in the high thread, low seal configuration of HL-PNBN a slightly lower seal number of  $0.42 * X$  is achieved. Finally, the seal number proves to be considerably diminished on the traditionally worst-case HL-PSBF geometry with its high thread interference, low seal interference, and mismatch in taper. Here, the seal number shows an ability to differentiate between nominal and offset taper angles- a feature that is apparent but not nearly as noticeable in the contributing seal length, normal strain, and contact pressure metrics.

Table 4.11: Seal Number results from the comparative seal analysis. Results extracted from equivalent axisymmetric model configurations developed from 3-D wedge models and correlated with DIC data.

<b>Model</b>	<b>Seal Number (N/mm<sup>2</sup>*X)</b>	<b>Percent Converged</b>
LL-PSBF	0.51	1.0
HL-PNBN	0.42	0.5
HL-PSBF	0.14	0.6
HH-PFBS	1.00	0.8

# Chapter 5 Calibration of the Finite Element Model

Several finite element modeling techniques were attempted before the final 3D-wedge and 3D-inspired axisymmetric pretension techniques were determined. In this model development process, several error metrics were used to help steer the efforts of the study towards the best available solution based in the DIC data. These metrics are valuable not only because they quantitatively determine the error present in the models, but are also able to reveal the nature of the error and the path forward for model improvement. The metrics are evaluated on both the axisymmetric and 3D finite element models.

## 5.1 Model Error Metrics

The error metrics operate on two data sets: the DIC data and the finite element model. The term correlation will refer to the combined notion of the traditional correlation coefficient, the sum-squared error (SSE) between the two data streams, and the sum squared error of the spatial frequency content (FFT SSE). All correlations discussed will be the finite element data relative to the experimental DIC strain and displacement field reference.

### 5.1.1 The Correlation Coefficient

The traditional correlation coefficient is a measure of linear dependence between variables [24]. The correlation coefficient is normalized to a scale from -1 to 1. High correlation coefficient magnitudes (positive or negative) correspond to a strong relationship between two variables. Negative correlation coefficients indicate an inverse relationship. Correlation coefficients are not sensitive to the order of magnitude of the data set (scale) or vertical (DC) offsets. They are a measure of a variables' trend rather than its numerical value. The final correlation coefficients of the 3D-wedge model are given in Table 5.1, and show that the trends in the finite element models' mechanics are representative of the DIC displacement and strain data. By comparison, the axisymmetric displacement fields were only able to produce levels of correlation of 0.4.

Table 5.1: Correlation coefficients for the final 3D-wedge model

	Radial Displacement	Circumferential Displacement	Axial Displacement	Circumferential Strain	Axial Strain
Correlation Coefficient	0.802	0.624	0.617	0.928	0.930

### 5.1.2 Data Set Alignment

Prior to correlation the axial origin of the FE data set must be registered with the axial origin of the DIC data. This is necessary because the FE model data is not guaranteed to begin at the same physical location as the DIC data unless great care has been taken in the experiment to orient the DIC images to a stationary, well documented coordinate system. The process of registering the axial origins of the two data sets is illustrated by Figure 5.1. The process begins at the origin of the DIC data set and compares the interpolated FE data set to the DIC data set using the correlation coefficients. The FE data set is then given a phase offset  $\phi$  bounded by Equation (5.1).

$$0 \leq \phi \leq \phi_{max} \quad (5.1)$$

The maximum phase offset,  $\phi_{max}$ , has been fixed at 50 mm for speed and correlation accuracy. At each phase offset evaluation the FE data set has to be interpolated from the nodal values to maintain a one-to-one spatial relationship with the DIC data. All  $\phi$  are evaluated within the limits, and the largest correlation coefficient is recorded with its associated optimum phase offset  $\phi_{optim}$  as shown in Figure 5.1. The axial coordinate of the final point in the offset FE data set is determined, and the DIC data is trimmed to maintain equivalent spatial length  $L_{FE}$  in both data sets. This is needed because the FE and DIC data are not guaranteed to cover the same spatial length.

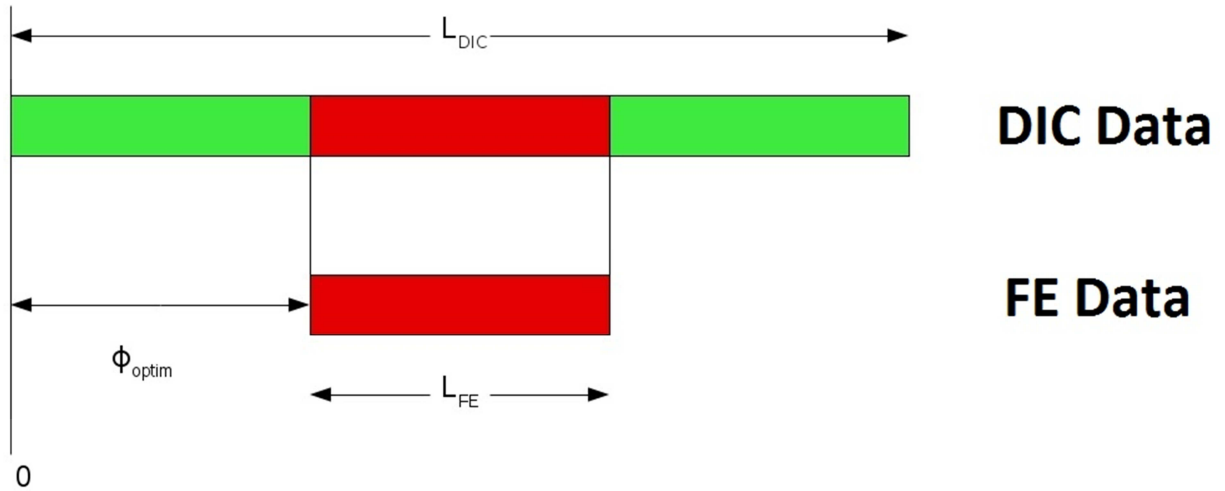


Figure 5.1: Alignment of data sets.  $\phi_{optim}$  is the phase offset that produces the largest correlation coefficient. The trimmed data sets (illustrated in red) are passed forward for error metric evaluation.

In the search for the optimum phase offset, the correlation coefficient was calculated using data over the full connection length. This decision produces a data alignment that does not favor any particular region of the connection, despite the fact that some regions along the axis contain more dynamic signals than others. An alternate formulation for middle shoulder connections is to only consider the ‘upper’ half of the connection between the shoulder and the outer seal for the data alignment. It is in this upper region that the displacement and strain signals have a higher signal-to-noise ratio as seen in Figure 3.4 and Figure 3.7. The reason for the low SNR below the shoulder is the additional thickness of the box as shown in Figure 4.23. The added thickness in this section smooth’s out the frequency content of the data on the outer diameter as the strain energy is dissipated from the thread contact surface.

### 5.1.3 Sum Squared Error

The modified FE data with the best correlation coefficient and the trimmed DIC data are then compared using the sum squared error method of Equation (5.2). The SSE is the sum of the pointwise difference between the FE model data and the mean zero DIC data. This quantity is then normalized to the maximum value of the DIC data. The sum-squared error is necessary to quantitatively show the spatial relation between the two data sets. The sum squared error values for the final 3D-wedge model are given in Table 5.2.

$$SSE = \sum_{i=1}^n \left( \frac{(FE_i - DIC_i - \text{mean}(FE - DIC))^2}{\max(DIC)} \right) \quad (5.2)$$

Table 5.2: Sum Squared error values for the final 3D-wedge model

	<b>Radial Displacement</b>	<b>Circumferential Displacement</b>	<b>Axial Displacement</b>	<b>Circumferential Strain</b>	<b>Axial Strain</b>
<b>SSE</b>	0.407	8.21E-3	0.085	1.21E-3	6.33E-3

### 5.1.4 Fast Fourier Transform

The Fast Fourier Transform provides an orthogonal view of the data as shown in Figure 3.9. The FFT allows the DIC and FE data streams to be viewed through a different characterization, spatial frequencies and amplitudes. In order to be able to perform an FFT on the two data sets, the data points must be sampled at a fixed spatial interval and the number of data points must be a power of 2. To capture the relevant frequency content in the displacement and strain fields, the FFT should be constructed such that it can capture wavelengths as small as the pitch of the thread form, and as large as the total length of the connection.

For example if the spatial length of the two data streams is 200 mm and the pitch is 5 mm, resampling the data at 512 equally spaced points would produce  $512/2.56+1=200$  spectral lines, plus an additional spectral line when the DC component is included. The resulting spatial frequency range would be from  $1/200\text{mm} = 0.005$  cycles/mm to  $0.005\text{cycles/mm} * 200$  spectral lines = 1 cycle/mm. With these FFT parameters, wavelengths between 1 and 200 mm could be captured on the outer diameter of the box. This is sufficient to capture features smaller than the pitch of 5mm and as large as the entire connection length. The final FFT plots of the DIC and FE data can be found in Figure 5.2.

The spatial frequency content of some components is represented better than others by the finite element model. While the radial and circumferential displacement as well as the circumferential strain field show remarkable similarity, the axial displacement and axial strain fields are more difficult to represent.

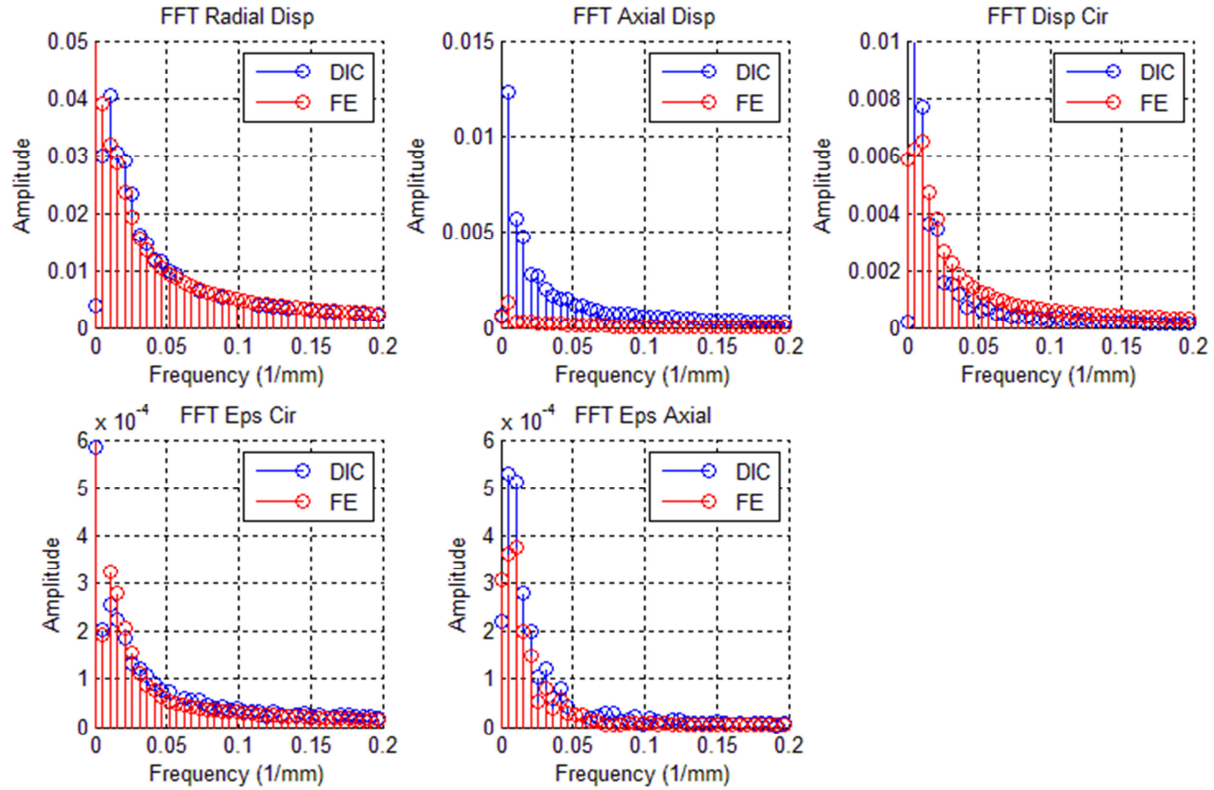


Figure 5.2: FFT overlays of the FE and DIC data. Note: The vertical scales are not constant in this image.

Another way to characterize the difference in the spatial frequency content is to use a sum squared error metric. By summing the difference between the amplitudes at each spectral line of the two FFT's, an FFT sum squared error (*FFT SSE*) was calculated as shown in Equation (5.3).

$$FFT\ SSE = \sum_{i=1}^n (FE_i - DIC_i)^2 \quad (5.3)$$

Where  $n$  is the number of spectral lines,  $FE_i$  is the  $i$ 'th spectral line for the finite element data set, and  $DIC_i$  is the  $i$ 'th spectral line for the DIC data set. FFT sum squared errors are given for the final model in Table 5.3.

Table 5.3: Fast Fourier Transform sum squared error values for the final 3D-wedge model

	Radial Displacement	Circumferential Displacement	Axial Displacement	Circumferential Strain	Axial Strain
SSE FFT	2.02E-2	4.28E-04	2.05E-04	1.49E-7	8.30E-9

### 5.1.5 Analysis of the Residuals

Examining the residuals throughout the model development process provided insight into model and data acquisition improvement. An ideal model correlation would result in a residual signal randomly distributed about the mean with a maximum value significantly less than the

amplitude of the signal itself. There should be no physics remaining in the ideal residual signal. A residual analysis performed on an early model is shown in Figure 5.3. The radial displacement residual signal shows a variation in the pointwise difference between the finite element model and DIC data with respect to the axial coordinate. This type of error is due to the common rigid body rotation mode of the connection in the test facility. Because no fiduciary marks were available a rotation subtraction operation could not be performed on the DIC data to improve this type of error.

A mean offset can be seen in the both radial and axial displacement signals. This is indicative of a rigid body translation mode present in the DIC displacement data and can be corrected by subtracting the mean of the residual. Additional justification for this operation could be provided by observing the translation of available fiduciary marks in the test. The circumferential and axial strain residuals for this model do show a mean zero error that is more randomly scattered about the mean. Because of the spatial derivative of the strain components, any rigid body displacements and rotations are removed.

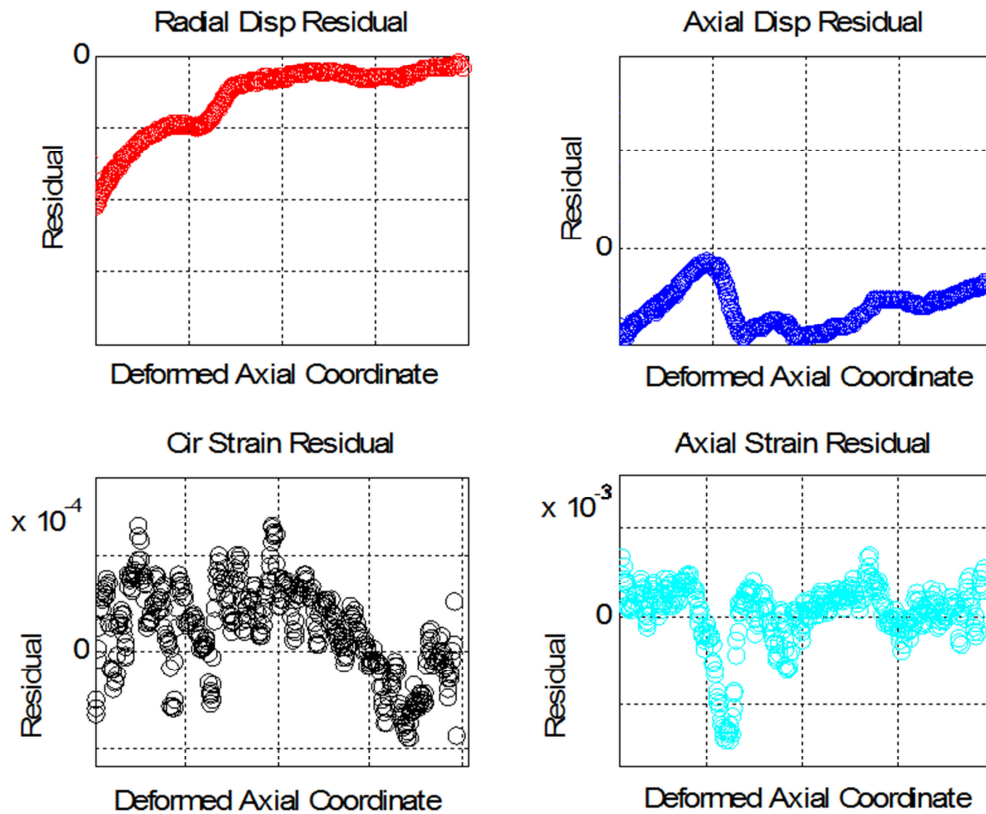


Figure 5.3: Example plots of the residual analysis.

The FFT of the residual displacement signal shown in Figure 5.4 illustrates the spatial frequency error of the model. The FFT of the displacement residuals also shows a mean offset in the zero Hertz (DC) component.

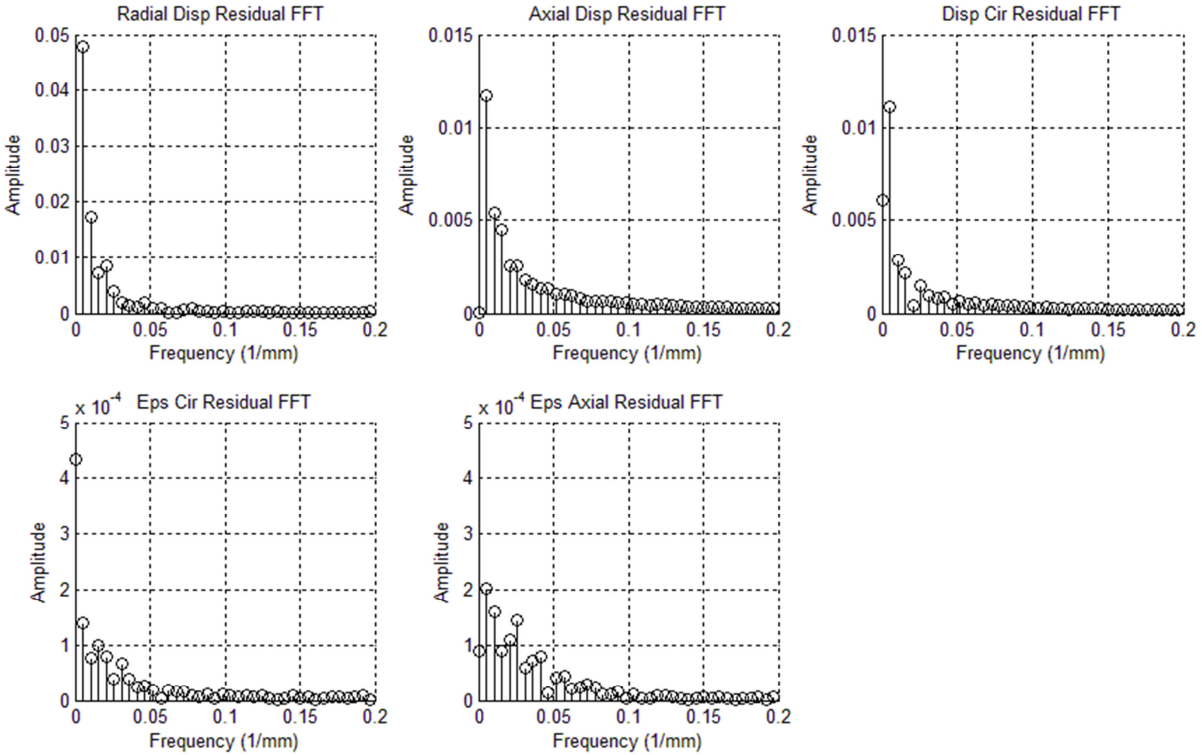


Figure 5.4: FFT of the residuals for the final correlated model. The FFT SSE from Equation (5.3) is a squared summation of the above data.

## 5.2 Identifying the Minimum Error Make-up Model

Many of the metrics in Section 5.1 were developed with a goal of optimizing the axisymmetric connection formulations used in industry today. The metrics have been able to quantitatively determine the effects of finite element modeling decisions using full-field DIC strain and displacement data as the reference. As discussed in Chapter 4, it was eventually determined that only a 3D model could provide the necessary degrees of freedom to capture the torque-theta relationship of a connection make-up. Because of the immense computational cost of a full 3D representation, a 3D-wedge model was developed and later used to guide the computationally efficient axisymmetric formulation. The most representative connection make-up model found during the course of the study was the 3D-wedge model that achieved experimental torque values. The outer diameter displacement and strain fields for this final 3D-wedge model are plotted in Figure 5.4 along with the corresponding DIC data.

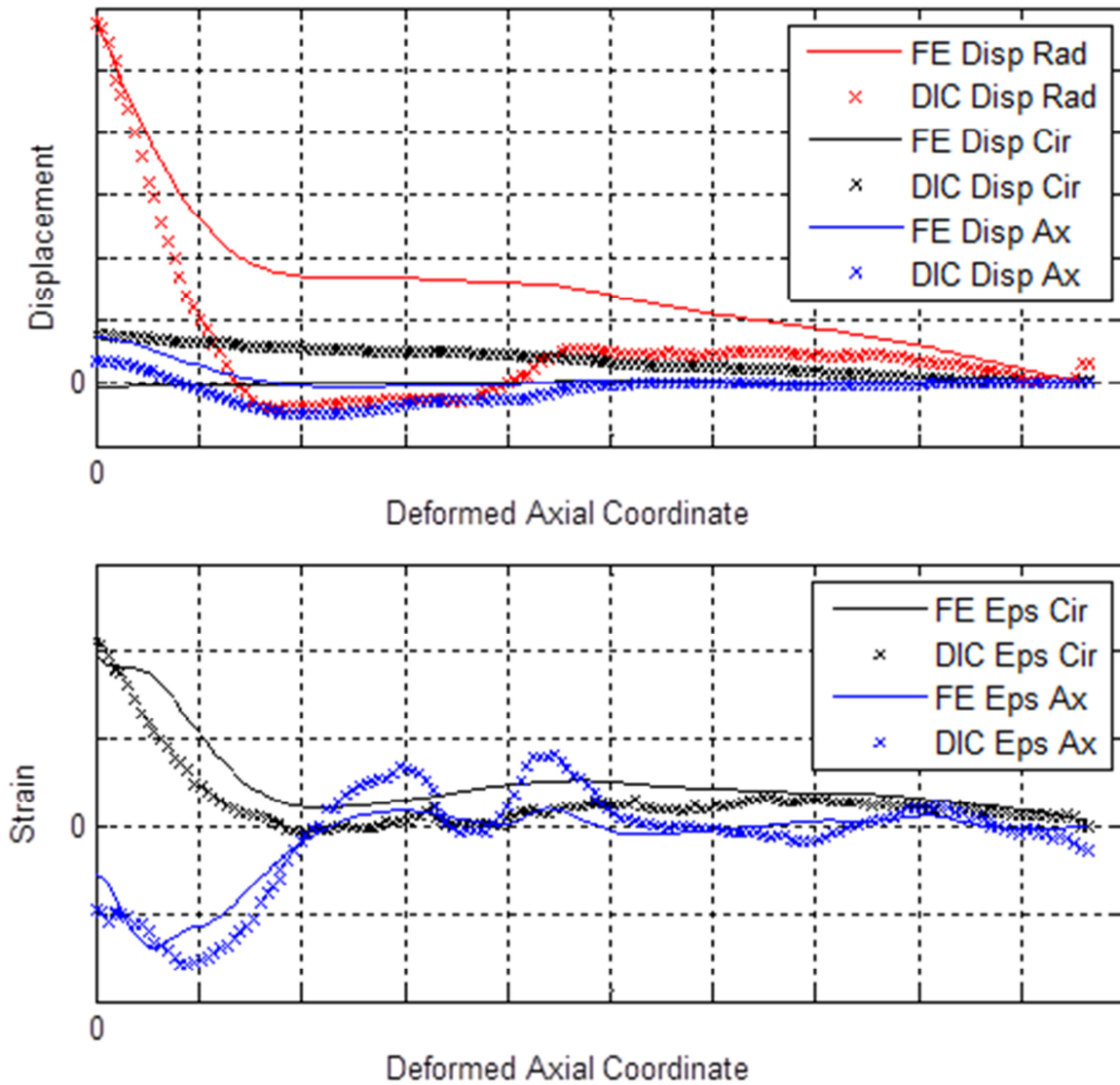


Figure 5.5: Final overlay of 3D-wedge finite element data and extracted DIC data. Displacements (top) and Strains (bottom) show strong resemblance.

The plotted strain data provides visual confirmation of the model's ability to capture the trends in the mechanics of the connection. This is confirmed by the high correlation coefficients for the strain data shown in Table 5.1. The overall trends in the displacement data appear to be adequately represented by the finite element model as well. Improvements to the displacement correlation can be made by establishing the true rigid body motion in the experimental data. This can be done by registering the DIC data with fiduciary marks as discussed in Section 3.2.1. The 3D-wedge model does not represent the DIC data perfectly, but provides substantial improvement over axisymmetric pretension section representations. It is unlikely that much improvement can be made to the modeling technique without applying predefined fields to place the connection in pure torsion as discussed in Section 4.7.1.9 or extending the 3D model to 360 degrees as discussed in Section 4.7.1.10.

# Chapter 6 Summary, Conclusions, and Recommendations

## 6.1 Summary and Conclusions

From a review of the literature, Hilbert and Khalil have identified that a need exists for a general correlation between torque and equivalent axisymmetric loading for OCTG connection make-ups. Heijnsbroek adds that axial displacement is the dominant mechanism linked to sealing capability. The literature also reveals that strain gauge methods do not provide enough spatial resolution to properly capture the complex OCTG outer diameter strain fields. The conclusion drawn is that confidence in any OCTG modeling technique can only be as good as the resolution of the corresponding experimental data.

The use of DIC in connection testing means that finite element connection models may now be held to higher standards. DIC strain and displacement measurements can provide high-spatial-density full-field validation data for finite element models of OCTG premium connection make-ups. This ability hinges on the requirement that appropriate correlation techniques are used. Fiduciary marks are necessary to provide a concrete reference for mapping the DIC data back to the geometry and accounting for any rigid body motion present in the system. Best practice recommendations are made throughout Chapter 3 if these marks are not available.

Metrics such as Signal to Noise Ratio can be used to quantitatively assess the DIC data quality as shown in Section 3.4. The calibration, paint pattern, lighting, and camera orientations have been shown to drastically influence data quality. DIC data processing must be done carefully and with knowledge of the mechanics of the system at hand. Data robustness can be improved by sampling at several circumferential coordinates and using a median technique to collapse the data into an axisymmetric equivalent form. The value of extracting both strains and displacements cannot be overlooked. The strength of the experimental displacement signals is the ability to calibrate the model to the scales of the connection behavior. The strain signals offer the ability to represent the trends present in the mechanics of the system. Filtering is necessary and should be used with caution to avoid over processing the data set.

Chapter 4 describes the technique and reasoning behind the construction of the finite element make-up model. The truest available finite element model of a connection make-up is a full 360-degree representation of the box and pin using 3D continuum elements. This representation has no associated modeling assumptions. Unfortunately, this type of model is often intractable.

When recognized and appropriately exploited, axisymmetry can reduce the number of degrees of freedom in a finite element model while maintaining sufficiently accurate solutions. However, OCTG connections are not axisymmetric because the helix angle of the thread form causes a variation in geometry with respect to the circumferential coordinate. In addition, the mechanism of rotating the pin at make-up results in a variation of the displacement field with respect to the circumferential coordinate. This mechanism cannot be directly modeled in a conventional axisymmetric model.

Relying on a turn-pitch calculation to determine pretension axial offsets at discrete points neglects the fact that the connection is a complex distributed elastic system. The pretension section loading method can only be deemed an acceptable representation of a connection make-

up if a concrete, mechanics-based link is made between the applied torque and the resulting axisymmetric displacement field. Only a 3D representation can provide this link.

The 3D-wedge model offers the ability to capture the torque-theta relationship with considerably fewer degrees of freedom than the full 360-degree representation. Because the circumferential degree of freedom is activated, the 3D-wedge model incorporates the torsional stiffness's of the box and pin. In addition, a direct kinematic relationship between the pin rotation and the distributed axial displacement of the system is now available.

Several recommendations are made for the construction of the 3D-wedge model. A Ramberg-Osgood deformation plasticity material model is found to be a very effective representation of the stress-strain constitutive behavior. This form was chosen in Section 4.4 because it allows both the elastic and plastic material behavior to be represented by a single smooth curve. The proper definition of a continuous transition between elastic and plastic behavior is necessary to appropriately capture the plastic zones that develop throughout the geometry.

In Section 4.5, it is demonstrated that great care and effort must be devoted to the meshing scheme to achieve a stable mesh that can successfully converge a difficult contact solution in a reasonable amount of time. This is especially critical in 3D applications where efficient and effective meshes drive the model's contact performance. The ability of the connection model to support experimental torque values was limited primarily by its ability to resolve the contact problem at the threads, seals, and shoulder as the pin was driven into the box. Section 4.6 illustrates that no single contact resolution method will adequately satisfy every modeling case, and several complimenting methods have been developed for varying levels of contact severity.

For the wedge model to represent the full 360-degree make-up, the unmodeled portion of the connection must be represented using loads and boundary conditions as discussed in Section 4.7. An appropriate set of boundary conditions is determined by viewing the make-up as a superposition of the composite cylinders problem and the torsion bar problem. The 360 results of these constituent problems can be reproduced with sufficient accuracy in 1/10th the time using a 20-degree wedge section. The challenge realized is that the boundary conditions for these two constituent problems are mutually exclusive. A compromise is reached in Section 4.7.1.8 and the 3D-wedge model is able to couple torque, rotation, and axial displacement at the thread form to drive contact at the shoulder and seals. While this final model did not achieve the idyllic state of pure torsion, it is the closest approximation of the connection make-up state available.

The 3D-wedge model can now serve as the link between the experimental connection data and the computationally efficient axisymmetric model. In Section 4.7.2 the axisymmetric representation is forced into agreement with the 3D-wedge model through an iterative process by monitoring the axial displacement at the shoulder and seals.

With a representative axisymmetric connection model in place, several metrics are developed in Section 4.8 to characterize the seal effectiveness. None of the seal metrics may be considered representative without an accompanying convergence plot. Particular attention must be given to the seal length metric when determining model convergence. The convergence plots provided illustrate how a false confidence will result if an unconverged mesh is used for the prediction of seal performance. Current industry mesh density produces seal length values 45% higher than models with greater mesh refinement. This refinement provides a much more accurate representation of the seal state at the expense of a slight increase in computation time.

The contact pressure metric was able to provide valuable insight into the potential variation in sealing capacity present in a given connection pulled from the production line. The Seal Number shows an ability to differentiate between nominal and offset taper angles- a feature that is apparent but not nearly as noticeable in the contributing seal length, normal strain, and contact pressure metrics.

In Chapter 5 modeling error metrics are developed using the DIC data as the reference. These metrics are valuable not only because they quantitatively determine the error present in the models, but can also reveal the nature of the error and the path forward for model improvement. The error metrics show good correlation between the 3D-wedge model and the DIC data. The 3D-wedge model does not represent the experimental data perfectly, but provides substantial improvement over current axisymmetric pretension section representations.

## 6.2 Recommendations

The make-up event is only the beginning of the connection model evaluation process. Future efforts should test the above models to determine if an enhanced ability to predict seal performance has been achieved. Efforts to minimize physical testing should then be carried out as highlighted below.

### 6.2.1 The In-Plane Minimum Seal Performance Envelope

The seal(s) of the minimum error make-up model are to be monitored as service loads are applied using the seal metrics of Section 4.8. A minimum seal performance envelope can be developed for the particular connection variant. The envelope is then discretized using a series of segments as shown in Figure 6.1. The discretized “In-Plane Minimum Seal Performance Envelope” is a mathematical representation of the seal performance limits at a given location in the design space.

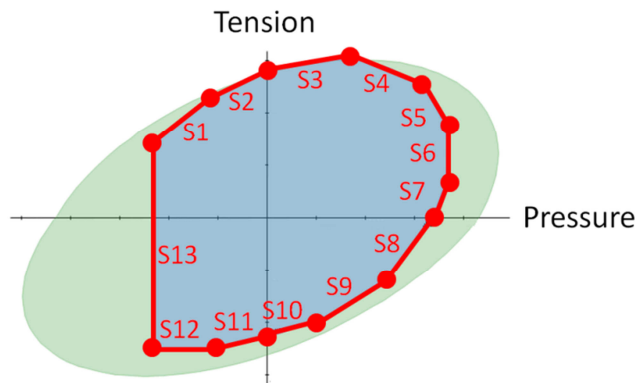


Figure 6.1: The In-Plane Minimum Seal Performance Envelope can be discretized into several segments which allow the envelope to be operated upon.

### 6.2.2 The Out-of-Plane Minimum Seal Performance Envelope

Several In-Plane Minimum Seal Performance Envelopes built from geometric connection variants can be related by applying trajectory functions as shown in Figure 6.2. These trajectory functions operate in the space between well-defined connection variants and can be used to generate an “Out-of-Plane” projection of untested seal performance. Once the trajectory

functions are defined, interpolation methods can be utilized to study seal performance as a function of a single design variable.

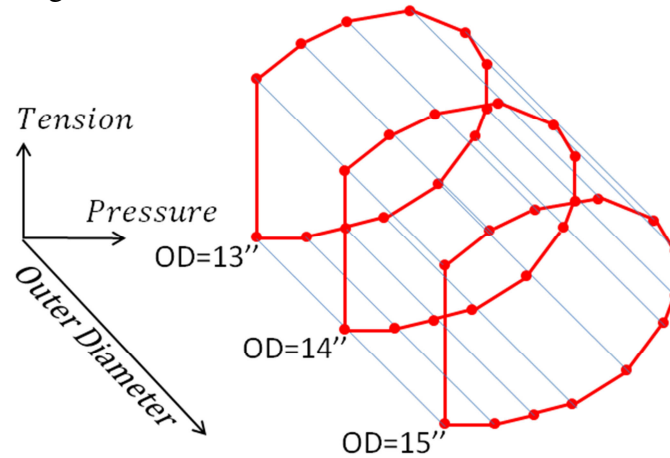


Figure 6.2: Trajectory functions can be used to generate Out-of-Plane Minimum Seal Performance envelopes and to interpolate minimum seal performance limits between known test configurations. Here the trajectories operate as a function of the outer diameter design variable.

### 6.2.3 Response Surface Modeling

Seal performance can also be studied as a function of multiple design variables by applying response surface methods. The response surface is a well-defined statistical tool that typically assumes a polynomial solution to a function of interest over a domain, uses sampling methodology to examine the domain, then defines a least-squares-error best-fit solution to model the function of interest [29]. It is a powerful technique because it allows the analyst to explore a design space while accounting for coupled design variables. The basics of the finite-element-based response surface are provided in Appendix E, and the possible applications to OCTG are discussed below.

#### 6.2.3.1 Response Surface Analysis of Premium Connections

Application of response surface techniques in the analysis of premium connections allows simultaneous consideration of coupled design variables. Rather than sampling a well-known function over an arbitrary domain as Appendix A, the response surface can sample parametric finite element models operating within the feasible design space. Design optimization methods can then operate upon the constructed response surface to identify and investigate areas of interest [30].

##### 6.2.3.1.1 Response Surface Make-up Studies

Response surfaces can be applied to calibrate a finite element make-up model based on experimental and/or analytical make-up data. This experimental data should take advantage of Digital Image Correlation as outlined in Chapter 3. Recommendations for the formulation of the finite element make-up model are made in Chapter 4. The functions of interest are the model error metrics developed in Section 5.1. The domain of the make-up problem is the design space defined by an arbitrary number of connection design variables. These design variables describe a particular geometric variant and/or modeling assumption of a make-up model. The particular combination of design variables that produces a model with minimum error can be identified as

illustrated in Figure 6.3. Service load studies can then be performed on the minimum error make-up model.

Table 6.1: Table of design variables for make-up studies

<b>Design Variables</b>
Connection Type
Connection Diameter
Connection Wall Thickness
Material Model
Thread Interference
Seal Interference
Box Taper
Pin Taper
Axial Interference Parameter(s) or Make-up Torque
Friction Coefficient

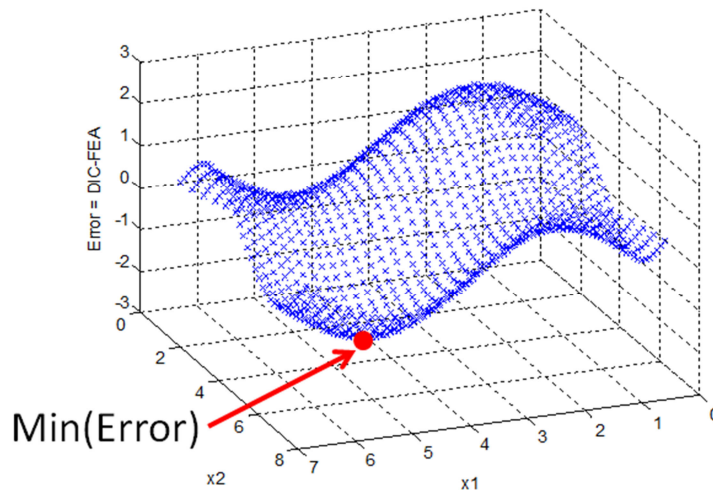


Figure 6.3: The response surface can operate upon a parametric finite element make-up model to identify the modeling configuration that produces the minimum error with respect to the experimental data.

### 6.2.3.1.2 Response Surface Service Load Studies

Application of response surface methodology to premium connection service load studies produces a systematic way to explore and characterize seal performance once a minimum error make-up model has been achieved. The functions of interest are now the seal metrics developed in Section 4.8. The sample points are the load configurations operating on the minimum error make-up model at feasible locations in the load space. The domain of the problem is the load space defined by an arbitrary number of load types which may include those found in Table 6.2. Areas of minimum seal performance can be identified in order to eliminate unnecessary physical testing, and testing efforts can be directed towards areas of marginal performance. These areas of marginal performance can then be investigated analytically as well as experimentally to further refine the application of the seal metrics.

Table 6.2: Table of load variables for service load studies

Service Load Variables
Axial Load
Bending Moment
Internal Pressure
External Pressure
Internal Temperature
External Temperature

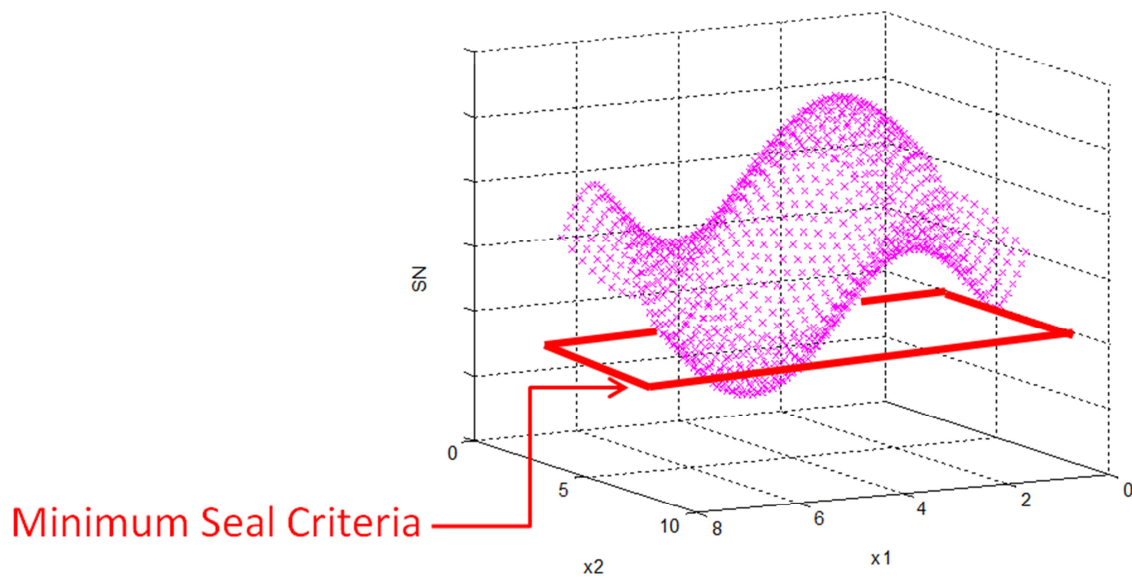


Figure 6.4: The response surface can operate upon a parametric finite element service load model to investigate seal performance across the load space.

### 6.2.3.1.3 Reducing Response Surface Dimensionality

Methods to reduce the dimensionality of the problem should be investigated to the furthest possible extent to reduce the number of model runs required to represent the design and load space. Some of the best ways to accomplish this are to combine similar variables, or use similitude in the system to reduce dimensionality [28]. A common reduction is to combine the nominal wall thickness and outer diameter into a ratio [1,9]. Other reductions can be made by combining box and pin tapers into a taper difference or combining internal and external load variables into differential forms. Only the *most relevant and essential* variables should be used in the construction of the response surface, and the variables believed to be *most dominant* should be investigated first.

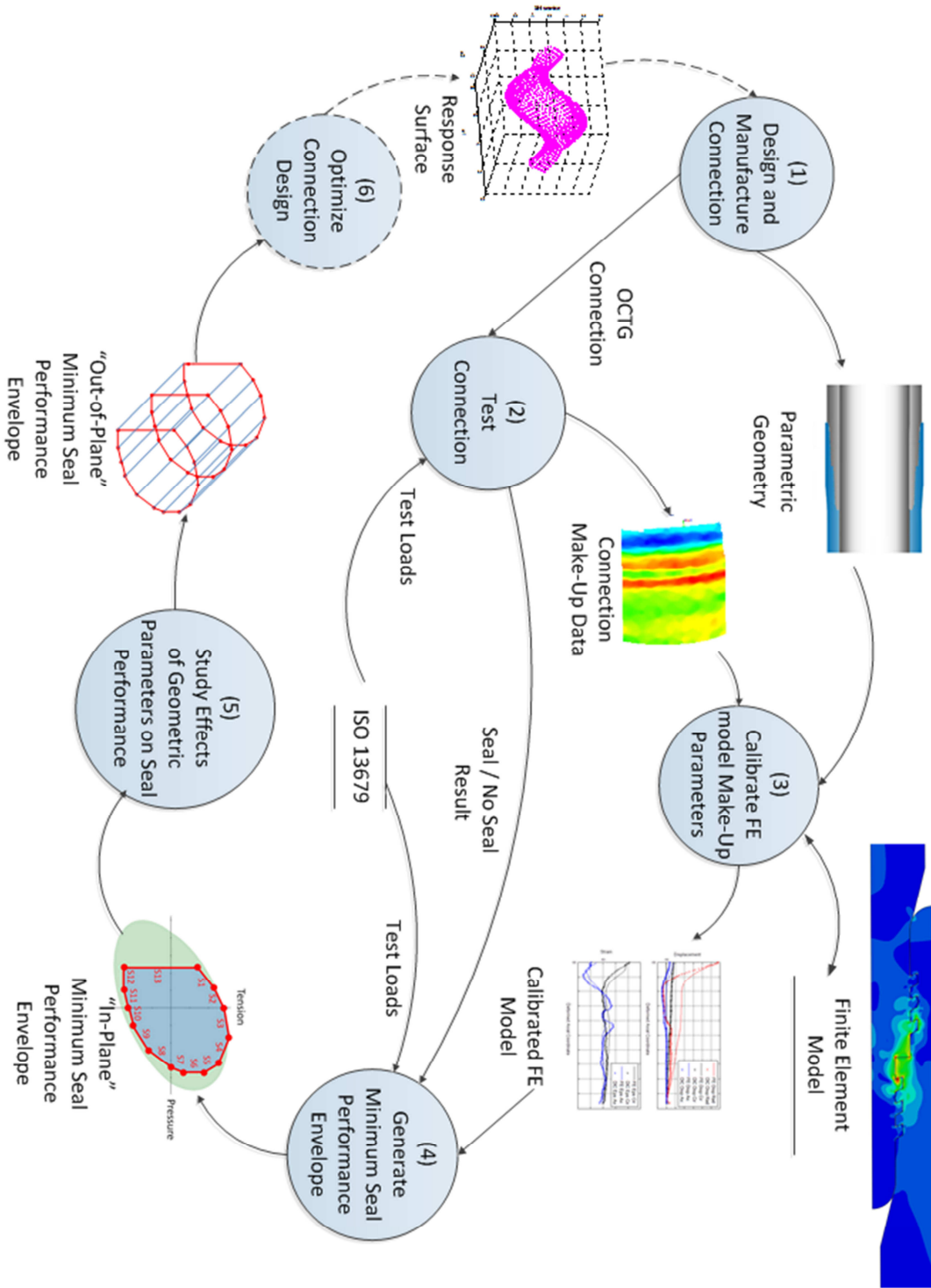
# Bibliography

- [1] Khemakhem A. S. D., Biegler M. W., Baker D. A., Burdette J. A., Dale B. A., Mohr J. W., Ceyhan I., Powers J., Myers J. H., and Asman M., 2009, “Method and System for Evaluating Groups of Threaded Connections. U.S. Patent Application Publication No.: US 2009/0250926 A1.”
- [2] DeMarco T., 1979, *Structured Analysis and System Specification*, Prentice-Hall, Inc, Englewood Cliffs, New Jersey.
- [3] Weiner P. D., 1968, “Analysis of Tapered Threaded Thick Walled Tubing Connections,” Texas A&M University.
- [4] Hilbert Jr. L. B., and Kalil I. A., 1992, “Evaluation of Premium Threaded Connections Using Finite-Element Analysis and Full-Scale Testing,” IADC/SPE Drilling Conference, New Orleans, Louisiana, pp. 563–580.
- [5] Ceyhan I., Khemakhem A. S. D., Coe D., Myers J. H., and Powers J., 2001, *ExxonMobil Connection Evaluation Program*, First Edition, ExxonMobil Upstream Research, Houston, Texas.
- [6] Dvorkin E., and Toscano R. G., 2003, “Finite element models in the steel industry Part II: Analyses of tubular products performance,” *Computers & Structures*, **81**(8-11), pp. 575–594.
- [7] ISO 13679-2002 Petroleum and natural gas industries- Procedures for testing casing and tubing connections, International Organization for Standardization, Geneva, Switzerland.
- [8] Heijnsbroek E. P. L., 1995, “Sealing Mechanism of Dry Metal-to-Metal Seals,” Delft University of Technology.
- [9] Powers J., Baker D. A., and Chelf M. S., 2008, “Application of Connection Productline Evaluation,” IADC/SPE Drilling Conference & Exhibition proceedings ; sustainable strategies for today’s realities ; 4-6 March, 2008 Orlando Florida, USA.
- [10] Sugino M., Nakamura K., Yamaguchi S., Metal S., Daly D., Briquet G., and Verger E., 2010, “Development of an Innovative High-performance Premium Threaded Connection for OCTG,” Offshore Technology Conference, Houston, Texas.
- [11] Sutton M. A., Orteu J.-J., and Shrier H. W., 2009, *Image Correlation for Shape, Motion and Deformation Measurements*, Springer Science+Buisness Media, LLC, New York, New York.

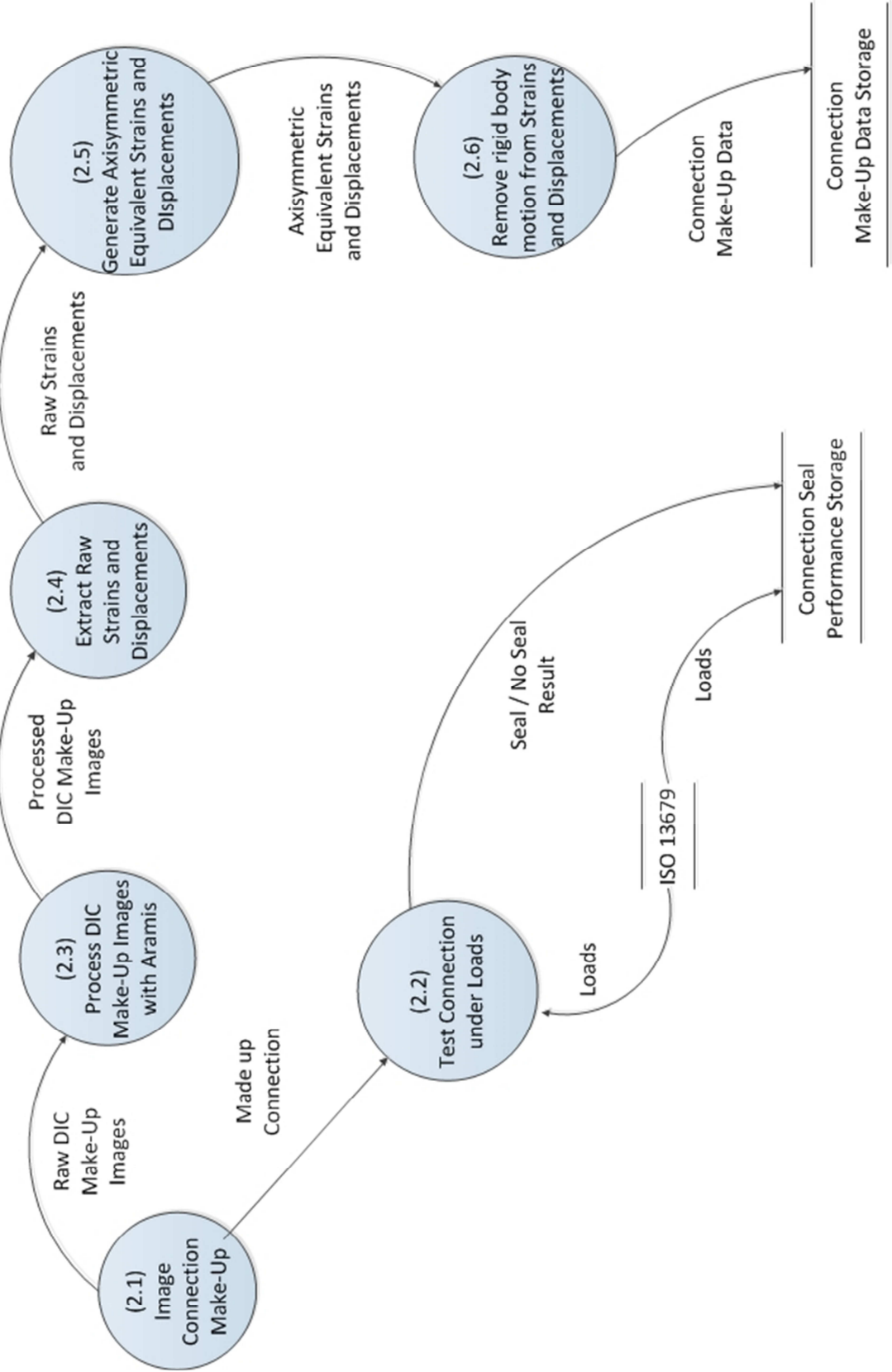
- [12] Schmidt T., 2012, “Uncertainty Quantification in DIC : A Practical Approach,” SEM XII International Congress & Exposition on Experimental and Applied Mechanics, Costa Mesa, California.
- [13] Schmidt T., 2012, 3D ARAMIS Sensitivity, Accuracy, and Data Validity Considerations, Trillion Quality Systems LLC, Plymouth Meeting, PA.
- [14] Reu P., 2012, “Introduction to Digital Image Correlation: Best Practices and Applications,” *Experimental Techniques*, **36**(1), pp. 3–4.
- [15] Reu P., 2012, “Hidden Components of DIC: Calibration and Shape Function - Part 1,” *Experimental Techniques*, **36**(2), pp. 3–5.
- [16] Reu P., 2012, “Hidden Components of 3D-DIC: Interpolation and Matching - Part 2,” *Experimental Techniques*, **36**(3), pp. 3–4.
- [17] Reu P., 2012, “Hidden Components of 3D-DIC: Triangulation and Post-processing - Part 3,” *Experimental Techniques*, **36**(4), pp. 3–5.
- [18] Hess Corporation, courtesy of David Coe.
- [19] “Gesellschaft für Optische Messtechnik (GOM) Optical Measuring Techniques, [www.gom.com](http://www.gom.com).”
- [20] 2000, The Fundamentals of Signal Analysis, Application Note 243, Agilent Technologies, Santa Clara, California.
- [21] Dassault Systèmes Simulia Corp., 2010, “Abaqus/CAE 6.10-EF1 Build ID: 2010\_11\_10-12.50.59 106506.”
- [22] 2011, Material Test Data Project No: IR-397.01, MTEC Mechanical Testing Services, Houston, Texas.
- [23] Dowling N. E., 2007, *Mechanical Behavior of Materials*, Pearson Education Inc., Upper Saddle River, New Jersey.
- [24] MathWorks, 2011, “MATLAB Version 7.12.0.635 (R2011a).”
- [25] Advanced Research Computing at Virginia Tech, <http://www.arc.vt.edu>.
- [26] Cook R. D., Malkus D. S., Plesha M. E., and Witt R. J., 2002, *Concepts and Applications of Finite Element Analysis*, John Wiley & Sons. Inc, New York, New York.
- [27] Boresi A. P., and Schmidt R. J., 2003, *Advanced Mechanics of Materials*, John Wiley & Sons. Inc, New York, New York.

- [28] Langhaar H. L., 1962, Energy Methods in Applied Mechanics, John Wiley & Sons. Inc, New York, New York.
- [29] Box G. E. ., and Draper N. ., 1987, Empirical Model-Building and Response Surfaces, John Wiley & Sons. Inc, New York, NY.
- [30] Arora J., 2004, Introduction to Optimum Design, Elsevier Academic Press, San Diego, California.
- [31] Reddy J. N., 1993, An Introduction to the Finite Element Method, MCGraw-Hill Inc., New York, New York.

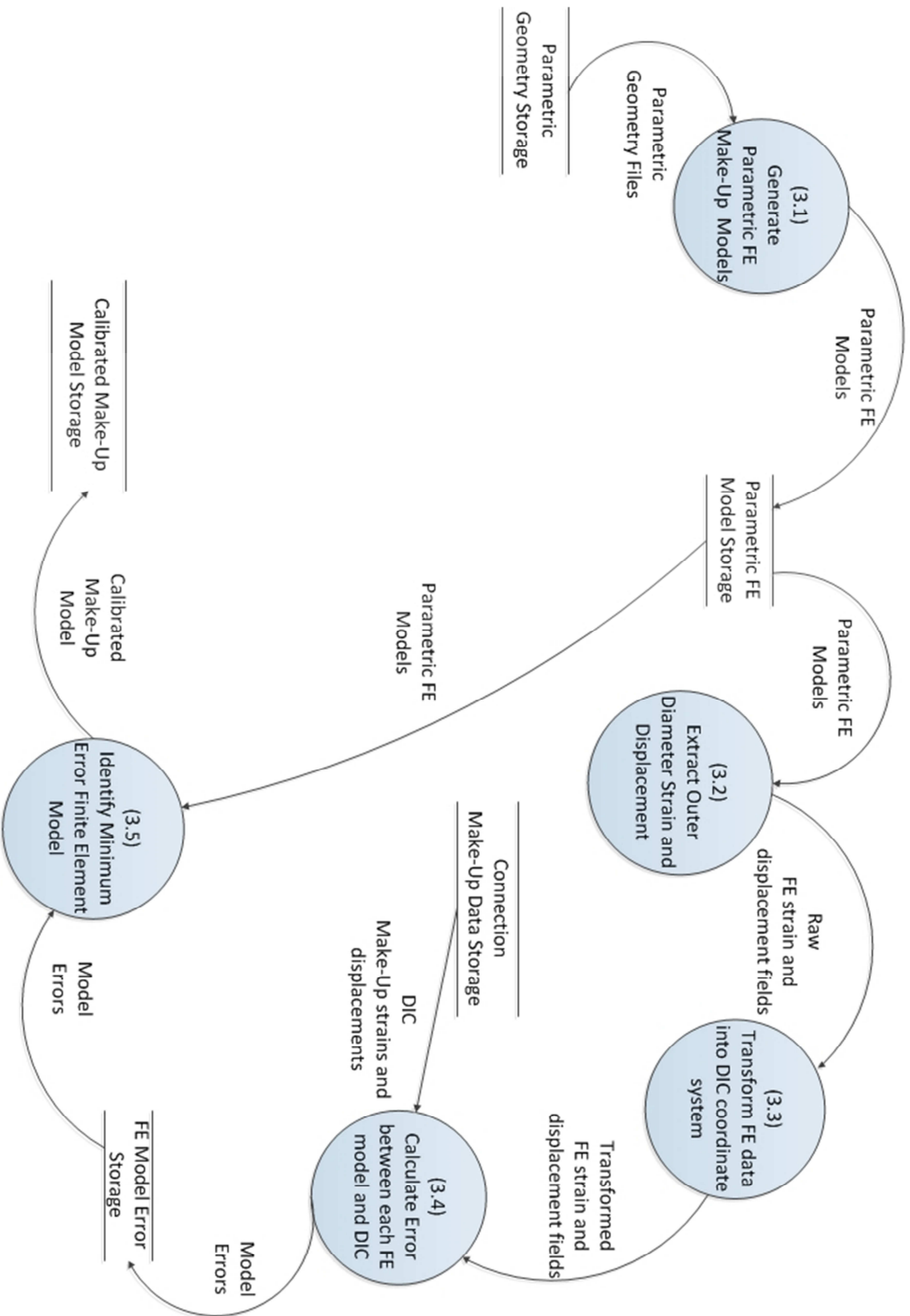
# Appendix A Data Flow Diagram for Minimum Seal Performance Envelope Generation



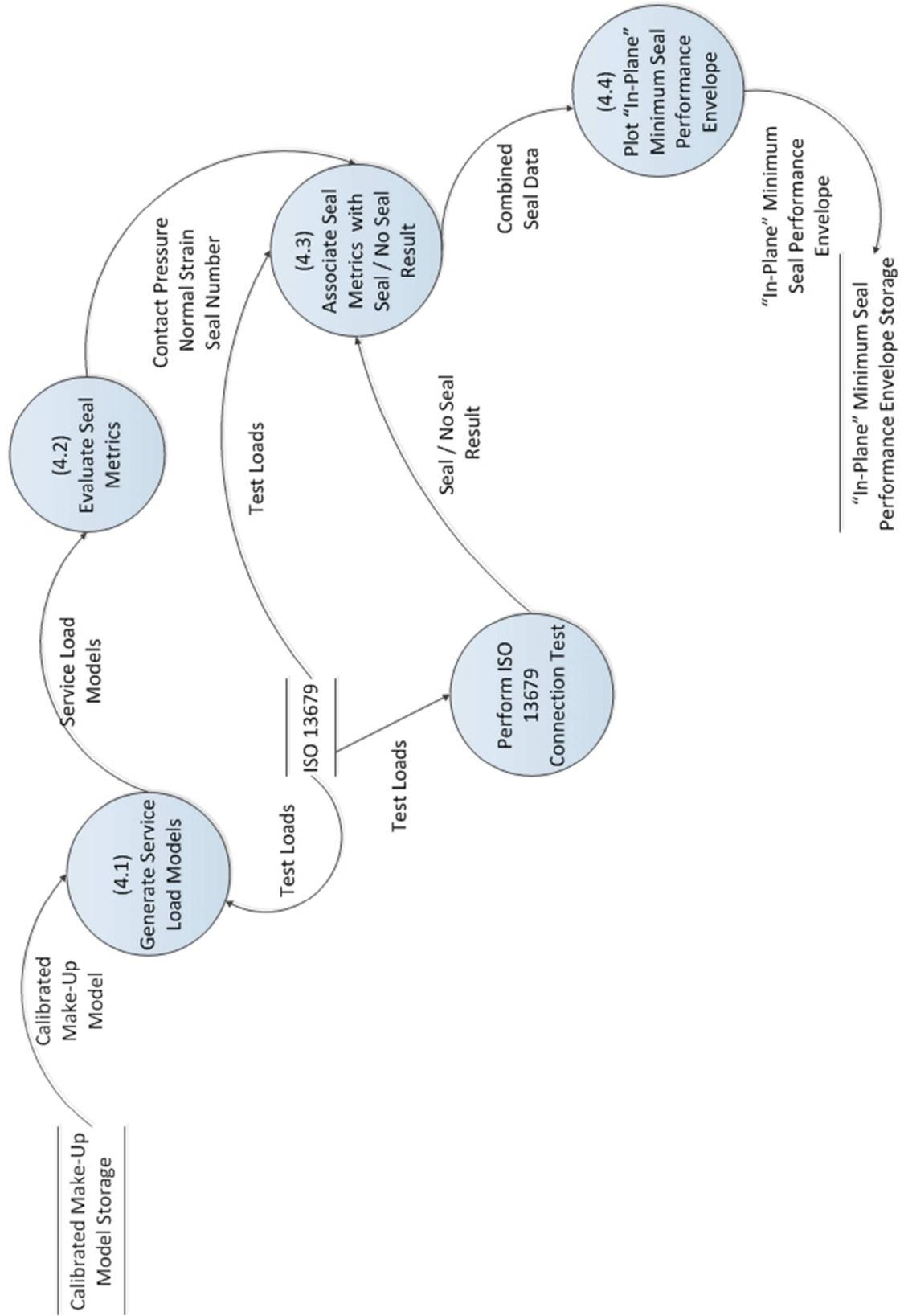
## (2) Test Connection



### (3) Calibrate Make-Up Parameters



# (4) Generate Minimum Seal Performance Envelope





# Appendix B Photographs of Experimental Setup

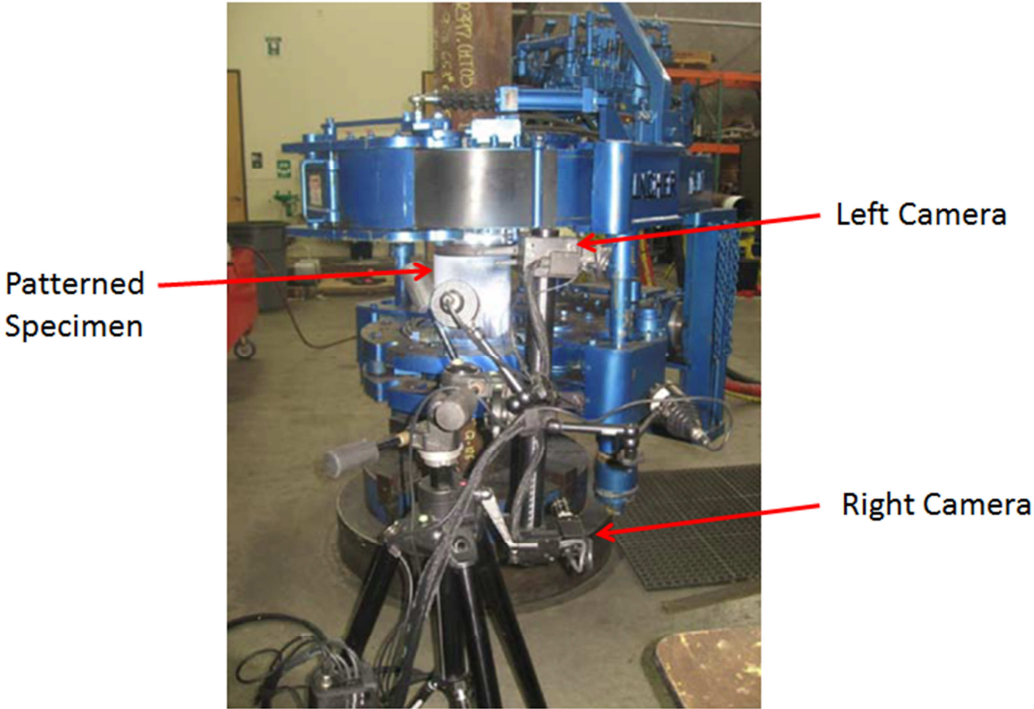


Figure B.1: A good DIC experimental setup. Cameras pushed far apart to maximize the dynamic range of the out-of-plane ray tracing measurement. Cameras are also oriented parallel to the pipe axis to give better resolution for in-plane measurements. Used with permission of Hess Corporation [18].

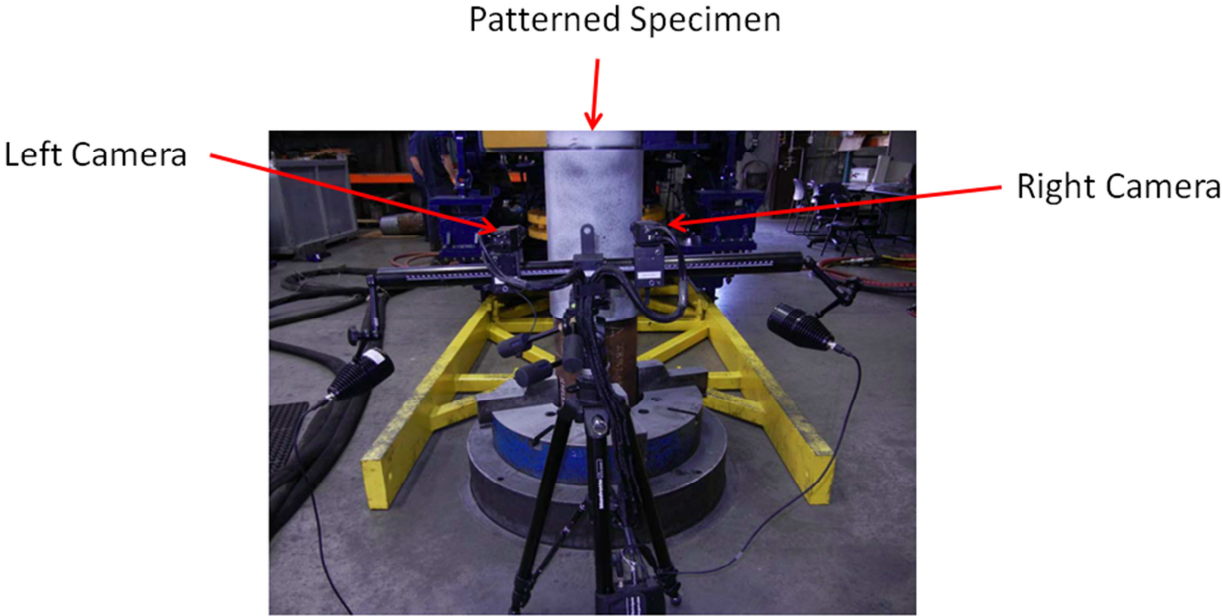


Figure B.2: A poor DIC experimental setup. Cameras are not separated by a sufficient angle. Cameras also oriented perpendicular to the pipe axis. Used with permission of Hess Corporation [18].



# Appendix D MATLAB Code for Deformation Plasticity Material Model Optimization

```

% Ramberg Osgood material constants optimization fit for Abaqus formulation
clc
clear all
StressDATA=[]; % Insert Stress Data Here
StrainDATA=[]; % Insert Corresponding Strain Data Here
%% Abaqus form for the ramberg osgood stress-strain relation
%Initial Parameters (constant)
E0=; %Young's Modulus
so0=; %Yield offset
eo=; %strain at Yield offset
% Initial variable values
n0=1;
alpha0=((eo*E0)/so0)-1;
x0=[alpha0,n0,so0,E0];
%FINDS OPTIMIZED RAMBERG-OSGOOD CONSTANTS IN ABAQUS FORM
[x]=lsqnonlin(@strainError,x0)
alpha=x(1)
n=x(2)
so=x(3)
E=x(4)
%Plot initial fit and final fit over experimental data
stressfit=linspace(0,1100,1000);
for i=1:length(stressfit)
    strainfitFinal(i)=AbqRO_StrainCalc(alpha,n,so,stressfit(i),E);
end
plot(StrainDATA,StressDATA,'ro',strainfitFinal,stressfit,'b')
%title('Abaqus form of Ramberg-Osgood stress/strain curve')
xlabel('strain ( )')
ylabel('stress ( )')
legend ('Material Test Data Points','Fitted Ramberg Osgood Curve')
grid on
%check that the proper relationship is satisfied at yield onset
check=0.0065-so/E*(1+alpha)
function [strainErr]= strainError(x)
    alpha=x(1);
    n=x(2);
    so=x(3);
    E=x(4);
    StressDATA=[]; % Insert Stress data here
    StrainDATA=[]; % Insert Strain data here
    % Abaqus form for the ramberg osgood stress-strain relation
    %Parameters (constant)
    E=; %Youngs Mod
    eo=; %Strain at yield offset
    for i=1:length(StressDATA)
        strainErr(i)=AbqRO_StrainCalc(alpha,n,so,StressDATA(i),E)...
            -StrainDATA(i);
    end
end
function [AbqRO_Strain]= AbqRO_StrainCalc(alpha,n,so,s,E)
    %Abaqus form of the Ramberg Osgood stress strain relationship
    AbqRO_Strain=s/E+(s*alpha)/E*(abs(s)/so)^(n-1);
end

```

# Appendix E Finite-Element Based Response Surface Formulation

The response surface is formulated below with a finite element-based-twist. Rather than fitting a series of polynomials over the domain, the domain is discretized into a set of response surface elements which use Gauss-Legendre sampling schemes to sample the space. Lagrangian shape functions are used to solve the over-determined system and find a least-squares-error best-fit solution to the function of interest over the domain of each response surface element. The response surface mesh can then be refined to the point of convergence where it represents the function of interest within an acceptable margin.

Once nodal function values  $y_{ij}$  are known, the response surface may be queried for a function value anywhere in the element domain using

$$y_i(x) = \sum_{j=1}^{\max(j)} y_{ij} * N_{ij}(x) \quad (E.1)$$

Where  $j$  is the node number within response surface element  $i$ ,  $y_{ij}$  are the nodal function values corresponding to  $y_{ij} = y_i(x)$ ,  $N_{ij}$  are the shape functions for element  $i$ , and  $x$  is the desired sample location the within the domain. The bulk of the effort in response surface modeling is finding the nodal function values  $y_{ij}$ . This is accomplished by finding the solution to the function of interest  $F(x)$  at sample locations  $\bar{x}_{ij}$  as shown in Equation (E.2). The sample locations  $\bar{x}_{ij}$  are arbitrary but will be demonstrated with Gauss-Legendre sampling schemes.

$$\bar{y}_{ij} = F(\bar{x}_{ij}). \quad (E.2)$$

The function of interest,  $F(x)$ , is rarely a function of a single variable but rather a vector of design parameters denoted as  $\{x\} = \{x_1, x_2, \dots, x_n\}$ . The parameters used to create the vector  $\{x\}$  are at the discretion of the investigator. Great care should be used to limit the size of  $\{x\}$  because the number of samples required to construct the full response surface grows according to Equation (E.3).

$$s = l^n \quad (E.3)$$

Where  $s$  is the number of samples required to fully construct the response surface,  $l$  is the number of levels at which each variable of  $\{x\}$  will be sampled (proportional to the response surface mesh density), and  $n$  is the number of independent variables that the response surface is operating within.

To solve for the best fit response surface, a mesh must first be generated over the domain. Once the mesh is in place, sample points are calculated within find the nodal function values  $y_{ij}$ ,

## E.1 Response Surface Example in a Single Dimension

To model the single dimension function  $F(x) = x^2$  over the domain  $\{0 \leq x \leq 1\}$ , we shall first assume a linear form for the response surface. Two elements will be used as shown in Figure E.5. The Lagrangian shape functions for the linear 1D case are given in Equation (E.4) [26]

$$N_1 = \frac{x_2 - x}{x_2 - x_1}$$

$$N_2 = \frac{x - x_1}{x_2 - x_1}$$
(E.4)

Where  $x_1$  is the coordinate of node 1, and  $x_2$  is the coordinate of node 2. Two point Gauss-Legendre sampling is used which results in samples taken for the 1D linear element at the normalized local coordinates  $\xi = \pm 0.5773502692$  [31]. These sample points can be transformed into the global system by Equation (E.5) [31].

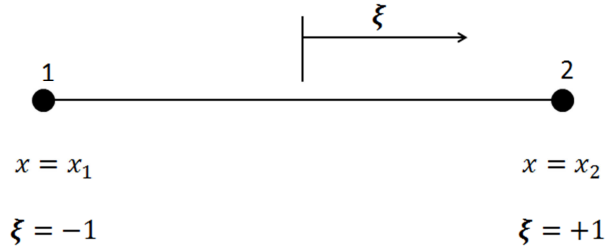


Figure E.3: The 1D linear response surface element with normalized local coordinate  $\xi$ .

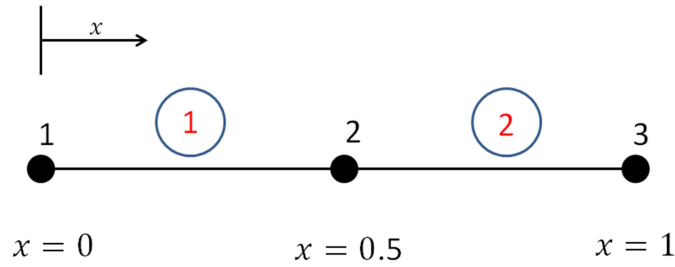


Figure E.4: The 1D response surface mesh in the global coordinate system consisting of two linear 1D elements.

$$\bar{x}_{ij} = x_1 + \frac{1}{2}(x_2 - x_1) * (1 + \xi)$$
(E.5)

This results in sample points being generated at the locations shown in Table E.1.

Table E.1: Sampling locations for the 1D example problem.

Element	Element Sample Number	Normalized Coordinate	Global Coordinate
1	1	$\xi = -1/\sqrt{3}$	$\bar{x}_1 = 0.1057$
1	2	$\xi = +1/\sqrt{3}$	$\bar{x}_2 = 0.3943$
2	1	$\xi = -1/\sqrt{3}$	$\bar{x}_3 = 0.6057$
2	2	$\xi = +1/\sqrt{3}$	$\bar{x}_4 = 0.8943$

The element shape functions for the mesh are constructed by applying Equation (E.1) as shown in Table E.2.

Table E.2: Shape function contributions for the 1D example problem.

Element	Element Shape Function Contribution
1	$\bar{y}_1 = f(\bar{x}_1) = N_1(\bar{x}_1)y_1 + N_2(\bar{x}_1)y_2$
1	$\bar{y}_2 = f(\bar{x}_2) = N_1(\bar{x}_2)y_1 + N_2(\bar{x}_2)y_2$
2	$\bar{y}_3 = f(\bar{x}_3) = N_1(\bar{x}_3)y_2 + N_2(\bar{x}_3)y_3$
2	$\bar{y}_4 = f(\bar{x}_4) = N_1(\bar{x}_4)y_2 + N_2(\bar{x}_4)y_3$

These equations can be assembled into a global shape matrix as shown in Equation (E.5)

$$\begin{Bmatrix} \bar{y}_1 \\ \bar{y}_2 \\ \bar{y}_3 \\ \bar{y}_4 \end{Bmatrix} = \begin{bmatrix} N_1(\bar{x}_1) & N_2(\bar{x}_1) & 0 \\ N_1(\bar{x}_2) & N_2(\bar{x}_2) & 0 \\ 0 & N_1(\bar{x}_3) & N_2(\bar{x}_3) \\ 0 & N_1(\bar{x}_4) & N_2(\bar{x}_4) \end{bmatrix} \begin{Bmatrix} y_1 \\ y_2 \\ y_3 \end{Bmatrix} \quad (\text{E.6})$$

$$\{\bar{y}\} = [N]\{y\}$$

Where  $\{\bar{y}\} = F(\{\bar{x}\})$  is the vector of function values at the sampling locations,  $[N]$  is the matrix of shape functions, and  $\{y\}$  is the vector of nodal function values. Equation (E.6) has four equations and three unknowns and thus is an over determined system. The squared error of the response surface in representing the function can be written in Equation (E.7). Application of Equation (E.7) at the nodes can be found in Equation (E.8).

$$E_i^2 = (y_i - \bar{y}_i)^2 \quad (\text{E.7})$$

$$\begin{aligned} E_1^2 &= (N_1(\bar{x}_1)y_1 + N_2(\bar{x}_1)y_2 - \bar{y}_1)^2 \\ E_2^2 &= (N_1(\bar{x}_2)y_1 + N_2(\bar{x}_2)y_2 - \bar{y}_2)^2 \\ E_3^2 &= (N_1(\bar{x}_3)y_2 + N_2(\bar{x}_3)y_3 - \bar{y}_3)^2 \\ E_4^2 &= (N_1(\bar{x}_4)y_2 + N_2(\bar{x}_4)y_3 - \bar{y}_4)^2 \end{aligned} \quad (\text{E.8})$$

The goal is to minimize the sum squared error as shown in Equation (E.9)

$$\text{Min} \left( \text{SSE} = \sum_{i=1}^4 E_i^2 \right) \quad (\text{E.9})$$

This minimum can be found by taking the partial derivative of the sum squared error function with respect to each nodal value  $y_i$  and setting it to zero. This is demonstrated for node 1 in Equation (E.10).

$$\frac{\delta SSE}{\delta y_1} = 0 = 2 * [N_1(\bar{x}_1)y_1 + N_2(\bar{x}_1)y_2 - \bar{y}_1] * N_1(\bar{x}_1)$$

$$0 = N_1(\bar{x}_1)N_1(\bar{x}_1)y_1 + N_1(\bar{x}_1)N_2(\bar{x}_1)y_2 - N_1(\bar{x}_1)\bar{y}_1 \quad (E.10)$$

$$y_1 = \frac{N_1(\bar{x}_1)N_2(\bar{x}_1)y_2 - N_1(\bar{x}_1)\bar{y}_1}{N_1(\bar{x}_1)N_1(\bar{x}_1)}$$

This process can be continued for each individual node, or the vector of nodal values  $\{y\}$  can be solved in matrix form by Equation (E.11).

$$\{y\} = ([N]^T [N])^{-1} [N]^T \{\bar{y}\} \quad (E.11)$$

This least-squares error response surface solution is plotted in Figure E.5.

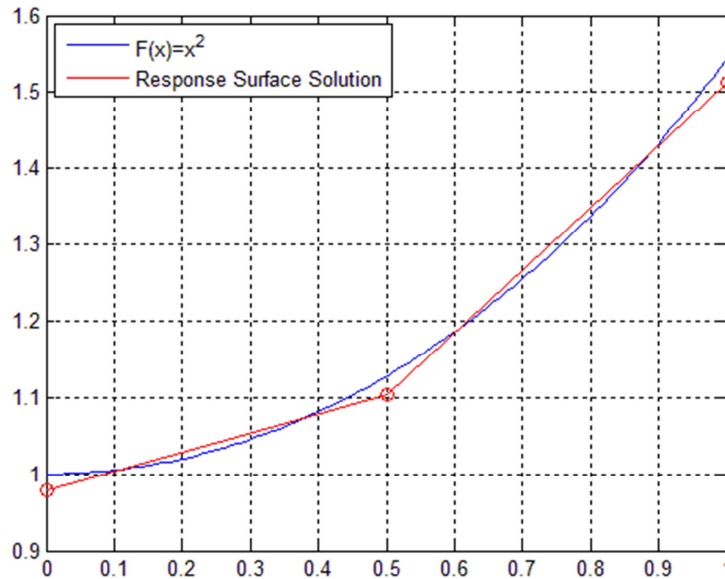


Figure E.5: The linear response surface solution to  $F(x) = x^2$  using two elements.

The response surface solution is exact only at the sampling locations because a linear form of the solution was assumed for a quadratic function. A single quadratic element as shown in Figure E.6 could be used to represent the function exactly. The shape functions for this element are given in Equation (E.12) [26].

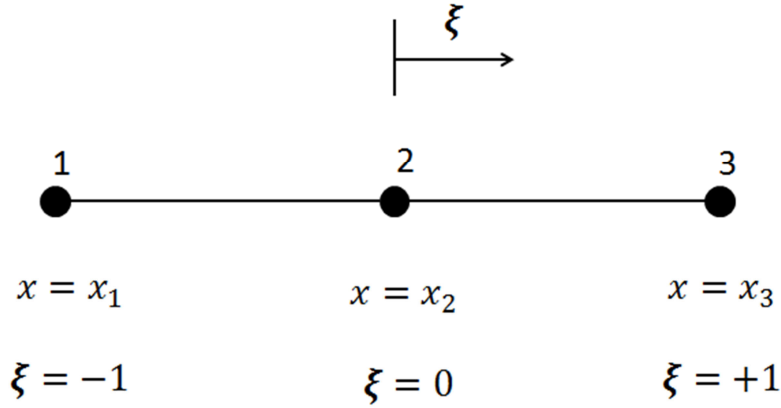


Figure E.6: The 1D quadratic response surface element.

$$\begin{aligned}
 N_1 &= \frac{(x_2 - x)(x_3 - x)}{(x_2 - x_1)(x_3 - x_1)} \\
 N_2 &= \frac{(x_1 - x)(x_3 - x)}{(x_1 - x_2)(x_3 - x_2)} \\
 N_3 &= \frac{(x_1 - x)(x_2 - x)}{(x_1 - x_3)(x_2 - x_3)}
 \end{aligned}
 \tag{E.12}$$

The same process applies in the case of the single quadratic element, only the shape functions and the sampling scheme have changed. A three point Gauss-Legendre sampling scheme is used which has samples taken at normalized coordinates of  $\xi = \pm 0.77745966692$  and  $\xi = 0$  [31]. Because only one quadratic element is needed to model the system perfectly, only three samples must be taken over the whole domain. The samples are evaluated, and the nodal function values are computed according to Equation (E.11). The quadratic response surface is plotted in Figure E.7.

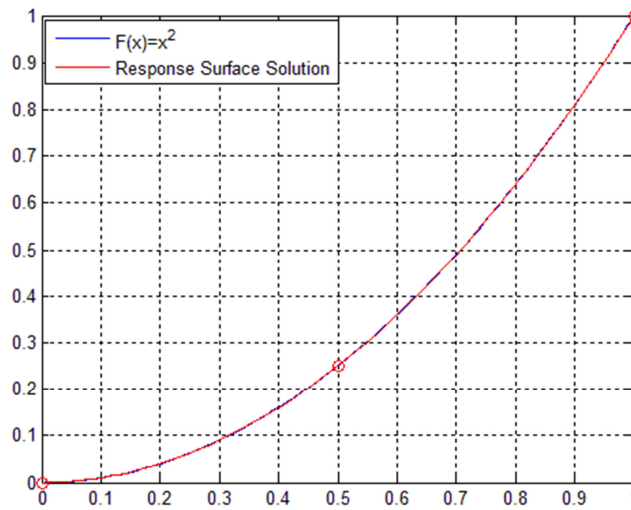


Figure E.7: The single quadratic element response surface solution to  $F(x) = x^2$ .

## E.2 Extending the Response Surface to Problems of Higher Dimension

The same response surface methodology can be extended to problems of two dimensions by taking the tensor product of the 1D shape functions [26]. An example mesh consisting of four bilinear response surface elements is shown in Figure E.8. The shape matrix  $[N]$  is generated for the mesh, and the function of interest is evaluated at the sample points. The nodal solution is then found by Equation (E.11). With mesh refinement to the point of convergence, any function can be well represented within an acceptable margin.

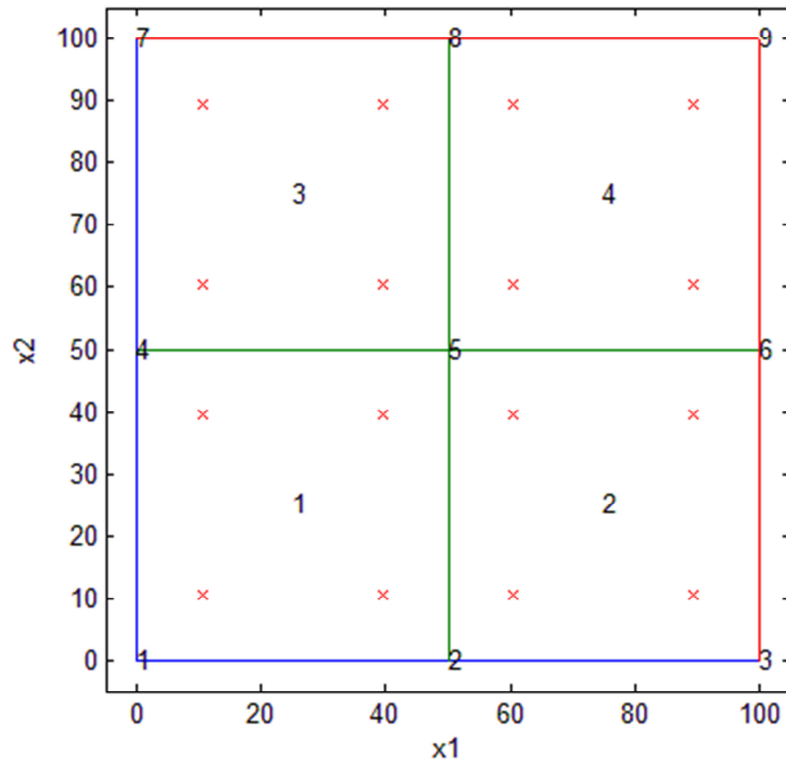


Figure E.8: An example bilinear mesh in two dimensions. Four linear elements are used to represent the domain with two point Gauss sampling shown by red 'x'.

Similarly the response surface can be further extended to any number of dimensions by again taking the tensor product of the 1D shape functions. Error estimates of the response surface can be made by comparing response surface solutions to results extracted from models constructed at the response surface nodal coordinates.

# Appendix F Copyright Permission Letters

Agilent Technologies, Inc. 408-553-2772 telephone  
Intellectual Property Group 408-553-2365 facsimile  
5301 Stevens Creek Blvd, MS 1A-PB j.m\_simon@agilent.com  
Santa Clara, CA 95051 www.agilent.com

James L. Simon  
Corporate Counsel



February 12, 2013

Via email to: [cogaard@vt.edu](mailto:cogaard@vt.edu)

Erik Ostergaard  
Masters Candidate  
VT Mechanical Engineering  
(+1) 412-996-1671  
4541 Rosebud Drive  
Columbus, Indiana 47203

Re: Permission to Copy and Republish Agilent Materials

Dear Erik:

This is in response to your recent email request for consent to copy and republish certain materials in which Agilent owns the copyright. I have attached for clarity a copy of the email that sets out your request. I am pleased to advise that, per your request, Agilent Technologies, Inc. gives its consent for you to use the diagram, namely, Figure 3.9 The relationship between the time and frequency domains. a) Three dimensional coordinates showing time, frequency, and amplitude b) Time domain view c) Frequency domain view, in your Master's thesis.

We ask that there be included in this material, an appropriate acknowledgment and an appropriate copyright notice in a form similar to the following (with the year date in the notice below being the year date in the notice in the respective Agilent source document):

© Agilent Technologies, Inc. <date>  
Reproduced with Permission, Courtesy of Agilent Technologies, Inc.

By reproducing these materials, you acknowledge and agree: (1) that the Agilent work(s) and the information contained therein are accepted "AS IS"; (2) that Agilent does not make any representations or warranties of any kind with respect to the materials and disclaims any responsibility for them as reproduced by you; (3) that Agilent Technologies has the right to review any use or display of these materials and to terminate this consent and require their immediate removal if altered, modified, or portrayed in any way that, in Agilent's opinion, is in poor taste or diminishes the reputation of Agilent or its products; (4) that Agilent will not be liable for any damages, whether special, incidental, consequential, direct, indirect or

punitive, resulting from or in connection with the use, copying or disclosure of the above referenced documentation, and (5) to indemnify Agilent Technologies for all claims, actions, damages, and expenses (including attorneys' fees) incurred by Agilent as a result the Agilent work(s) being reproduced, modified, or distributed pursuant to this consent.

Thank you for your interest in Agilent Technologies, Inc. and its products and services.

Sincerely,

A handwritten signature in cursive script that reads "James L. Simon".

James L. Simon  
Corporate Counsel

Enclosures:  
JLS/tj

Erik Ostergaard  
4541 Rosebud Drive,  
Columbus, Indiana 47203

February 12, 2013

David Coe  
1501 McKinney Street,  
Houston, TX 77010

Dear Mr. Coe:

This letter will confirm our recent email exchange. I am completing a masters thesis at Virginia Tech entitled "A Refined Methodology for Calibrating Premium Threaded Connection Make-ups." I would like your permission to reprint in my thesis excerpts from the following information from our correspondence.

The excerpts to be reproduced are found in the thesis as:

Figure 3.1 , Figure 3.2 , Figure 4.13 , Appendix B , Appendix C

A pdf of the draft thesis is available at [https://dl.dropbox.com/u/145836/Ostergaard\\_EB\\_T\\_2012.pdf](https://dl.dropbox.com/u/145836/Ostergaard_EB_T_2012.pdf).

The requested permission extends to any future revisions and editions of my dissertation, including non-exclusive world rights in all languages, and to the prospective publication of my thesis by Virginia Tech. These rights will in no way restrict republication of the material in any other form by you or by others authorized by you. Your signing of this letter will also confirm that you own [or your company owns] the copyright to the above-described material. If these arrangements meet with your approval, please sign this letter where indicated below and scan and email, or return to me by postal mail. Thank you very much.

Sincerely,

Erik Ostergaard

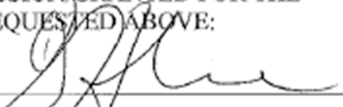


PERMISSION GRANTED FOR THE  
USE REQUESTED ABOVE:

By: \_\_\_\_\_

Title: \_\_\_\_\_

Date: \_\_\_\_\_



Drilling Engineer Advisor - HESS

2/21/2013

Erik Ostergaard  
4541 Rosebud Drive,  
Columbus, Indiana 47203

February 12, 2013

Tim Schmidt  
Trilion Quality Systems  
500 Davis Drive, Suite 200  
Plymouth Meeting, PA 19462

Dear Mr. Schmidt:

This letter will confirm our recent email exchange. I am completing a Master's thesis at Virginia Tech entitled "A Refined Methodology for Calibrating Premium Threaded Connection Make-ups." I would like your permission to reprint in my thesis excerpts from the following information from our correspondence.

The excerpts to be reproduced are found in the thesis as:

Figure 3.3  
Figure 3.4

A pdf of the draft thesis is available at [https://dl.dropbox.com/u/145836/Ostergaard\\_EB\\_T\\_2012.pdf](https://dl.dropbox.com/u/145836/Ostergaard_EB_T_2012.pdf).

The requested permission extends to any future revisions and editions of my dissertation, including non-exclusive world rights in all languages, and to the prospective publication of my thesis by Virginia Tech. These rights will in no way restrict republication of the material in any other form by you or by others authorized by you. Your signing of this letter will also confirm that you own [or your company owns] the copyright to the above-described material.

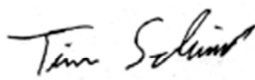
If these arrangements meet with your approval, please sign this letter where indicated below and scan and email, or return to me by postal mail. Thank you very much.

Sincerely,

Erik Ostergaard



PERMISSION GRANTED FOR THE  
USE REQUESTED ABOVE:

By:   
\_\_\_\_\_

Title: Vice President

Date February 19, 2013